ANALYSIS AND DESIGN OF CONCAVE GRATING-BASED DEVICES FOR MULTI-WAVELENGTH OPTICAL NETWORKS

Evgeny G. Churin

A thesis submitted to the University of London for the degree of Doctor of Philosophy (PhD)

Department of Electronic and Electrical Engineering
University College London

November 2003

ProQuest LLC
789 East Eisenhower Parkway
P.O. Box 1346
Ann Arbor, MI 48106-1346

In memory of my father…..

Abstract

This thesis is focused on the analysis and design of concave holographic gratings for applications in wavelength division multiplexed (WDM) optical network devices, such as multi/demultiplexers, routers and channel equalizers. The main advantage of this approach is that a single optical element can perform both functions of dispersion and imaging. However, the design of such gratings for operation in optical fibre communication networks requires the understanding and control of dominant optical aberrations, stray light, and polarization sensitivity. The solution of these problems forms the basis of the work in this thesis.

Chapter 1 presents the motivation for the work, describes the major objectives and lists the main original contributions.

Chapter 2 reviews related works in the field of WDM optical networks. Different published methods and techniques used for channel separation are described.

Chapter 3 describes the analysis of crosstalk in free-space WDM demultiplexers and wavelength routers due to aberrations, diffraction at the aperture, and diffuse scattering from non-uniformities. It is demonstrated experimentally that holographic grating can give background crosstalk as low as -60 dB. Holographic grating-based wavelength routers are shown to be absolutely scalable from the coherent crosstalk point of view, allowing a large number of subscribers/nodes to be interconnected.

Chapter 4 presents aberration analysis of concave grating. New general analytic formulae that define the parameters of concave grating mounts providing stationary and superstationary astigmatism are derived. These mounts offer diffraction-limited imaging within operating spectral range of WDM demultiplexers. A novel retro-reflective scheme of demultiplexer with concave grating and convex mirror resulting in double dispersion and large image field is proposed and analyzed.

Chapter 5 describes in detail all stages of design and adjustment of an athermal 49-channel demultiplexer. The method for accurate calculation of transmission spectra is developed. Tolerances and environmental stability are analyzed and the experimentally measured performance characteristics of fully packaged device are presented.

Chapter 6 presents the design and analysis of 91x91 wavelength router with 0.33 nm channel spacing based on stationary anastigmatic Littrow mount of concave grating. The problem of additional complexity with respect to a demultiplexer relating to the wide field of view in dispersion direction is successfully solved.

Chapter 7 describes the design, analysis and experimental verifications of WDM channel equalizer based on concave grating.

In chapter 8, novel method of flattening and broadening demultiplexer passband is proposed.

The final chapter, presents a summary of the research, and provides suggestions for future work.

Acknowledgements

This dissertation is the result of many years' work, and I owe many people gratitude for their help over that time. First and most importantly, I would like to thank my supervisor Prof. Polina Bayvel for her continuous support, guidance, and encouragement through the course of this work. Most of the problems analysed in this thesis originated from discussions with her. Next I would like to thank Dr. Fedor Timofeev and Vitaly Mikhailov for experimental verification of some ideas and Dr. Alan Hill for his support and technical discussions in the early stages of this work and BT Laboratories for funding a part of it. Support from the Royal Society for my academic visits to UCL under the RS Visiting Fellowship scheme also proved invaluable and served to start this work

Part of results in Chapters 5 and 7 was obtained during my work in E-Tek Dynamics, San Jose (1999-2000). I would like to thank Drs. Phil Anthony, Jinxi Shen, and Val Morozov for the help in working on the concave grating demultiplexer project. I am grateful to E-Tek Dynamics for partially funding the tuition fees, which enabled me to finish this research.

A very warm "thank you" to all those people from room 808 who made the life in UCL a pleasure: Robert Killey, Martin Sabry, Hans Joerg Thiele, Veronika Tsatourian, Derek Rothnie, Paolo Gambini, Stefano Baroni, and the list could continue for lines and lines.

Finally, I would like to thank my wife Tatyana for her patience and support during these years.

Contents

Chapter 1

An Overview

1.1 Introduction

Initially, the increase in network capacity has been accomplished mainly by Time Division Multiplexing (TDM) techniques. However, the demand for information bandwidth has grown rapidly and, finally, exceeded the current capability of TDM equipment. On the contrary, Wavelength Division Multiplexing (WDM) provides a simple way to upgrade the network capacity without adding more fibres. In addition, state-of-the-art gain-flattened optical erbium-doped fibre amplifiers (EDFAs) enable long-haul, high-capacity, WDM transport of multiple wavelength channels in the wavelength range between 1520 and 1570 nm, conventionally denoted as the C-band (C – for conventional) and with research aimed at increasing the usable spectral range over other bands down to 1480 nm (S-band, S denotes - short) and above 1600 nm (L-band, with L for long). In only a few years of deployment, WDM performance has been improved dramatically. Channel count has grown from 4 to above 100 and channel spacing has shrunk from 1000 GHz to 50-100 GHz, commercially, and down to 12.5 GHz in the research laboratories. Although "all-optical" WDM technologies are replacing most single channel TDM transmission lines, the key nodes of the networks, such as switches and cross-connects, still depend on relatively slow electronics and the unnecessary optical-electrical-optical conversions, limiting the network throughput. The only solution to this problem is to make these nodes all-optical by implementation of wavelength-routed optical networks.

The major WDM components to achieve this are multi/demultiplexers and wavelength routers. There are now two competitive multiplexing technologies for high channel count (>16) networks: planar optics demultiplexers, mainly focused on arrayed waveguide gratings (AWG) and free-space devices using traditional diffraction grating and imaging optics. AWG demultiplexers are integrated, smaller and cheaper, whilst free-space

devices potentially have superior performance characteristics such as crosstalk and insertion losses and do not require active temperature control.

The main aim of the research described in this thesis was to investigate how free-space concave diffraction gratings could be used as a basis of demultiplexers and routers in WDM optical networks. The major advantage of this approach is that a single optical element can perform both functions of dispersion and imaging in such devices as multi/demultiplexers, wavelength routers and channel equalizers. In physical optics terms this problem can be formulated as follows: to find solutions for concave grating spectrograph with unit magnification and diffraction limited performance in a given spectral range (in this thesis - 1520-1570 nm) for the input source with numerical aperture ≥ 0.1. This value is selected to match with the numerical aperture of standard single mode optical fibres. The device should be insensitive to polarization, provide linear dispersion ≥ 0.05 mm/nm, and have low levels of stray light. In addition, it was necessary to develop an analytical and numerical method to enable the calculation of the transmission spectrum of each demultiplexer or wavelength router channel, taking into account the contributions from aberrations, diffraction at the aperture and fibre mode profile.

The secondary objectives were to design a holographic concave grating-based demultiplexer, wavelength router and channel equalizer and to analyze their performance characteristics.

The basic theoretical and computer simulation research for this thesis was carried out at University College London in 1995-1998. The main experimental measurements were made in E-Tek Dynamics (San Jose, California, USA) in 1999-2000; although experimental work based on the analysis and designs described, also continued in the Optical Networks Group at UCL under the EPSRC 'PHOTON' project (2000-2003)

1.2 Structure of the thesis

The **second chapter** describes the basic concept of WDM optical networks and reviews related works in the field of wavelength demultiplexing. Comparative analysis of different published methods and techniques used for channel separation and wavelength routing is presented. Free-space, and especially concave grating-based, demultiplexers are reviewed in more detail.

Chapter three deals with analysis of crosstalk in free-space demultiplexers due to diffraction at the aperture, aberrations and diffuse scattering. The necessity of using the exact fibre mode solution for the crosstalk calculations instead of its Gaussian approximation is identified and examined. The analysis of aberrations demonstrated that crosstalk is most sensitive to the spherical aberration in the dispersion direction. Diffraction at the aperture was analysed experimentally and with a computer simulation for three different aperture shapes. It was shown that the best crosstalk performance could be achieved with a diamond aperture.

In addition, the crosstalk in wavelength routers is analyzed to estimate the router scalability. A simple formula estimating the power penalty due to simultaneous increase in the number of ports and the geometrical size of wavelength routers is derived. The scalability is strongly dependent on the aperture shape and the type of grating. It was shown that holographic grating-based routers with circular and diamond aperture are absolutely scalable from the crosstalk point of view and, hence, have the greatest potential for applications in densely spaced WDM networks.

Chapter four describes the general approach to the design of concave grating demultiplexers through the analysis and control of aberrations. Namely, it shows how input and output fibres must be mounted relative to the grating to provide minimum aberrations within the operating spectral range. General analytic formulae that define the parameters of concave grating mounts providing stationary and superstationary astigmatism are derived for the first time. Some novel and previously described special cases of stationary anastigmatic (SA) mounts are presented. Numerical simulations demonstrate that these mounts present diffraction-limited imaging within operating spectral range of WDM demultiplexers. Additional modification of SA spectrograph into a novel retroreflective scheme by introducing a convex mirror concentric to the intermediate image is described. The considerable advantages of this modification lie in (a) much wider image field in the sagittal direction providing the large number of parallel multi/demultiplexers, (b) a factor of two higher dispersion, (c) substantial further compensation of the chromatic astigmatism.

Chapter five describes in details all stages of design and assembly of an athermal concave holographic grating demultiplexer for 49 wavelength channels. An accurate method to calculate the transmission spectrum for each channel of the free-space demultiplexer is developed. The technique for the optimization of holographic recording schemes is described in detail. The grating period and the profile depth were chosen to

minimize the difference in diffraction efficiencies for S- and P-polarizations across the operating spectral range. To obtain flat and wide passband, input fibre was pigtailed to a short multimode waveguide, the design of which is also optimised. In addition, the tolerances and environmental stability are analyzed. The experimentally measured performance characteristics of a packaged device are presented

Chapter six focuses on the design and analysis of 91x91 router based on SA Littrow mount, selected from mounts found and analysed in Chapter 4. In this mount the incidence and diffraction angles are close to 30° and the arrays of input and output fibres are fixed one under another and separated by the dispersion plane. The holographic recording scheme was optimized to balance coupling losses within all 91x91 routes to below 0.8 dB. The advantages and shortcomings of two different approaches for realization of full-mesh routing are analyzed. In the first case 91 wavelengths and 181 output fibres are used, whilst the second method requires 181 wavelengths and 91 fibres.

Chapter seven describes the design, analysis and experimental verifications of WDM channel equalizer based on concave grating. In this device wavelength channels are separated at the image surface by dispersion, attenuated by a MEMS (micro-electro-mechanical system), reflected back and coupled into a single output fibre. It is demonstrated that due to compensation of the odd aberration terms, root-mean-square wave-front variance in this retro-reflective optical scheme does not exceed $\lambda/100$. Introducing a quarter-wave plate in the front of MEMS achieves a reduction of PDL by the factor of 7.

Chapter eight presents a novel effective method of flattening and broadening demultiplexer passband. This method provides complete compensation of dispersion within each WDM channel and allows spectral efficiency of 90% with extremely low crosstalk level.

Chapter nine presents a summary of the main conclusions of the research, and provides suggestions for future work.

1.3 Original contributions

The original contributions included in this thesis are:

- Analysis of aberrations in the optical system with one-to-one imaging of the fibre mode demonstrated that crosstalk in WDM devices is most sensitive to the spherical

aberration in the dispersion direction. The next aberration to be corrected to obtain improved crosstalk performance is meridional coma.

- The general analytic formulae that define the parameters of concave grating mounts, providing stationary and superstationary astigmatism have been derived. The spectral diagrams of the RMS wave aberrations demonstrate that the results presented can be readily used for design of diffraction-limited multi/demultiplexers for WDM networks.

- The stationary anastigmatic concave grating spectrograph has been modified into a novel retro-reflective scheme, by introducing a convex mirror, and analysed with ray-tracing software. The considerable advantages of this modification lie in a factor of two higher dispersion, and much larger image field without an increase of aberrations.

- Numerical and experimental analysis of the influence of aperture size and shape on crosstalk level in free-space WDM demultiplexers showed that the lowest crosstalk is provided by diamond aperture. For improved crosstalk performance, a circular aperture should be used to mask the square and rectangular gratings. A background crosstalk level of –60 dB is demonstrated experimentally for a holographic concave grating with a diamond aperture.

- The requirement for using the exact fibre mode solution for crosstalk calculations, instead of commonly used Gaussian approximation, which leads to an approximately 6 dB underestimation, was suggested and verified.

- Contribution to coherent crosstalk in wavelength routers from diffraction at the aperture and diffuse or in-plane scattering was analyzed. A simple formula estimating the power penalty due to simultaneous scaling up for the number of ports and the geometrical sizes of the device was derived. It was shown that holographic grating-based routers with circular and diamond aperture are absolutely scalable from the crosstalk point of view.

- A 49-channel demultiplexer based on stationary anastigmatic mount of a holographic concave grating with normal incidence onto the image plane was designed and experimentally investigated. A fully packaged, ready-to-use free-space concave grating demultiplexer was demonstrated for the first time. This was an athermal, flat-top passband, and low crosstalk device with polarization dependent losses less than 0.4 dB. A simple method developed for numerical calculations of transmission spectra for each demultiplexer channel demonstrated good agreement with experimental data.

- A 91x91 free-space wavelength router was designed, based on a stationary anastigmatic Littrow mount of a holographic concave grating with the longest dimension of 100 mm. Predicted performance included 1 dB bandwidth of 0.068 nm, less than 0.8 dB losses, and 1 dB power penalty due to coherent crosstalk. It was shown that full-mesh routing with 181 instead of 91 wavelengths results in much lower transmission losses and substantially simplifies the device.

- A concave grating power channel equalizer with extremely low polarization dependent losses, 25 dB dynamic range, 4.5 dB losses and 40 nm operating spectral range was designed and experimentally verified. The ray-tracing analysis showed that, due to double diffraction at the grating, aberrations are reduced by a factor of 6 compared to a single-pass optical scheme.

- A novel technique was developed for the realization of a flat top passband in WDM demultiplexers, allowing more than 90% spectral efficiency with very low crosstalk. The method is based on the cancellation of the wavelength-dependent image shift within the signal spectral window.

The following is a list of publications supporting original contributions and arising from work in this thesis at the time of submission, in chronological order, including conference presentations, letters, and papers:

F.N.Timofeev, J.E.Midwinter, P.Bayvel, E.G.Churin, A.Stavdas, M.N.Sokolskii, "Free-space aberration-corrected grating demultiplexer for application in densely-spaced,

subnanometre wavelength-routed optical networks", *IEE Electronics Letters*, vol.31, 1995, pp.1368-1370.

F.N. Timofeev, J.E. Midwinter, P. Bayvel, E.G.Churin, M.N. Sokolskii, "Free-space grating demultiplexer for densely-spaced, subnanometer wavelength-routed optical networks", Proceedings of the 1995 8th Annual Meeting of the IEEE Lasers and Electro-Optics Society. Part 2 (of 2), San Francisco, CA, USA, Oct 30-Nov 2 1995, (Conf. code 44261), pp.372-373

A.Stavdas, F.N.Timofeev, J.E.Midwinter, P.Bayvel, E.Churin, M.N.Sokolskii. "Free-space aberration-corrected diffraction grating demultiplexer for application in densely-spaced, subnanometer wavelength routed optical networks", *Proc. ECOC'95*, vol.2, 1995, pp.789-792.

E.G. Churin, P.Bayvel, J.E.Midwinter, A.M.Hill. "The influence of aperture size and shape on crosstalk level in free-space grating demultiplexers for WDM networks", *IEEE Photon. Technol. Lett.*, vol.8, 1996, pp.1337-1339.

F.N. Timofeev, P. Bayvel, E.G.Churin, J.E. Midwinter, "1.5 micron free-space grating multi/demultiplexer and routing switch", *IEE Electronics Letters*, vol.32, 1996, pp.1307-1308

E.G. Churin, P.Bayvel, A.Stavdas, J.E.Midwinter, A.M.Hill. "Optimization of Rowland circle mounts for grating demultiplexerrs and narrow-band spectrographs", *Optics Letters*, vol.21, 1996, pp.1084-1086.

F.N.Timofeev, P.Bayvel, E.G.Churin, P.Gambini, J.E.Midwinter. "Penalty-free operation of a concave free-space grating demultiplexer at 2.5 Gbit/s with 0.2-0.6 nm channel spacing", *Proc. ECOC'96*, vol.2, 1996, pp.321-324.

E.G.Churin, P.Bayvel, A.Stavdas, J.E.Midwinter, A.M.Hill. "Stationary anastigmatic mounts of concave gratings", *Applied Optics*, vol.36, 1997, pp.3444-3451.

F.N.Timofeev, P.Bayvel, E.G.Churin, V.B.Smirnitskii, V.V.Tsaturian, J.E.Midwinter "Free-space grating multi/demultiplexer and wavelength-router for densely spaced WDM networks", IEE Colloquium (Digest), 1997, No.036, p.5pp

E.G.Churin, P.Bayvel, J.E.Midwinter. "Optimized superstationary anastigmatic mounts of concave gratings", *Applied Optics*, vol.36, 1997, pp.4962-4964.

E.G.Churin, P.Bayvel, V.B.Smirnitskii, F.N.Timofeev, J.E.Midwinter "Concave grating and convex mirror double dispersion spectrograph for optical network applications", *Applied Optics*, vol.36, 1997, pp.7822-7825.

E. G. Churin, P. Bayvel. "Coherent crosstalk and scalability of free-space wavelength routers", *IEE Electronics Letters*, vol.34, 1998, pp.1225-1227.

E. G. Churin, P. Bayvel, "Free-space WDM router based on a new concave grating configuration", *Proc. ECOC'98,* vol.1, 1998, pp.239-240.

E. G. Churin, P. Bayvel, "Design of free-space WDM router based on holographic concave grating", *IEEE Photon. Technol. Lett.*, vol.11, 1999, pp.221-223.

F. N. Timofeev, E. G. Churin, P. Bayvel, V. Mikhailov, D. Rothnie, J. E. Midwinter, "Transmission passband, optical crosstalk and cascadability of free-space concave grating demultiplexer for dense WDM networks", *Optical and Quantum Electronics*, vol.31, 1999, pp.227-236.

E. G. Churin, P. Bayvel, "Passband flattening and broadening techniques for high spectral efficiency wavelength demultiplexers", *IEE Electronics Letters*, vol.35, 1999, pp. 27-28.

V. Mikhailov, P. Bayvel, E. G. Churin. "Low-crosstalk, loss and PDL grating demultiplexer for application in terabit WDM routed networks", *Proc. OFC'00,* 2000, paper WF3-1.

V. Mikhailov, P. Bayvel and E. G. Churin. "0.53 bit/s/Hz spectral efficiency free-space demultiplexer with very low crosstalk, loss and polarisation dependence", *IEE Electronics Letters*, vol.36, 2000, pp. 1640-1641.

Chapter 2

WDM demultiplexers and wavelength routers

2.1 Introduction

Optical fibre is now recognised as the most effective medium for high-capacity long-distance transmission in telecommunication networks [1]. The primary limit on the amount of data, which can be carried from point to point, is the available transmission bandwidth of the medium itself. The realisation that optical fibres could initially provide over 15 THz bandwidth, defined by very low losses spectral region of 1500-1620 nm (as shown in Figure 2.1), has stimulated one of the most buoyant research activities after development of

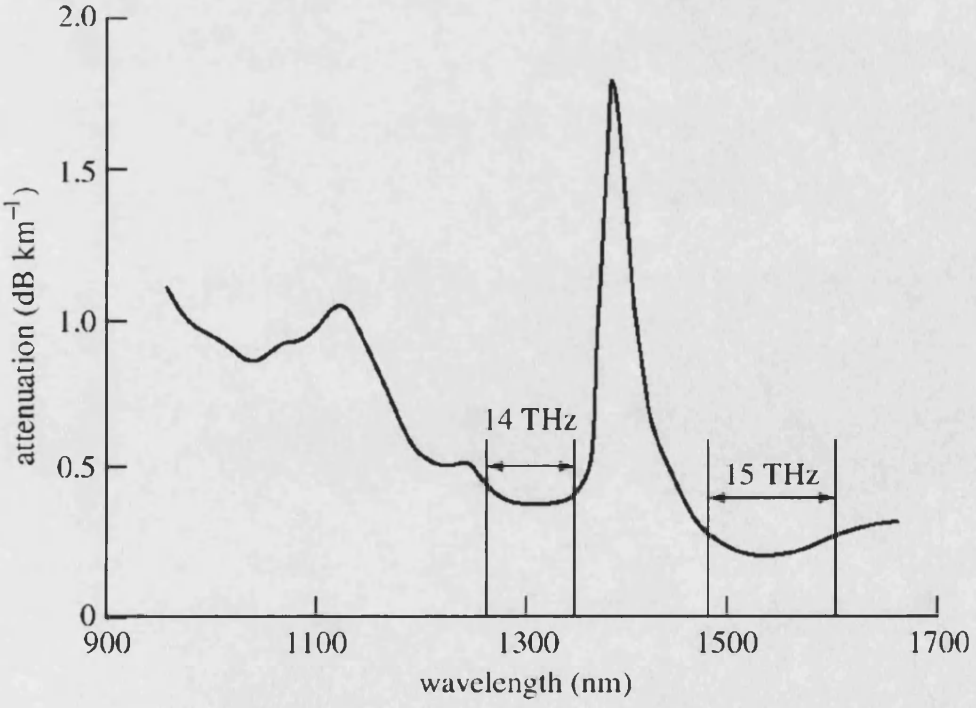

Fig.2.1. **Optical loss of fused silica single mode fibre versus wavelength.**

all-optical erbium-doped fibre amplifiers operating in the vicinity of 1550 nm [2]. The recent research on new Raman amplifiers [3] and new fibre dopants [4] to give amplification at 1300 nm is likely to open additional window of 14 THz (1250-1360 nm) in the future. Recent developments [5] in fibre fabrication technologies have resulted in the elimination of the water absorption peak around 1400 nm, yielding a low-loss operation of a single mode fibre over continuous region of 1300-1600 nm (about 40 THz). Thus the total potential bandwidth of optical fibre exceeds all the radio, high frequency and satellite spectra by several orders of magnitude.

Since the maximum bit-rate, which each user can transmit is limited by electronics speed, multiplexing techniques are required to make efficient use of the optical bandwidth [6]. Up-to-date modulators allow the modulation of light at the rate of 40 Gbit/s [7, 8], and commercial photo-receivers are becoming readily available to detect information at the rate of 40-45 Gbit/s [9,10].

Two approaches can be used to fill the huge reserve of the fibre bandwidth. The first method, known as optical time division multiplexing (OTDM), shown in Figure 2.2, would involve all-optical interleaving and regeneration of many lower bit-rate channels at 10 Gbit/s or higher all at the same wavelength, optically multiplexed to 100 Gbit/s and over [11, 12]. The interleaving would be performed by first generating different streams of very narrow pulses, say for a bit rate of 10 Gbit/s with a bit period of 100 ps, the pulse duration would be of the order of several picoseconds. Each stream to be multiplexed, would be separately modulated and delayed, using precise optical delays in free-space, optical fibre or waveguide (2 mm for a 10 ps delay in fibre or silica waveguide) with reference to the initial bit stream, generating a n x 10 Gbit/s aggregate bit rate.

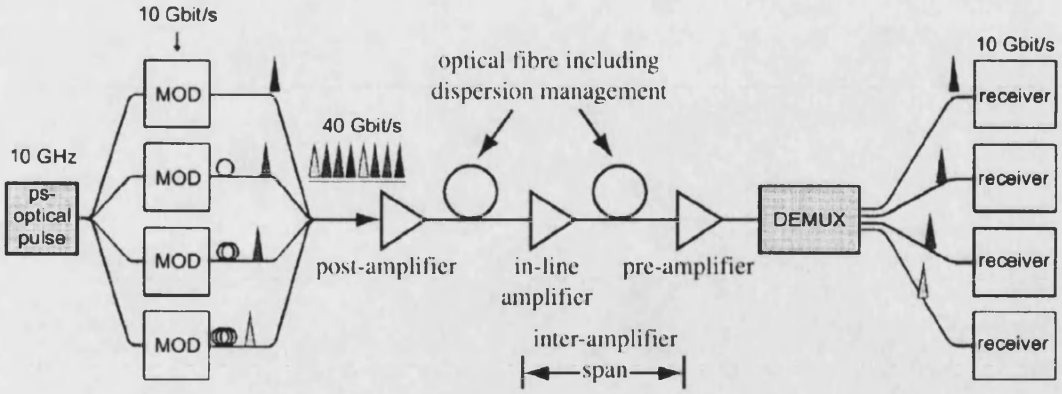

Fig.2.2. **Key building blocks of OTDM transmission**

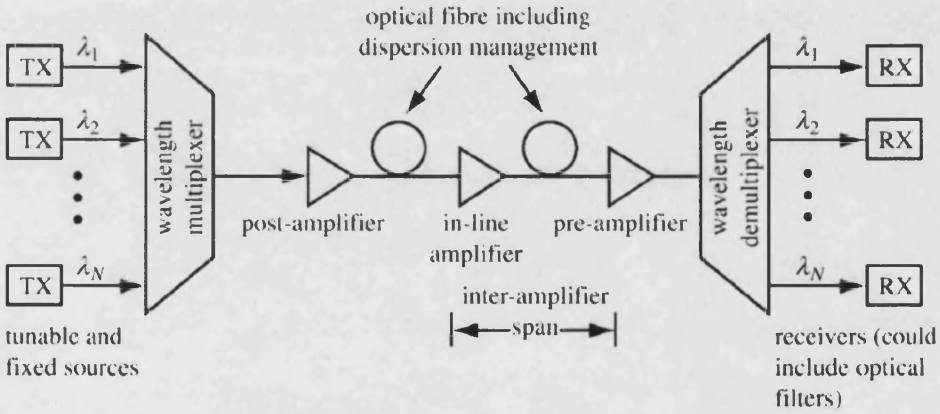

Fig.2.3. **Key building blocks of WDM transmission**

A second, competing, network approach, closely related to the subject of this thesis, known as wavelength division multiplexing (WDM), allows the spectrum to be sliced up into channels with a different wavelengths allocated to each channel (Figure 2.3), similar to the frequency division multiplexing in radio technology [13, 14]. The spectral efficiency with which fibre bandwidth can be accessed, measured in bits per second per hertz, is becoming important, since it defines how many channels with a given bit rate can be

'slotted-in' within the available spectrum. Fundamentally, the spectral efficiency is restricted by crosstalk between the neighbouring channels arising at the stage of demultiplexing and by the stability of single-frequency sources. The performance of WDM transmission system is often characterized by bit error rate (BER), which is required to be smaller than approximately 10^{-15} at the beginning of their life for most installed systems [15].

Besides the efficient use of fibre bandwidth, WDM technology provides an additional remarkable possibility of wavelength routing [16]. Wavelengths can be used to denote routing destinations [17], directing high-capacity all-optical signals, transparently, between source and destination nodes without the need for electronic processing [18]. This has the potential of significantly simplifying routing, processing and management of variable traffic types and demands in future, advanced optical networks.

The main question for WDM optical networks application is how many wavelengths, at what bit rate, and over which distance can successfully be transmitted without incurring errors through channel interactions caused by a combination of chromatic dispersion of the wavelength comb, crosstalk from imperfect selectivity of filters and fibre nonlinearities in long fibre length? Modest optical power used in transmission of several milliwatts per channel in single-mode optical fibres with core diameter of 8-10 μm give rise to intensities of the order of 1 GW/m^2, at which many optical nonlinearities become significant [19]. To answer this question, leading research laboratories around the world have competed to report the longest transmission distances with the highest bit-rate using cleverly optimised fibre dispersion, channel spacing and inter-amplifier distance. The recent achievements in transmission experiments, reported at the two key conferences in the field: European Conference on Optical Communications (ECOC) and Optical Fibre Communications Conference (OFC), are summarised in a Table 2.1. The highest bandwidth 'hero' experiment has exceeded 10

Tbit/s with 256 WDM channels for 300 km distance by Frignac *et al.* (2002). The mean channel separation of 66.7 GHz and the bit rate per channel of 42.7 Gbit/s result in a spectral efficiency of 0.64 bit/s/Hz.

Table 2.1 highlights the conflict between high bit-rate and achievable transmission distances. For local networks with distances about a hundred of kilometres the fundamental limitations on the bit rate are imposed by crosstalk between channels and finite receiver sensitivity, limited by the shot (quantum) noise. For intercontinental fibre cables with the length around ten thousands kilometres, accumulated errors due to chromatic dispersion, fibre nonlinearities, and optical amplifiers noise impose additional limitations on achievable bit rate. 3.73 Tbit/s over 11,000 km, reported by Cai *et al.* (2003), corresponds to transporting of 100,000 volumes of encyclopaedia in a second across the ocean [20], or can support one billion intercontinental telephone conversations simultaneously.

Author	Number of channels	Bit rate per channel (Gbit/s)	Total bit rat (Tbit/s)	Distance (km)
Cai [OFC'2002]	38	40	1.52	6200
Rasmussen [ECOC'2002]	40	42.7	1.71	5200
Tsuritani [OFC'2003]	40	42.7	1.71	8700
Zhu [ECOC'2002]	80	42.7	3.42	5200
Grosz [ECOC'2002]	128	42.7	5.47	1280
Charlet [ECOC'2002]	159	42.7	6.79	2100
Vareille [OFC'2003]	185	10.7	1.98	8370
Foursa [OFC'2002]	256	10	2.56	11000
Frignac [OFC'2002]	256	42.7	10.93	300
Cai [OFC'2003]	373	10	3.73	11000
Tanaka [ECOC'2002]	1001	10	10.01	120

Table 2.1: Recent WDM record transmission experiments.

2.2 Wavelength multiplexing technologies

The key components of WDM are wavelength multiplexers and demultiplexers, since they represent the means for wavelength channels to enter and exit the optical network. The main function of a demultiplexer is to receive from a fibre a beam consisting of multiple optical frequencies and separate it into its frequency components, which are coupled to as many individual fibres as there are frequencies. A multiplexer functions exactly in the opposite manner. It receives many optical wavelengths from many fibres and combines them into a single fibre. Due to the optical reciprocity, the same device can be used both as multi- and demultiplexer. However, it is much easier to design and produce a multiplexer, because it has no requirements on the level of crosstalk between wavelength channels.

Besides the number of wavelength channels and channel spacing, there are also five key parameters, which characterize the demultiplexer performance, namely: insertion loss, crosstalk, polarization dependent losses (PDL), passband shape and thermal stability. It is important to understand the implications of these on network performance, cost and reliability.

Insertion loss is one of the most important specifications in determining the maximum distance between network nodes. It is the ratio of the powers at the input and output for each channel of the demultiplexer device, expressed in dBs. Insertion losses directly impact the power budget of a WDM link, influencing the need for optical amplifiers. Amplifier-free links are possible in metro and access networks since they have shorter inter-node distances (typically less than 80 kilometres) than long-haul networks. Reducing the number of amplifiers results in lower costs and avoids the operational and

design complexities that are a consequence of their use such as noise, power balancing, and gain tilt [21]. Demultiplexer technologies that offer low insertion losses are more likely to reduce the dependence on amplifiers.

Crosstalk, expressed in dBs, is the relative power level added to the signal from adjacent and non-adjacent channels at the demultiplexer output [22]. Crosstalk degrades the signal-to-noise ratio and consequently the BER, and thus the quality of service. Demultiplexers with poor crosstalk performance require additional spectral filtering at the receiver side.

PDL, expressed in dBs, refers to the maximum or worst-case variation in the insertion loss, across the defined passband, as the state of polarization of the incident signal is varied over all orientations. The polarization of light propagating through a fibre is indeterminate; it can vary across the signal bandwidth resulting in increased BER for systems with high PDL [23].

The passband shape refers to the profile of the spectral response for each demultiplexer channel. The two most commonly known spectral response types are Gaussian (parabolic top) and the so-called "flat-top". The Gaussian passband shape implies strict limitation on demultiplexer spectral efficiency and on the drift of the transmitter wavelength. Network designers have addressed this issue by adding expensive wavelength lockers [24, 25] to transmitters. Demultiplexer manufactures have introduced flat passband devices that relax the need to control the transmitter wavelength to a precise value. Flat passband shape requires additional elements [26, 27] in the optical path that results in greater insertion loss.

Another important demultiplexer characteristic is its thermal behaviour. Some technologies, such as those based on arrayed waveguide gratings, are very temperature sensitive and require the use of heaters that keep the waveguide chip at a controlled temperature of approximately 75°C [28]. Growing demands on network reliability has favoured the use of passive devices that do not require power or temperature control elements. If the performance parameters, such as wavelength and insertion loss, are below some defined critical values over the operating temperature, the device is said to be *athermal*. For a demultiplexer to be athermal, its thermal wavelength stability should be better than 1 pm/°C and temperature-dependent insertion loss should be smaller than 0.015 dB/°C [29].

There are four main demultiplexer technologies: thin film filters [30], fibre Bragg gratings [31, 32], arrayed waveguide gratings [33] and free-space diffraction gratings [34]. Thin film filters and fibre Bragg gratings were first used in WDM systems when wavelength counts were low. Although they use different physical mechanisms, they both function by filtering wavelengths serially, where individual elements are used to multiplex (or demultiplex) wavelengths on a one-by-one basis. Thin film filters use a concatenated set of individual interference filters as shown in Fig. 2.4. Each filter has multiple dielectric coatings that pass a single wavelength and reflect all the others. This works well for low channel counts but have limitations at higher counts (typically greater than 16) due to size and accumulated insertion losses.

Fibre Bragg gratings rely on a grating formed in the fibre core that reflects a single wavelength and transmits other wavelengths. They are characterized by highly customized filter profiles. Each grating is designed with a different period to demultiplex a single wavelength in the system. The reflected wavelength is demultiplexed from the fibre using an optical circulator as shown in Fig. 2.5. As was the case for thin film filters, the serial

process restricts the practical channel count due to size, accumulated insertion losses and cost of the individual piece parts.

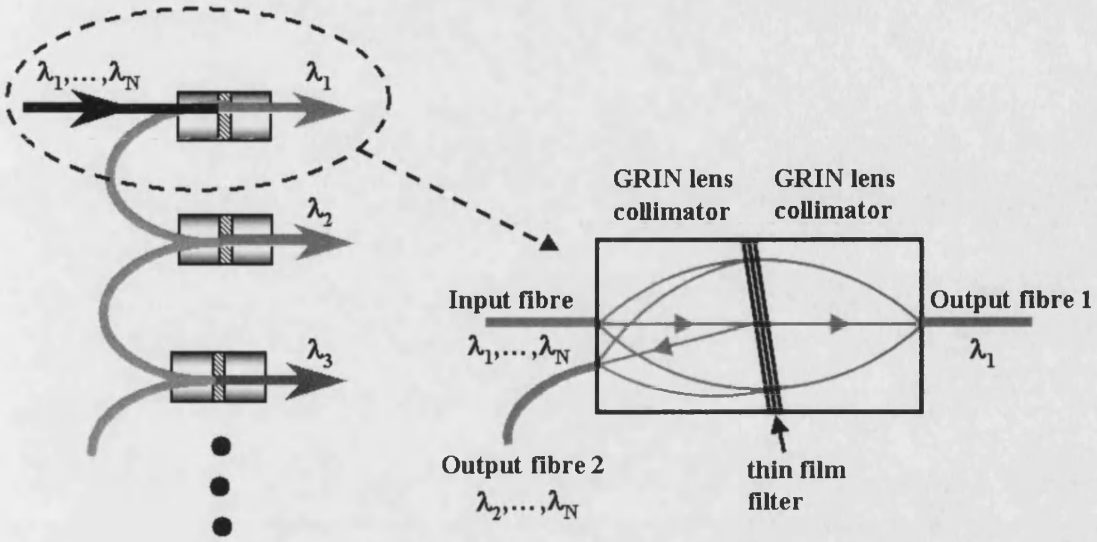

Fig.2.4. **Thin film demultiplexer.**

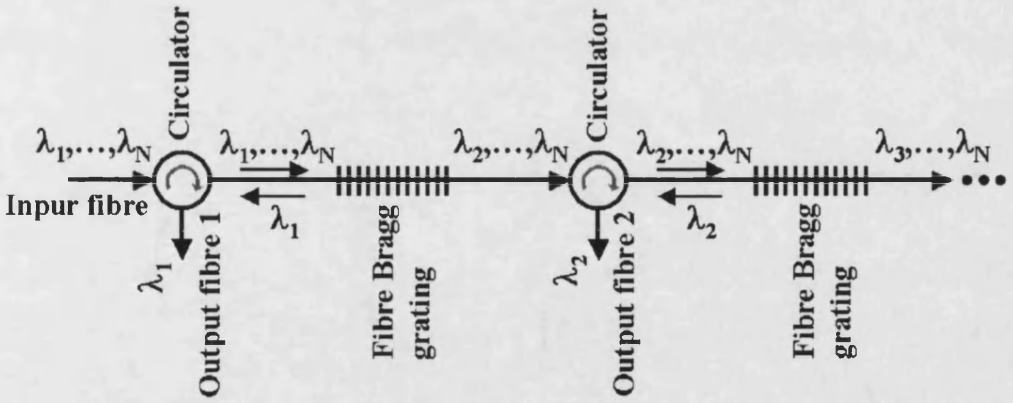

Fig.2.5. **Fibre Bragg grating demultiplexer.**

In contrast to thin film filters and fibre Bragg gratings, arrayed waveguide gratings (AWGs) and free-space diffraction gratings (FSDGs) systems use a parallel approach that is more conducive to high channel count applications. Silica- and InP-based AWGs have been proposed as the next generation of demultiplexers, and they dominate high-channel-count applications in long-haul networks. Fig. 2.6 shows the schematic layout of AWG demultiplexer. A multi-wavelength beam from the transmitter waveguide enters the free

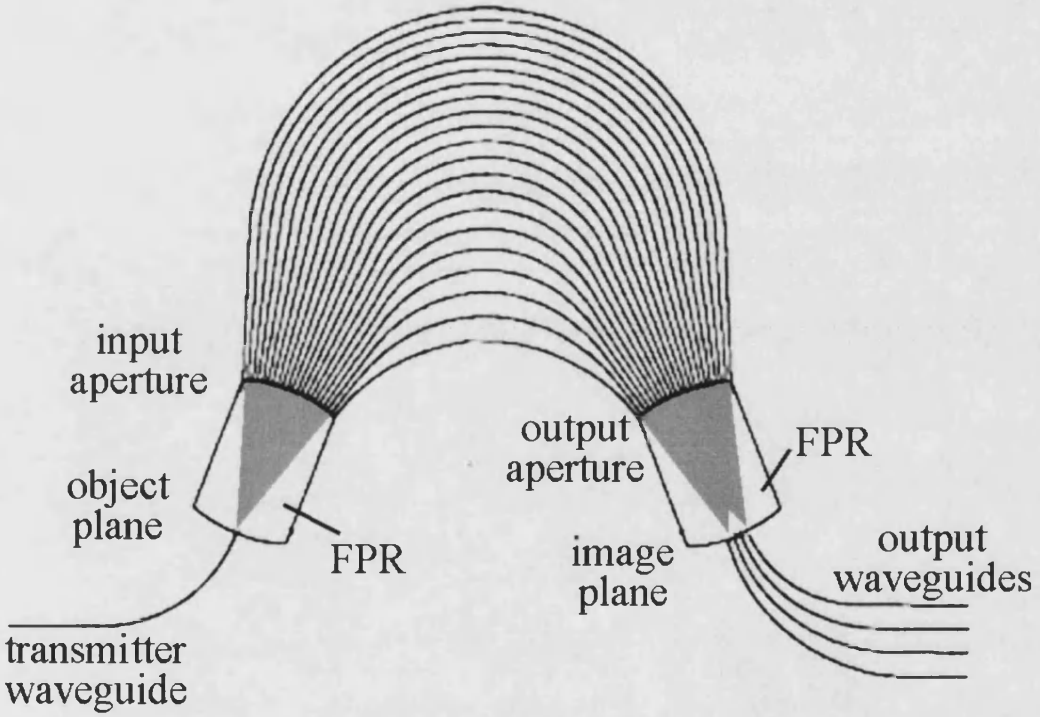

Fig.2.6. **Array waveguide grating demultiplexer**

propagation region (FPR) and becomes divergent. At the input aperture the beam is coupled to the waveguides' array and propagates to the output aperture. The length of the array waveguides is chosen such that the optical path length difference between adjacent waveguides equals an integer multiple of the central wavelength of the demultiplexer. The initial divergent beam at the central wavelength is transformed into a convergent one at the

output aperture, and coupled into the central output waveguide. The dispersion of the AWG is due to the linearly increasing length of the array waveguides, which causes the phase change induced by a change in the wavelength to vary linearly along the output aperture. As a consequence, the outgoing beam at another wavelength is tilted and coupled to another output waveguide.

Integration of AWG demultiplexers with other elements is promising, but performing such integration remains highly complex. AWGs are often designed to optimise one of the performance criteria (low loss [35], flat top [36, 37], low PDL [38, 39], athermal [40, 41]) and do not commonly offer all features in a single device. As mentioned previously, AWGs use internal heaters to maintain the waveguide chip at a constant temperature. System designers using AWGs must add heater control circuitry that introduces cost, size and complexity in the system. From a reliability standpoint a heater failure has a significant network impact since all wavelengths will be affected. Athermal versions of AWGs are emerging, however, these devices typically have higher insertion losses than their heated counterparts. Another problem with AWG demultiplexers is intrinsically high level of crosstalk [42] due to two-dimensional nature of the device, as will be discussed in Chapter 3.

FSDG demultiplexers [43, 44] can be implemented using ruled or holographic, plane or concave diffraction gratings as the dispersion element to separate wavelengths into individual output fibres. Ruled diffraction gratings scatter much more light in the dispersion plane compared to holographic ones [45] resulting in higher crosstalk level. The FSDG demultiplexers are based on classical optics principles and operate in free space. Basically, they are spectrographs designed to operate over a relatively narrow spectral range. The basic elements are the input fibre, output fibres array, collimating lenses and plane diffraction grating as shown in Fig. 2.7.

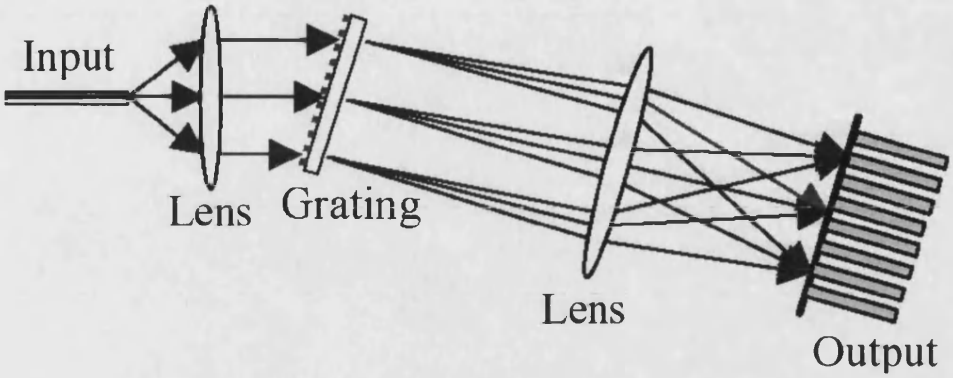

Fig.2.7. **Layout of typical free-space diffraction grating demultiplexer**

The main challenge for free-space demultiplexers is to combat the grating PDL, caused by the difference in diffraction efficiencies for P- and S- polarizations. Within the WDM C-band (1525-1565 nm), 550-600 lines/mm holographic gratings with a reflective metallized sinusoidal profile can achieve diffraction efficiencies of around 70% and PDL<0.4 dB [46, 47]. The recently developed volume holographic transmission gratings [48] with very deep refractive index modulation and frequency of 940 lines/mm give diffraction efficiency >87% and PDL<0.2 dB within C-band. These gratings have one shortcoming: they are holographically recorded in very hygroscopic material (gelatin) and need to be hermetically sealed between two glass substrates.

Through advanced optical and mechanical designs that compensate refractive index changes and mechanical thermal expansion, FSDG can be engineered to be insensitive to temperature variations. Also, recent improvements in multi-fibre array manufacturing (ZYGO Corporation) have enabled high yield production of high channel counts. FSDG demultiplexers offer performance advantages compared with AWG-based solutions because they can simultaneously achieve low insertion loss, flat filter profiles, low

crosstalk and superior thermal performance. For instance, athermal, flat top FSDG can achieve insertion losses <4dB compared with typical 7 dB for flat top AWG [36]. FSDGs are totally passive in operation, requiring no built-in heaters because their optical designs are inherently insensitive to temperature.

Advantages and shortcomings of multiplexing technologies are summarized in a Table 2.2.

Demultiplexer type	Advantages	Shortcomings
Thin film filters	Versatile and mature. Low cost for wide spacing. Good temperature stability. Low PDL.	Loss and cost scale with channel count. Long lead times.
Fibre Bragg gratings	High selectivity. Narrow spacing available. Short lead time possible. Flexible passband shape.	Requires circulator. Loss and cost scale with channel count. High dispersion.
AWGs	Can be integrated. Lowest cost For high channel-count modules.	High crosstalk and insertion loss. Requires active temperature control. Substantial PDL.
Free-space diffraction gratings	Low cost. Wide wavelength range. High uniformity. Lowest crosstalk. Good temperature stability.	Large size. Packaging issues. Moderate PDL.

Table 2.2: Summary of WDM multiplexing technologies.

2.3 Free-space plane grating demultiplexers

The intense development and investigation of FSDG multiplexing technique since the early 1980's resulted in numerous publications. The most reliable designs, reviewed below, were realized in commercially available free-space demultiplexers. The devices with the best performance parameters based on a plane diffraction grating have been proposed by Highwave Optical Technologies, Nettest and Bayspec. The Highwave demultiplexer is based on so-called "Stimax" configuration proposed by Laude *et. al.* [49]

in the 1980's. In reality it is difficult to call this device a free-space, because the light always propagates in bulk glass as shown in Fig. 2.8. The diffraction grating is embedded in a mono-block of silica, and the optical fibres are directly fixed to the block through the

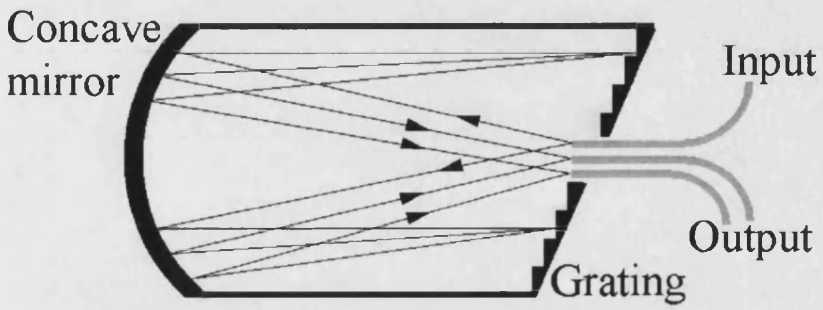

Fig.2.8. **Highwave demultiplexer**

grating centre. The concave mirror transforms the diverging beam from the input fibre into a parallel beam. The beam is then incident on the grating and is angularly dispersed back to the concave mirror where it is imaged onto the output fibres. Initially the device showed poor thermal stability (wavelength drift 14 pm/°C) due to high thermal expansion coefficient and refractive index temperature dependence. Additional compensating elements introduced later [50] to the glass bulk reduced wavelength drift to 1 pm/°C.

The Nettest device [51] is a retro-reflective scheme, shown in Fig.2.9, with double diffraction at the grating. PDL is suppressed by splitting the two orthogonal polarizations into two parallel beams with a birefringent walk-off crystal. A $\lambda/2$ plate in the S-polarized beam allows always using the grating with P-polarization. After diffraction at the grating, the directions of the two beams are reversed by a 180° folding prism, acting as a dihedral retro-reflector, and they follow exactly the same path in opposite directions, with the spread

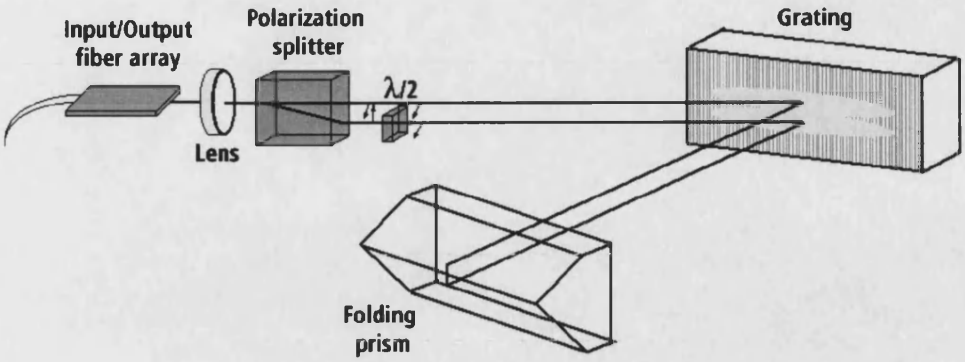

Fig.2.9. **Nettest demultiplexer**

spectrum refocused on the array of the output fibres. Additional optimized phase filter was inserted later [52] on the optical path of this scheme to achieve a flat top passband. A high PDL of grating in this approach is compensated at the expense of a number of additional elements and, therefore, increasing the device complexity and cost.

The Bayspec demultiplexer [53] is based on traditional configuration (see Fig. 2.7) with a volume phase transmission grating [48] as a dispersive element. In another modification [54] a double-pass optical scheme, shown in Fig. 2.10a, is employed to

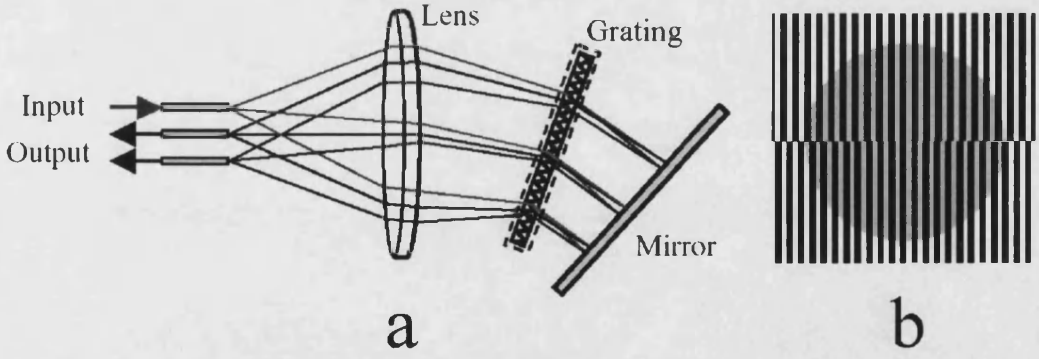

Fig.2.10. **Bayspec demultiplexer (a) and split grating (b)**

increase the angular dispersion, and, therefore, to decrease device dimensions. To obtain a flat top spectral response they use two gratings on the same substrate with slightly different spatial frequencies, depicted in Fig. 2.10b. The upper and lower parts of the incident beam are split angularly after diffraction, resulting in a double image at the output fibres' facets.

Performance characteristics for flat passband modifications of these three demultiplexers, designed to operate with 100 GHz spaced channels, are summarized in Table 2.3.

Parameters: \ Supplier:	Highwave	Nettest	Bayspec
Channel number	48	40	40
Insertion loss (dB)	9	5.5	5
0.5 dB Bandwidth (nm)	-	-	0.3
1 dB Bandwidth (nm)	>0.15	0.22	0.36
PDL (dB)	0.5	0.4	0.3
Adjacent channel crosstalk (dB)	-25	-30	-30
Non-adjacent channel crosstalk (dB)	-32	-	-35
Cumulative crosstalk	-22	-23	-25
Operating temperature (°C)	-20 +70	-10 +65	0 +70
Thermal wavelength drift (pm/°C)	1	1.4	0.5
Dimensions mm^3	160x30x30	148x68x26	105x75x16

Table 2.3: Performance characteristics of available free-space demultiplexers.

2.4 The concave grating demultiplexers

Since their invention by Henry Rowland in 1883, concave diffraction gratings have played an important role in spectrometry. Compared with plane gratings, they offer one significant advantage of combining the dispersive and focusing (imaging) properties that otherwise must be provided by separate optical elements. Until the end of 1960's only ruled (conventional) concave gratings were produced. The theory for ruled gratings was

developed by Zernike and Beutler [55]. There is a comprehensive review by Welford [56] on conventional concave gratings and their mounts.

With the development of laser technology, the first holographic gratings were produced in 1960's [57, 58]. Much lower stray light in comparison to ruled gratings has encouraged wide application of holographic gratings. They are easily fabricated with frequencies from 300 to 5000 gr/mm, produced in large sizes, and can be formed on steep concave surfaces which are otherwise very difficult to rule conventionally. The theory of holographic concave grating was first given by Cordelle *et al.* [59] for a system with a plane of symmetry. Aberration terms up to the fourth order, which include spherical aberration, were given by Namioka et al. [60]. There is a detailed review by Chrisp [61] on holographic concave gratings and their mounts.

The idea to make concave grating demultiplexer, based on a single optical element, as shown in Fig. 2.11, is very attractive, and is an extension of many years' research and

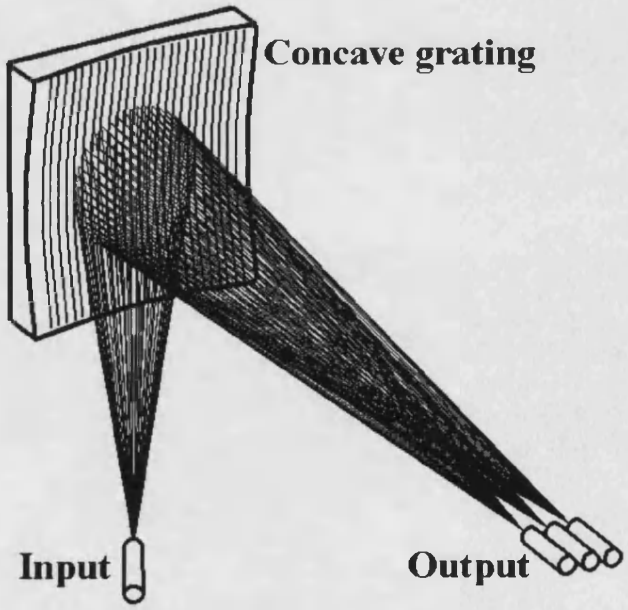

Fig.2.11. **Concave grating demultiplexer**

development of concave grating spectrographs for different applications. The first attempts to create such type of demultiplexer based on conventional ruled grating with frequencies 300-1000 gr/mm were made in the 1980's [62-65] at the earliest stage of the optical networks' era. These were the so-called "coarse" devices for transmitting low bit rate signal over very short distances operating with multi-mode fibres (core diameter 60-200 μm) in a wavelength range 700-900 nm. The number of channels varied from six to ten with a channel spacing of 20-30 nm. At that time such an important characteristic, as PDL was not even considered. Aberrations were also not a significant issue due to wide core of multimode fibres, and the image quality of those demultiplexers across the operating spectral range was far from diffraction limited. Further development of optical telecommunications technologies resulted in a shift to 1550 nm, much closer channel spacing, longer transmission distances, and the use of single mode fibres. This placed much stricter requirements on the performance characteristics of wavelength demultiplexers, and concave grating devices developed in the eighties for multi-mode fibres became obsolete.

To consider the use of a concave grating for demultiplexing in modern WDM networks it was necessary to turn from ruled to holographic gratings for lower crosstalk, to choose a proper grating frequency to achieve a low PDL, to find new mountings providing diffraction limited performance within the operating spectral range and to optimize the holographic recording scheme. The investigation of these problems is the focus of this work. There appears to be no work preceding this thesis on the development of concave grating demultiplexers for single mode fibres and closely spaced wavelength channels. This is believed to be due to the difficulty in designing an aberration corrected and low PDL device necessary for this application. Traditionally, during the design of a concave holographic grating spectrograph, the optical scheme of the device and the holographic recording scheme are optimized simultaneously to obtain the minimum aberrations within

the operating spectral range. This is a very time consuming and difficult process. To reduce the complexity, the aberration analysis in this thesis is carried out in two steps. At the first stage, described in Chapter 4, an idealized concave grating is considered. This grating creates an aberration-free image of the point source at a single wavelength for any chosen source and image positions. Then the wave aberrations are calculated in the image plane for other wavelengths. This allows an analytical derivation of the source and image positions providing the best performance of an idealized grating within a given operating spectral range and, finally, defines the demultiplexer optical scheme. At the second stage (Chapter 5), the aberrations of a real holographic grating, recorded by two point sources are calculated for a chosen demultiplexer scheme, and minimized by varying positions of recording sources.

2.5 Wavelength routers

The principle of wavelength router operation can be understood from Fig. 2.12. The grating diffraction laws allow the design of a device with N input and $2N$-1 output fibres which is simultaneously a demultiplexer for each input fibre and a multiplexer for each output fibre. The same set of N channel wavelengths is used in each input fibre but at the device output the images of a spectral comb are shifted relative to each other by multiples of channel separation. All routes for signals S_{IJ} at I-th wavelength coming from J-th input fibre are shown in Fig. 2.12 for N=4. The output fibres are combined in couples and directed to N output port, each with N wavelengths. Such a device can be realized with a free-space diffraction grating [66-68] or AWG [69, 70] and is inconceivable with thin film filters and fibre Bragg gratings.

The main purpose of *NxN* wavelength router is to provide a full-mesh interconnection between *N* nodes without any optoelectronic switching and wavelength conversion [18]. This establishes the network node-pairs with end-to-end optical channels, resulting in

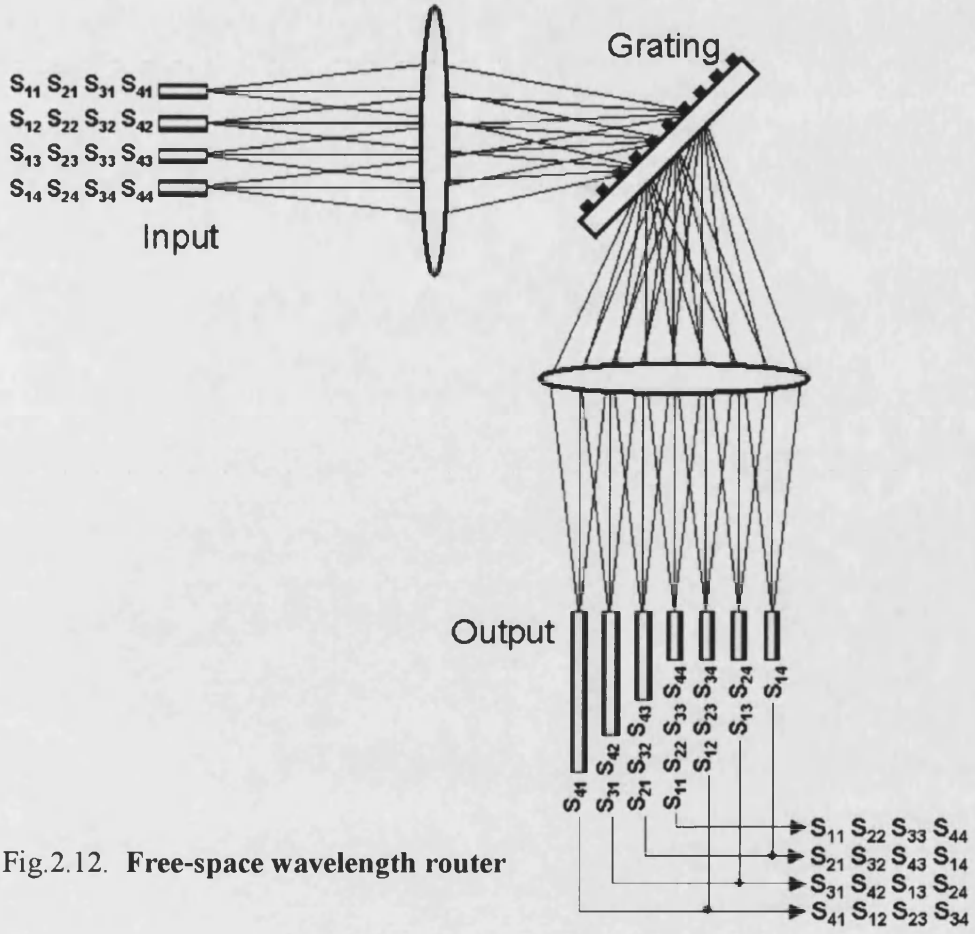

Fig.2.12. **Free-space wavelength router**

protocol transparency [71] and simplified management and processing compared to routing in systems using digital cross-connects [72]. Optical routers with a large number of ports (>32) have emerged as key elements for provisioning and restoration in future WDM networks.

The main problem with wavelength routers, compared to conventional demultiplexers, is coherent crosstalk (or beat noise) arising from the same wavelength re-

use within different ports. This crosstalk cannot be filtered at the receiver and implies strict limitations on the amount of stray light. Free-space optics provides significantly better crosstalk performance than integrated optics devices [66] and is much more expedient for the realization of high-capacity routers. The design of a router must be focused, in the first place, on the suppression of all possible crosstalk origins described in Chapter 3, such as the aberrations, diffraction at the aperture, and diffuse scattering at the optical surfaces. The only published design of concave grating router and detailed description of its operation are presented in Chapter 6.

2.6 Summary

A brief introduction to WDM optical networks is presented, and different technologies of wavelength demultiplexing and routing are described and compared. Free-space, and especially concave grating-based demultiplexers are reviewed in detail. This chapter places the subject of thesis in the context of the vast area of optical communications as follows: Optical networks → WDM → Demultiplexing techniques → Free-space approach → Concave grating devices. The following chapters describe the many problems addressed in the thesis, which need to be investigated and solved for achieving reliable and simple WDM devices based on concave gratings. Specifically this requires minimization of chromatic aberrations of concave grating, optimization of holographic recording scheme, accurate analysis of crosstalk, compensation of polarization dependence and investigation of many other collateral problems, which formed the main subject of this thesis, and which were successfully achieved.

References to Chapter 2:

[1] P. Bayvel, "Future high-capacity optical telecommunication networks", *Phil. Trans. R. Soc. Lond. A*, vol.358, 2000, pp.303-329.

[2] B. J. Ainslie, "A review of the fabrication and properties of erbium-doped fibres for optical amplifiers," *J. Lightwave Technol.*, vol.9, 1991, pp.220-227.

[3] C. R. S. Fludger, V. Handerek, R. J. Mears, "Ultra-wide bandwidth Raman amplifiers", *Proc. OFC 2002*, paper TuJ3.

[4] B. N. Samson, J. A. Medeiros, R. I. Neto, R. I. Laming, and D. W. Hewak, "Dyprosium doped Ga:La:S glass for a efficient optical fibre amplifier operating at 1.3 μm," *IEE Electronics Letters*, vol.30, 1994, pp. 1617-1619.

[5] A. K. Srivastava, D. L. Tzeng, A. J. Stentz, J. E. Johnson, M. L. Pearsall, O. Mizuhara, T. A. Strasser, K. F. Dreyer, J. W. Sulhoff, L. Zhang, P. D. Yates, J. R. Pedrazzani, A. M. Sergent, R. E. Tench, J. M. Freund, T. V. Nguyen, H. Manzar, Y. Sun, C. Wolf, M. M. Choy, R. B. Kummer, D. Kalish, and A. R. Chraplyvy, "High-speed WDM transmission in all wave fibre in both the 1.4-μm and 1.55-μm Bands," in *OSA Tech. Dig., Optical Amplifiers and Their Applications,* Washington, DC, 1998.

[6] D. J. Mestdagh, "Multiple access techniques for fiber-optic networks", *Optical Fiber Technology*, vol.2, 1996, pp.7-54.

[7] A. Shen, J. Damon-Lacoste, M. Le Pallec, C. Duchet, J-L. Gentner, F. Devaux, and M. Renaud, "Low insertion loss and polarization-insensitive InP-based Mach-Zender modulator for 40 Gbit/s optical regeneration", *Proc. OFC 2002*, paper WV3.

[8] H. Feng, T. Makino, S. Ogita, H. Maruyama, and M. Kondo, "40 Gb/s Electro-absorption-modulator-integrated DFB laser with optimised design", *Proc. OFC 2002*, paper WV4.

[9] V. Hurm, "40 Gbit/s, 1.55 μm monolithic integrated GaAs based PIN-HEMT photoreceiver", *Proc. ECOC 1998*, vol.3, pp.119-121.

[10] A. Beling, D. Shmidt, H.-G. Bach, G.G. Mekonnen, R. Ziegler, V. Eisner, M.Stolberg, G. Jacumeit, E. Gottwald, C.-J. Weiske, A. Umbach, "High power 1550 nm twin-photodetector modules with 45 GHz bandwidth based on InP", *Proc. OFC 2002*, paper WN4.

[11] D. Cotter, R.J. Manning, K.J. Blow, A.D. Ellis, A.E. Kelly, D. Nesset, I.D. Phillips, A.J. Poustie, and D.C. Rodgers, "Nonlinear optics for high-speed digital information processing", *Science*, vol.286, 1999, pp.1523-1528.

[12] R. Ludwig, U. Feiste, C. Schmidt, C. Schubert, J. Berger, E. Hilliger, M. Kroh, T. Yamamoto, C. M. Weinert, H. G. Weber, "Enabling transmission at 160 Gbit/s", *Proc. OFC 2002*, paper TuA1.

[13] G. E. Kaiser, "A review of WDM technology and its applications", *Opt. Fib. Technol.*, vol. 5, 1999, p.3-10.

[14] I. P. Kaminow and T. L. Koch. Optical fiber telecommunications. Vols IIIA and IIIB. Academic Press, San Diego, 1999.

[15] N. Antoniades, A. Boskovic, I. Tomkos, N. Madamopoulos, M. Lee, I. Roudas, M. Sharma, and M. J. Yadlowsky, "Performance engineering and topological design of Metro WDM optical networks using computer simulation", *J. Lightwave Technol.*, vol.20, 2002, pp.149-165.

[16] G. R. Hill, "A wavelength routing approach to optical communication networks," *BT Technol. J.*, vol.6, 1988, pp.24-31.

[17] I. Chlamtac, A. Ganz, and G. Karmi, "Purely optical networks for terabit communication," in *Proc. IEEE INFOCOM 1989*, pp. 887-896.

[18] M. Young, H. Laor, and E. J. Fontenot, "First in-service network application of optical cross-connects," in *Proc. OFC 1998*, paper PD23.

[19] G. P. Agrawal, *Nonlinear fiber optics.* San Diego, Academic Press, 1995.

[20] S. V. Kartalopoulos, *Introduction to DWDM technology.* New York, IEEE Press, 2000.

[21] E. Desurvire. *Erbium doped fiber amplifiers: Principles and applications.* New York, Wiley, 1994.

[22] Y. Shen, K. Lu, and W. Gu, "Coherent and Incoherent crosstalk in WDM optical networks," *J. Lightwave Technol.*, vol.17, 1999, pp.759-764.

[23] E. Lichtman, "Limitations imposed by polarization-dependent gain and loss on all-optical ultra-long communication systems," *J. Lightwave Technol.*, vol.13, 1995, pp.906-913.

[24] D. M. Adams, C. Gamache, R. Finlay, M. Cyr, K. M. Burt, J. Evans, E. Jamroz, S. Wallace, I. Woods, L. Doran, P. Ayliffe, D. Goodchild, and C. Rogers, "Module packaged tunable laser and wavelength locker delivering 40 mW of fibre-coupled power on 34 channels," *IEE Electronics Letters*, vol.37, 2001, pp. 691-693.

[25] T. Haber, K. Hsu, C. Miller, and Y. Bao, "Tunable EDF Laser precisely locked to the 50 GHz ITU frequency grid," *Proc. ECOC 1999*, Paper Mo B2.4.

[26] M. R. Amersfoort, J. B. D. Soole, H. P. LeBlance, N. C. Andreadakis, A. Rajhel, and C. Caneau, "Passband broadening of integrated arrayed waveguide filters using multimode interference couplers," *IEE Electronics Letters*, vol.23, 1996, pp. 449-451.

[27] C. Dragone, T. Strasser, G. A. Bogert, L. W. Stulz, and P. Chou, "Waveguide grating router with maximally flat passband produced by spatial filtering," *IEE Electronics Letters*, vol.33, 1997, pp. 312-314.

[28] A. Kaneko, T. Goh, H. Yamada, T. Takana, and I. Ogawa, "Design and applications of silica-based planar lightwave circuits", *IEEE J. Select. Topics Quantum Electron.*, vol.5, 1999, pp.1227-1236.

[29] D. Yu, W. Yang, "VPG-Based DWDM MUX/DeMUX devices and specifications", White Paper, 2002:
http://downloads.lightreading.com/wplib/bayspec /BaySpec-VPG-DWDM.pdf

[30] M. A. Scobey and D. E. Spock, "Passive DWDM components using microplasma optical interference filters," *Proc. OFC 1996*, pp.242-243.

[31] N. Yusuke, Y. Shinji, "Realization of various superstructure fiber Bragg gratings for DWDM systems using multiple-phase-shift technique," *Proc. OFC 2002*, paper TuQ3.

[32] J. J. Pan, "0.4 nm channel spacing dense WDM multiplexers and demultiplexersnusing FBGs and bandpass filters", *Proc. OFC 1998*, p.184.

[33] M. K. Smit and C. van Dam, "Phaser-based WDM-devices: Principles, design and applications," *IEEE J. Select. Topics Quantum Electron.*, vol.2, 1996, pp.236-250.

[34] J. P. Laude. *Wavelength Division Multiplexing*. Prentice Hall, New York, 1993.

[35] C. van Dam, A. A. M. Staring, E. F. Jansen, J. J. M. Binsma, T. van Dongen, M. K. Smit, and B. H. Verbeek, "Loss reduction for phased-array demultiplexers using a double etch technique," *Integrated Photonics Research 1996,* Boston, MA, Apr. 29-May 2, 1996, pp. 52-55.

[36] K. Okamoto and A. Sugita, "Flat spectral response arrayed-waveguide grating multiplexer with parabolic waveguide horns," *IEE Electronics Letters*, vol.32, 1996, pp. 1661-1662.

[37] M. C. Parker, F. Farjady, and S. D. Walker, "Arrayed-waveguide grating passband flattening by combined phase and amplitude apodisation," *Proc. ECOC 1998,* pp.297-298.

[38] H. Takahashi, Y. Hibino, and I. Nishi, "Polarization-insensitive arrayed-waveguide grating wavelength multiplexer on silicon," *Optics Letters*, vol.17, 1992, pp.499-501.

[39] H. Bissessur, P. Pagnod-Rossiaux, R. Mestric, and B. Martin, "Extremely small polarization independent phased-array demultiplexers on InP," *IEEE Photon. Technol. Lett.*, vol.8, 1996, pp.554-556.

[40] H. Tanobe, Y. Kondo, "Temperature insensitive arrayed waveguide gratings on InP substrates," *IEEE Photon. Technol. Lett.*, vol.10, 1998, pp.235-237.

[41] N. Ooba, Y. Hibino, Y. Inoue and A. Sugita, "Athermal silica-based arrayed waveguide grating multiplexer using bimetal plate temperature compensator," *IEE Electronics Letters*, vol.36, 2000, pp. 1800-1801.

[42] H. Takahashi, K. Oda, and H. Toba, "Impact of Crosstalk in an Arrayed-Waveguide Multiplexer on NxN Optical Interconnection", *J. Lightwave Technol.*, vol.14, 1996, pp.1097-1105.

[43] M.C. Hutley, *Diffraction Gratings*. Academic Press, London, 1982.

[44] E. G. Loewen and E. Popov. *Diffraction gratings and applications*. Marcel Dekker, New York, 1997.

[45] J. F. Verrill, "The specification and measurement of scattered light from diffraction gratings," *Optica Acta*, vol.25, 1978, pp.531-547.

[46] M. C. Hutley, "Blazed interference diffraction grating for the ultra-violet" *Optica Acta*, vol.22, 1975, pp.1-13.

[47] E.G. Loewen, M. Neviere, and D. Maystre, " Grating efficiency theory as it applies to blazed and holographic gratings", *Applied Optics*, vol.16, 1977, pp.2711-2721.

[48] L. Dickson, "Volume diffraction gratings for wavelength division multiplexing," Wasatch Photonics, white paper, 2002:
http://www.wasatchphotonics.com/documents-%20word,%20pdf/gratingtutorial.pdf

[49] J. P. Laude and J. M. Lerner, "Wavelength division multiplexing/demultiplexing (WDM) using diffraction gratings", *Proc. of SPIE*, vol.503, 1984, pp.22-28.

[50] J P Laude, "Stable monoblock wavelength division multiplexers with channel spacing down to 0.5 nm usable as practical wavelength reference tools in optical fibre communication systems," *Pure and Applied Optics*, vol.3, 1994, pp.963-974.

[51] P. Martin, E. Taufflieb, B. Laloux, and H. C. Lefecre, "Optimized bulk-optic grating approach for D-WDM demultiplexers," *Proc. ECOC 1999*, Paper Mo D2.6.

[52] B. Chassagne, K. Aubry, A. Rocher, B. Herbette, V. Dentan, S. Bourzeix, P. Martin, P, "Passive athermal bulk-optic mux/demux with flat-top spectral response," in *Proc. ECOC 2001*, paper WeL2.1.

[53] D. Yu, J. Yang, J. Wang, L. Chen, C. Zhang, W. Yang, "Volume phase grating based flat-top passband response dense wavelength division multiplexers," *Proc. OFC 2002*, paper TuN4.

[54] W. Yang and S. Zhang, "Compact double-pass wavelength multiplexer-demultiplexer," US Patent No. 6,275,630 (August, 2001).

[55] H. Beutler, "The Theory of the Concave Grating", *J. Opt. Soc. Am.*, vol.35, 1945, pp.311-350.

[56] W. T. Welford, "Aberration theory of gratings and grating mountings", *Progress in Optics*, vol.4, 1965, pp.241-280.

[57] D. Rudolph, and G. Schmahl, *Umsch. Wiss. Tech.*, vol.67, 1967, p. 225-231.

[58] A. Labeyrie, and J. Flamand, "Spectrographic performance of holographically made diffraction gratings" *Opt. Commun.*, vol.1, 1969, pp.5-8.

[59] J. Cordelle, J. Flamand, G. Pieuchard, and A. Labeyrie, "Aberration-corrected concave gratings made holographically". In *Optical instruments and techniques* (J. Home Dickson, ed.), p. 117-124, Oriel Press, Newcastle-upon-Tyne, London, 1970.

[60] T. Namioka, H. Noda, and M. Seya, "Possibility of using the holographic concave grating in vacuum monochromators", *Sci. Light (Tokyo)*, vol.22, 1973, pp.77-99.

[61] M.P.Chrisp, "Aberration-Corrected Holographic Gratings and Their Mountings", in *Applied Optics and Optical Engineering*, R.R.Shannon and J.C.Wyant, eds. (Academic, London, 1987), vol.10, pp.391-454.

[62] R. Watanable, K. Nosu, "Optical Demultiplexer Using Concave Grating in 0.7-0.9 μm Wavelength Region", *IEE Electronics Letters*, vol.16, 1980, pp. 106-108.

[63] R. Watanable, K. Nosu, "Slab waveguide demultiplexer for multimode optical transmission", *Applied Optics*, vol.19, 1980, pp. 3588-3590.

[64] H. W. Yen, H. R. Friedrich, R. J. Morrison, G. L. Tangonan, "Planar Rowland spectrometer for fiber-optic wavelength demultiplexing", *Optics Letters*, vol.6, 1981, pp.639-641.

[65] T. Kita and T. Harada, "Use of aberration-corrected concave gratings in optical demultiplexers ", *Applied Optics*, vol.22, 1983, pp.819-825.

[66] A. M. Hill, S. Carter, J. Armitage, M. Shabeer, R. A. Harmon, and P. Rose, "A Scaleable and Switchless Optical Network Structure, Employing a Single 32x32 Free-Space Grating Multiplexer," *IEEE Photon. Technol. Lett.*, vol.8, 1996, pp.569-571.

[67] J.P. Laude, I. Long and D. Fessard, "Very dense N*N wavelength routers based on a new diffraction grating configuration", *Proc. ECOC 1997*, vol.3, pp.87-90.

[68] E. G. Churin, P. Bayvel, "Design of free-space WDM router based on holographic concave grating", *IEEE Photon. Technol. Lett.*, vol.11, 1999, pp.221-223.

[69] K. Okamoto, H. Hasegawa, O. Ishida, A. Himeno, and Y. Ohmori, "32x32 arrayed-waveguide grating multiplexer with uniform loss and cyclic frequency characteristics," *IEE Electronics Letters*, vol.33, 1997, pp. 1865-1866.

[70] K. A. McGreer, "Arrayed waveguide gratings for wavelength routing," *IEEE Communications Magazine*, December 1998, pp.62-68.

[71] O. Gerstel, "On the future of wavelength routing networks," *IEEE Network*, vol.10, 1996, pp.14-20.

[72] P. E. Jr. Green, "Optical networking update," *IEEE J. Select. Areas Commun.*, vol.14, 1996, pp.746-779.

Chapter 3

Crosstalk in free-space grating demultiplexers and wavelength routers

3.1 Introduction

Crosstalk between different channels is the main obstacle in the realization of wavelength demultiplexing and routing devices [1]. This phenomenon arises due to imperfect separation of wavelength channels at the output of demultiplexer or wavelength router. It is caused mainly by a combination of fibre mode tails, aberrations, diffraction at the truncated aperture and scattered light. Conventionally the inter-channel crosstalk is subdivided into two types: neighbouring channels crosstalk giving the highest contribution to the signal-to-noise ratio and the background crosstalk, with an approximately equal contribution from any nonadjacent channel.

Crosstalk in a single demultiplexer is incoherent because the difference in carrier frequencies for any two channels is much higher than the bit rate and the receiver bandwidth. This allows presentation of the crosstalk as a ratio of "parasitic" and "useful" light powers. Therefore, the cumulative (total) crosstalk for a given channel j in demultiplexer can be expressed in decibels as

$$Q_j = 10\log_{10}\left(\frac{1}{P_{jj}}\sum_{i\neq j} P_{ij}\right), \qquad (3.1)$$

where P_{ij} is the light power coupled from the channel i into channel j at the output of the demultiplexer.

For the case of a wavelength NxN router the requirements on channel isolation is much higher compared to demultiplexers. Incoherent crosstalk is not a problem in the wavelength router because the signal still requires demultiplexing and/or filtering before the receiver. However, the main problem in these devices is coherent crosstalk or beat-noise [2-5] caused by the same wavelength reuse within different ports. In a coherent case the accumulated beat noise can be estimated through summing all the amplitudes (assumed in phase for the worst case) of the parasitic light at the signal wavelength.

In this chapter, the three main mechanisms of crosstalk in free-space devices (aberrations, aperture truncation and scattered light) are analysed. The necessity to use exact fibre mode description instead of its Gaussian approximation for accurate calculations of crosstalk is demonstrated. The numerical simulations and experimental results for the influence of the aberrations, aperture size and shape on the crosstalk level in free-space demultiplexers are presented [6].

A simple formula estimating the power penalty due to scaling up the number of ports in a wavelength router is derived [7]. The scalability is shown to be strongly dependent on the aperture shape and the type of grating used as a dispersive element.

3.2 Fibre mode tails and validity of Gaussian approximation

The most obvious source of crosstalk is the coupling between the receivers through the tails of the fibre mode. This effect cannot be avoided by proper design, but can be reduced by

increasing the linear dispersion corresponding to a larger pitch between output fibres. However, this increases the system dimensions and decreases the spectral efficiency. The design of the demultiplexer always implies a trade-off between the useful bandwidth and crosstalk.

The Gaussian approximation for the fibre mode simplifies substantially [8] the calculations of the coupling efficiency into output fibre. The error typically does not exceed 0.1 dB. To estimate the accuracy of the Gaussian approach for crosstalk calculations consider the fundamental mode of the standard single-mode fibre (SMF), obtained in a weakly-guiding approximation [9] for wavelength λ_0=1550 nm, core radius a=4.15 μm, core and cladding refractive indexes n_1=1.4504, and n_2=1.4447, respectively. These data correspond to the normalized waveguide parameter $V = \frac{2\pi a}{\lambda_0}\sqrt{n_1^2 - n_2^2} = 2.162$, and numerical aperture 0.1 at e^{-2} intensity level. The fundamental modal field ψ as a function of the distance ρ from the fibre axis is given by

$$\psi(\rho) = \begin{cases} A\dfrac{J_0(U\rho/a)}{J_0(U)} & 0 < \rho \le a \\ A\dfrac{K_0(W\rho/a)}{K_0(W)} & \rho > a \end{cases}, \quad (3.2)$$

where J_0 is zero order Bessel function of the first kind, K_0 is zero order modified Bessel function of the second kind, $U = \sqrt{1 + 2\ln V} = 1.594$, $W = \sqrt{V^2 - U^2} = 1.460$, and A is a normalizing constant.

The overlap integral [9] between the fundamental mode and its best Gaussian approximation provides coupling of 99.3%, however, the tail difference, shown in Fig. 3.1a is dramatic. Fig. 3.1b shows far-field profile for this fibre mode and its Gaussian approximation calculated using a Fourier transform. After passing through real optical system the tails amplitudes are generally increased due to diffraction at the aperture.

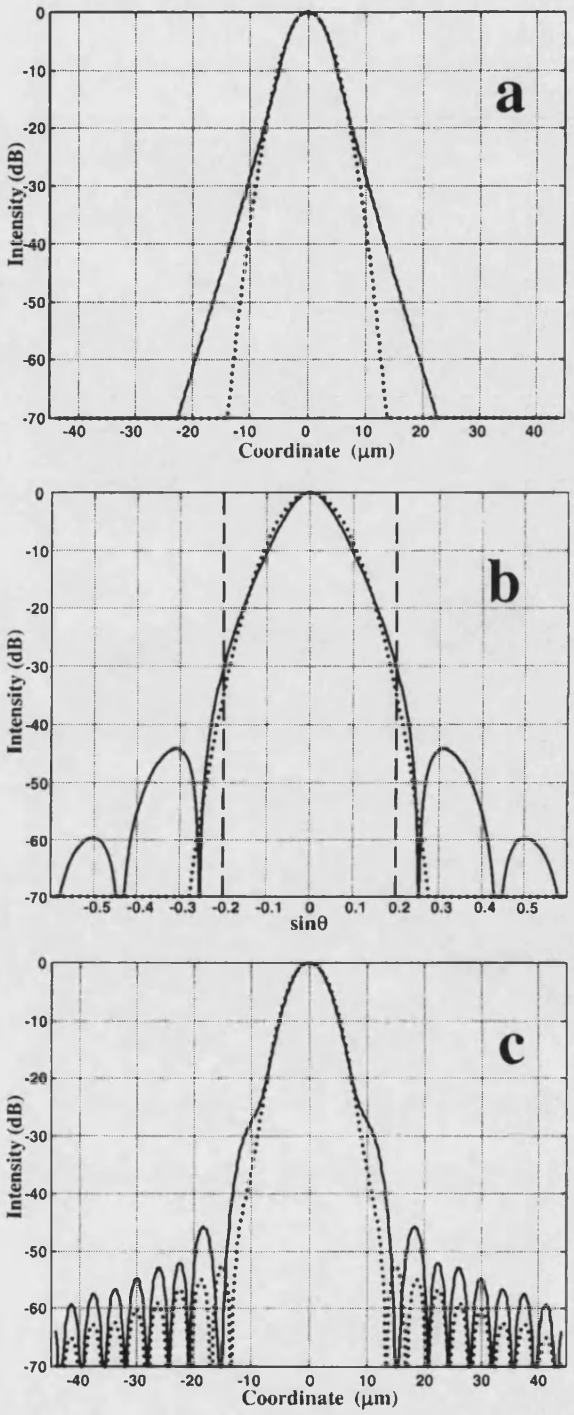

Fig.3.1. **SMF-28 fiber mode (solid curves) and its Gaussian approximation (dotted curves) in a fibre (a), in far field (b), and after one-to-one imaging with NA=0.2 (c)**

Fig.3.1c shows Gaussian and fibre mode distributions after one-to-one imaging through the lens with numerical aperture NA=0.2. This shows some 6 dB underestimation of crosstalk with Gaussian approximation for the fibre separation of 40 μm at the output of the demultiplexer.

Therefore, the Gaussian approximation for the fibre mode should be avoided for the numerical calculation of crosstalk level, and a more accurate mode description should be used. Further in this thesis the fibre mode profile described by Equation (3.2) is used for the calculations of crosstalk and transmission spectra of the demultiplexer and wavelength router.

3.3 Aberrations

The demultiplexer performance is fundamentally limited by aberrations. Firstly, they decrease the coupling efficiency into the output fibres, as considered in the following chapters. In addition, they increase the image tails resulting in higher crosstalk between the adjacent channels, which is analyzed in this section. Let yz be the Cartesian co-ordinate system at the exit pupil and the y -axis lie in the dispersion plane. Consider the wave aberration [10] expansion up to the fourth power

$$W(y,z)=A_{10}y+A_{01}z+A_{20}y^2+A_{11}yz+A_{02}z^2+A_{30}y^3+A_{21}y^2z+A_{12}yz^2+A_{03}z^3+ \quad A_{40}y^4+ \quad A_{31}y^3z+ A_{22}y^2z^2+A_{13}yz^3+A_{40}z^4+... \qquad (3.3)$$

First of all, one can always design the demultiplexer optical scheme symmetric relative to dispersion plane resulting in cancellation of terms with odd powers of z, i.e. $A_{01}=A_{11}=A_{21}=A_{03}=A_{31}=A_{13}=0$. Secondly, A_{10} (image shift in dispersion direction) and A_{20} (meridional defocus, referring to the dispersion plane) can be reduced to zero by proper positioning of output fibres. Thirdly, the remaining aberration terms that depend only on z (namely, the astigmatism $A_{02}z^2$ and sagittal spherical aberration $A_{40}z^4$, referring to the plane

perpendicular to the dispersion direction) can be omitted here because they do not change the image profile in the dispersion direction and, therefore, provide no contribution to crosstalk. However these two aberrations lead to the increase of image spot in the sagittal direction resulting in coupling losses and should be minimized at the design stage (especially the astigmatism). Consider separately the residual terms: meridional coma $A_{30}y^3$, sagittal coma $A_{12}yz^2$, meridional spherical aberration $A_{40}y^4$, and combined spherical aberration $A_{22}y^2z^2$. Assume that these aberrations reach the conventional Rayleigh quarter-wavelength limit at the e^{-2} level of the exit pupil intensity distribution. Applying Fourier analysis to the one-to-one imaging optical system and multiplying the amplitude at the exit pupil by the phase term $\exp[j2\pi W(y,z)/\lambda]$ the amplitude for the image of SMF fibre mode was calculated. The pupil was not truncated, which allows separation of the contributions to the crosstalk caused by aberrations from that caused by diffraction at the aperture edges. Then, the overlap integral [9] between the fibre mode and its image was calculated numerically for different shifts of output fibre in the directions of dispersion. The resultant coupling losses for different types of aberrations are shown in Fig. 3.2 as a function of the

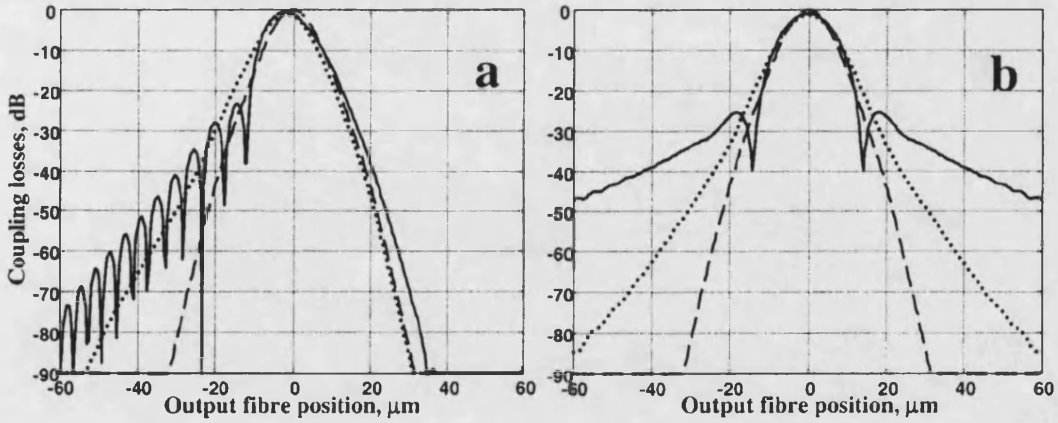

Fig.3.2. **Coupling losses as a function of output fibre position for aberration-free optical system(dashed line) and for the system aberrated with meridional coma (a, solid line), sagittal coma (a, dotted line), meridional spherical aberration (b, solid line), and combined spherical aberration (b, dotted line)**

output fibre position. A typical pitch in the output fibres array for free-space demultiplexer is approximately 30-50 μm [11, 12], and therefore the coupling losses for such displacement of output fibre can be related to crosstalk between adjacent channels. The meridional and sagittal comas result in strongly asymmetric transmission spectra, shown in Fig. 2a, and contribute crosstalk values of -52 and -65 dB, respectively, from one adjacent channel for 40 μm fibre separation. For the meridional and combined spherical aberrations the total crosstalk from two adjacent channels is -36 and -60 dB, correspondingly. Therefore, after correcting the astigmatism for minimization of losses, the elimination of spherical aberration in the dispersion direction is the second concern when designing the optical scheme for demultiplexer. The next aberration to be corrected for better crosstalk performance is meridional coma.

3.4 The influence of aperture size and shape

A significant contribution to crosstalk is also caused by diffraction at the truncating aperture [13] of the device exit pupil. Numerical simulations in this section are not restricted to a specific optical system, it can consist for example of lens and plane grating in a Littrow mount [14] or a single concave grating [15]. In the latter, it is the grating which fully defines the aperture, while in the former the aperture can be defined by both the lens and the grating.

3.4.1 Basic equations

To estimate the crosstalk between channels in a WDM grating demultiplexer, the method of calculating the overlap integral at the exit pupil [16] is used. Let yz be the Cartesian co-

ordinate system at the exit pupil σ and the y-axis lie in the plane of dispersion, then the coupling efficiency η (transmission of the optical system) can be represented as

$$\eta = \left| \iint_{\sigma} E_S E_R^* dydz \right|^2 \qquad (3.4)$$

where E_R is the normalized amplitude of the receiving-fibre mode at the exit pupil and E_S is that of the source-fibre after reverse passing through the optical system. Assume the optical system of unit magnification with equivalent receiving and transmitting single mode fibres, so that $|E_S| = |E_R|$. Neglecting the Fresnel diffraction on the optical surfaces, equation (3.4) yields

$$\eta(\lambda_0) = \left| \iint_{\sigma} I(y,z) \exp\left[\frac{j2\pi}{\lambda_0} W(y,z) \right] dydz \right|^2 \qquad (3.5)$$

where $I(y,z)$ is the normalized intensity distribution of the fibre mode, λ_0 is the wavelength of a channel corresponding to a given receiving fibre at the exit pupil, and $W(y,z)$ is the wave aberration of the optical system. For a WDM system with channel spacing $\delta\lambda$, one can easily calculate the coupling efficiency into this fibre from another channel at a wavelength $\lambda + k\delta\lambda$, where k is an integer. The wavefront at this wavelength will be tilted in the exit pupil relative to the wavefront at λ_0 by an angle

$$\Delta\beta = \frac{mk\,\delta\lambda}{T\cos\beta_0} \qquad (3.6)$$

where m is the operating diffraction order, T is the grating period and β_0 is the diffraction angle at a wavelength λ_0 (in the case of a concave grating with variable spacing, T and β_0 should be related to the grating centre). This corresponds to an "additional wave aberration" $\Delta W = \Delta\beta y$, and therefore the coupling efficiency becomes

$$\eta(\lambda_0 + k\delta\lambda) = \left| \iint_{\sigma} I(y,z) \exp\left[\frac{j2\pi}{\lambda_0} \left(W(y,z) + \frac{mk\delta\lambda\, y}{T\cos\beta_0} \right) \right] dydz \right|^2 \qquad (3.7)$$

Similar to Eq. (3.1), the accumulated crosstalk Q from all the channels in decibels can be expressed as

$$Q = 10\log_{10}\left(\frac{1}{\eta(\lambda_0)} \sum_{k\neq 0} \eta(\lambda_0 + k\delta\lambda) \right) \qquad (3.8)$$

where $\eta(\lambda_0)$ and $\eta(\lambda_0+k\delta\lambda)$ are defined by (3.5) and (3.7), respectively.

3.4.2 Numerical results and discussion

The following parameters have been used in calculations: m=1, $\lambda_0 = 1546.12nm$, $\delta\lambda = 0.4nm$, $T = 2.89\mu m$, $\beta_0 = 12.383^o$. The amplitude of the fibre mode with NA=0.1 at the pupil was calculated using the Fraunhofer approximation. The focal length of 350 mm corresponded to an e^{-2} intensity level at the pupil radius of G = 35 mm. These parameters provide 81 channels in the spectral region 1530-1562 nm with a 50 μm separation between the receiving fibres. The crosstalk calculations have been restricted to the contribution of the six nearest channels (k = ±1, ±2, ±3). To estimate the aperture truncation effects in combination with the aberrations, the optical system was aberrated in the dispersion direction with meridional coma $W=\lambda_0 y^3/(4G^3)$ equal to Rayleigh quarter-wave limit at e^{-2} intensity level (y=G) or meridional spherical aberration $W=\lambda_0 y^4/(8G^4)$ which is a factor of 2 less at the same level.

Consider three types of aperture, when the exit pupil surface σ is truncated (i) by the ordinary square ($-A \le y,z \le A$) [e.g. a conventional square-shaped grating], (ii) the same square, but rotated by an angle of 45° such that the y-axis coincides with its diagonal, designated as "diamond", and (iii) by the circle ($y^2 + z^2 \le R^2$). The values $0.1A/G$ and

$0.1R/G$ correspond to the numerical aperture of optical system. The coupling efficiency $\eta(\lambda_0)$ (termed transmission) and crosstalk for an ideal (W=0) and an aberrated optical system, as a function of the ordinary square size A, are plotted in Figures 3.3 and 3.4, respectively. Transmission of the aberrated optical system relative to that of an ideal one can be considered as a measure of the image quality similar to the Strehl ratio [10]. The crosstalk levels for ideal and aberrated optical systems as a function of the diamond size A and the circle radius R are shown in Figures 3.5 and 3.6, correspondingly.

The diamond provides the best crosstalk performance whilst the ordinary square provides the worst one, which can be easily explained as follows. As a result of diffraction at the square aperture the light intensity at the image plane decreases asymptotically [10] as $1/\rho^2$ in the direction parallel to the square side, and as $1/\rho^4$ in the diagonal direction, where ρ is the distance from the image centre. The diffraction at the circular aperture provides a decrease in intensity as $1/\rho^3$ in any direction. Therefore, for the best crosstalk performance, the grating grooves formed on the square substrate should be directed along the diagonal. High quality performance can be also achieved with a hexagonal aperture if the dispersion plane is parallel to the longer diagonal.

Figs. 3.4 and 3.6 show that enlargement of the ordinary square and circular apertures results in significant crosstalk reduction for both the ideal and aberrated optical systems. However increasing the aperture to about $1.8G$ does not lead to a further reduction in the crosstalk, corresponding to equilibrium in the contributions from truncation and aberrations beyond this point. The enlargement of the diamond aperture (Fig. 3.5) reduces the crosstalk level for an ideal system but does not reduce it for an aberrated one. This is because in this case, the light scattered by the aperture in the dispersion direction has extremely low power and the main contribution to crosstalk is provided by aberrations. The maximum crosstalk

values in the case of circular aperture are 6-8 dB lower compared to those for an ordinary square for

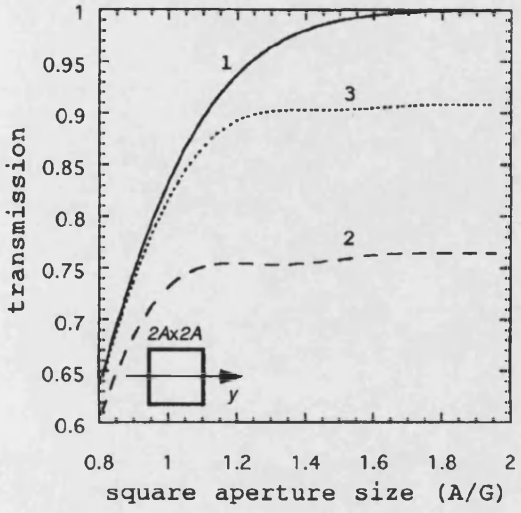

Fig. 3.3. **Transmission of the ideal (1), aberrated with coma (2), and with spherical aberration (3) optical system as a function of the square aperture size**

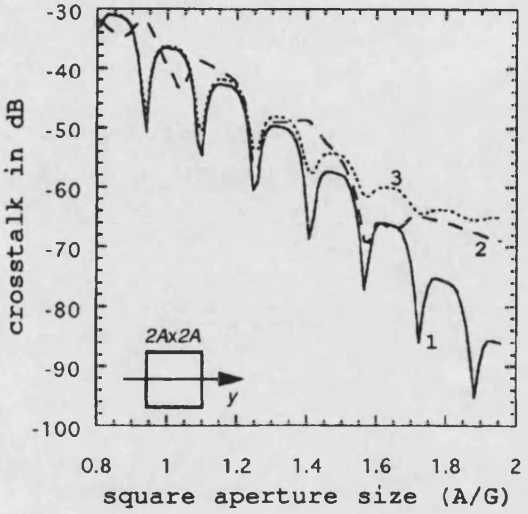

Fig. 3.4. **Crosstalk for the ideal (1), aberrated with coma (2), and with spherical aberration (3) optical system as a function of the square aperture size**

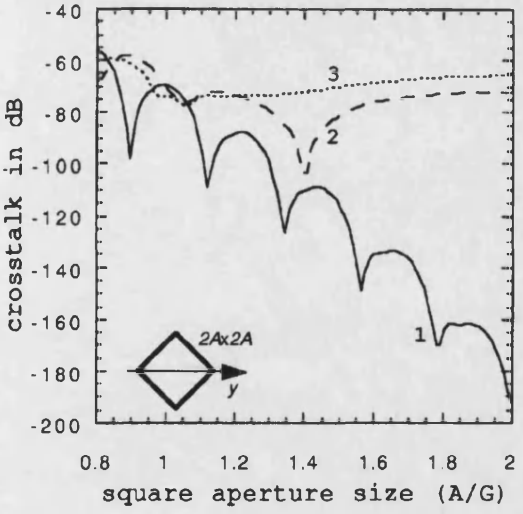

Fig. 3.5. **Same as Fig. 3.4, for an optical system with a diamond aperture**

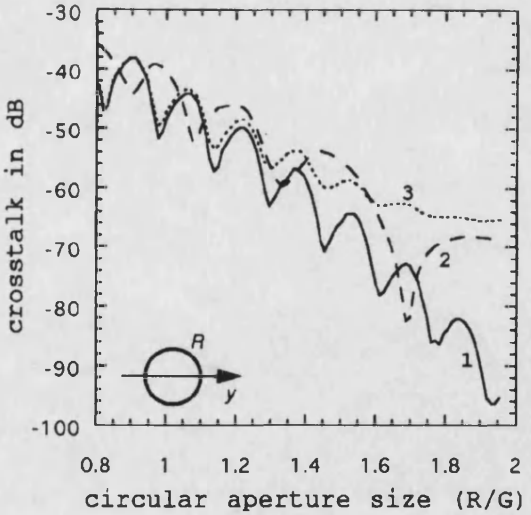

Fig. 3.6. **Same as Fig. 3.4, for an optical system with a circular aperture**

$R=A$ which implies that conventional square grating must be covered by a circular mask for improved crosstalk performance. It should be emphasized once more that the crosstalk is much more dependent on the spherical aberration than on the coma. A spherical aberration, which is half that for coma, provides a much better coupling efficiency (see Fig. 3.3) but results in the same or even higher crosstalk level.

The demultiplexer with the above parameters for both types of aberrations provides crosstalk of better than -60 dB when the circular aperture size $R \geq 1.55G$ and only -40 dB when $R=G$ (see Fig. 3.6). In the case of the diamond -60 dB crosstalk is attainable for the much smaller aperture size $A \geq G$. In fact, this level of crosstalk was shown to be necessary [17] for the design of large NxN network routers (N>170).

The described method can also be applied to calculate crosstalk in a planar waveguide grating demultiplexer [18], which, however, does not allow the aperture shape to be varied.

3.4.3 Experiments

The experiments on aperture truncation effects were carried out in E-Tek Dynamics for an "off-the-shelf" concave holographic grating operating in Littrow mount and aberration-corrected for the wavelength 1542 nm. The main parameters of the grating and optical scheme were as follows: grating diameter 38.5 mm, groove period approximately 2.2 μm, diffraction angle 20.2°, distance from input and output fibres to the grating centre 102 mm, linear dispersion 50 μm/nm, separation between input and output SMF fibres 125 μm. The grating surface was covered by square and circular masks with the dimensions of 23 and 27 mm, corresponding to numerical aperture values NA=0.11 and 0.13, respectively. The light from an unpolarized broadband source was fed to the input fibre. The spectrum of light coupled into the output fibre was displayed on an optical spectrum analyzer. The

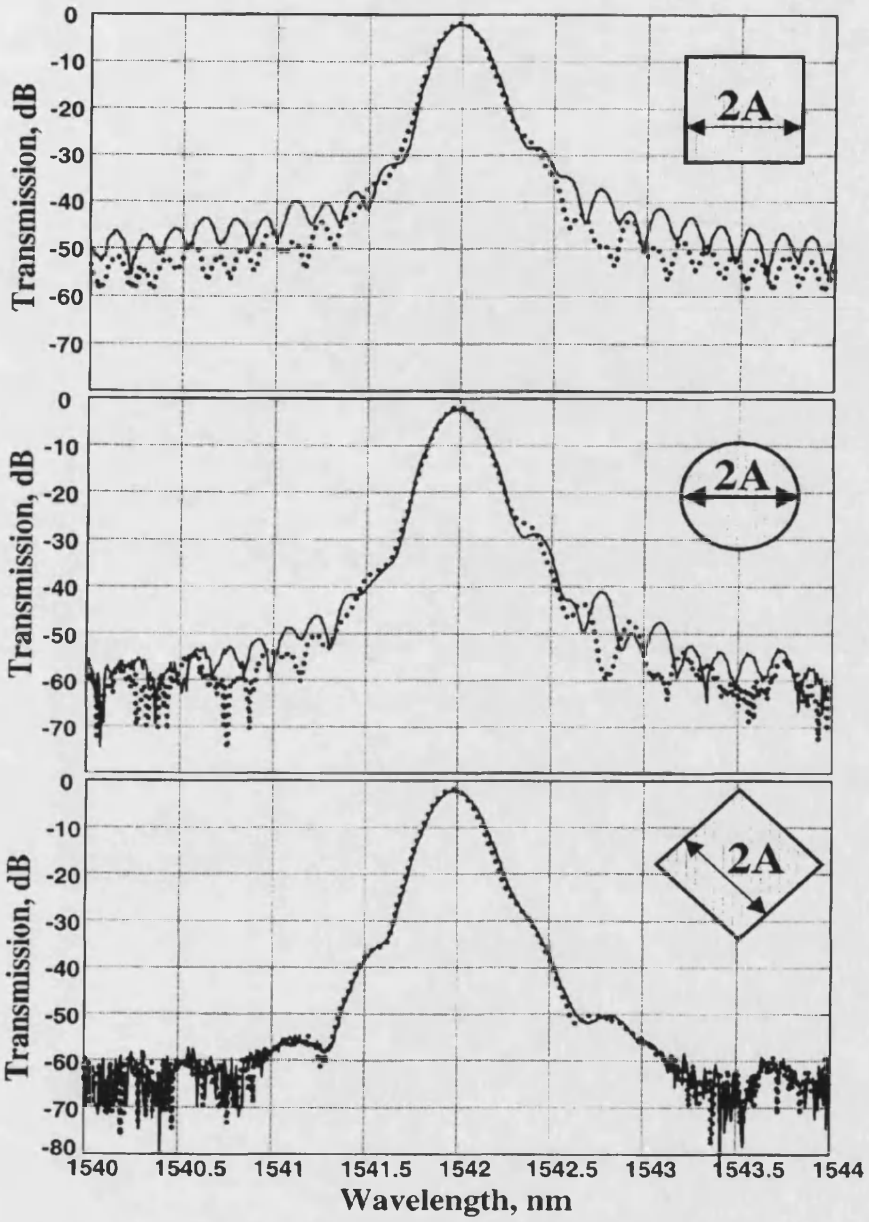

Fig. 3.7. **Experimental passbands for different pupil shape with the size 2A=23 mm(solid line) and 2A=27 mm (dotted line)**

transmission spectra for different aperture size and shape are shown in Fig. 3.7. The coupling losses at the central wavelength due to residual aberrations and grating diffraction efficiency were measured to be approximately 2 dB. The crosstalk reduction with the increase of aperture for the wavelength separation $\delta\lambda$=1 nm from -40 to -45 dB for square

aperture and from -47 to -53 dB for circular aperture are in a good agreement with the numerical simulations. The crosstalk value of -56 dB for both sizes of diamond aperture is caused by the residual aberrations of concave grating. The experiments confirmed the importance of right choice for the size and shape of exit pupil. The level of the -60 dB background for the case of diamond aperture is produced by the scattered light, the causes of which are discussed in the next section.

3.5 Scattered light

An approximately constant background level of crosstalk is caused by the scattered light. This phenomenon is the result of diffraction at random nonuniformities and can be described only statistically [19]. There are two most common categories of scattered light [20]:

(1) Diffuse scattering: light scattered in a wide solid angle at the roughness of holographic grating and optical surfaces as shown in Fig. 3.8a.

(2) In-plane scattering ("grass"): light scattered in the spectral plane (see Fig. 3.8b) due to random variations in the groove spacing or groove depth in ruled grating. The integrated optics devices also scatter the light in the dispersion plane. This type results in a much higher intensity level of the scattered light.

In general, the experimental results [21] show that the intensity of the scattered light from holographic gratings is down by the factor of 5-10 (7-10 dB) in comparison to ruled gratings. Errors arising from the ruling process, which are a manifestation of the fact that ruled gratings have one groove formed after another, are nonexistent in holographic gratings, for which all grooves are formed simultaneously. If properly made, then,

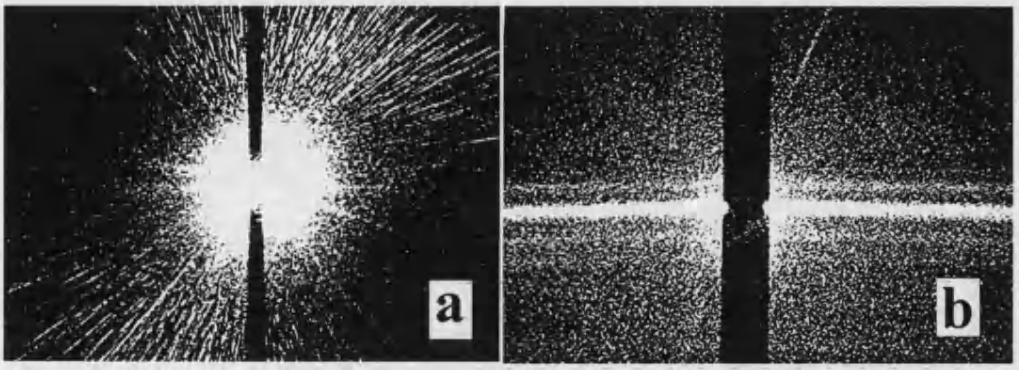

Fig. 3.8. **Stray light from holographic (a) and ruled (b) gratings. The useful light is covered by black strip. After J. F. Verrill, 1978.**

holographic gratings can be entirely free of both small periodic and random groove placement errors found on even the best mechanically ruled gratings.

3.6 Coherent crosstalk and scalability of wavelength routers

As mentioned in Chapter 2, high capacity wavelength routers can considerably simplify large core network architectures [22]. The main problem with these devices is coherent crosstalk due to wavelength re-use within different ports as described in [2-5]. Hill *et al.* [17] demonstrated that free-space optics provides significantly better crosstalk performance than integrated optics devices [5]. In a 32x32 device with a holographic grating they observed an adjacent channel crosstalk of -40 dB and "background" of -60 dB and estimated the acceptable number of ports as 170 with a power penalty of 2.2 dB.

In this section a more accurate approach to the scaling analysis is described. Firstly, we subdivide crosstalk contributions in two parts: (i) Fraunhofer diffraction (FD) at the aperture and (ii) scattered light. Aberrations are assumed to be very small which can be achieved by the proper design. Secondly, it is assumed that the angular dispersion and the

distance between adjacent fibres are fixed, so that router geometrical size increases proportionally to the number of ports, as shown in Fig. 3.9. This implies lower intensity of scattered light on the image plane and cannot be neglected in the scaling analysis.

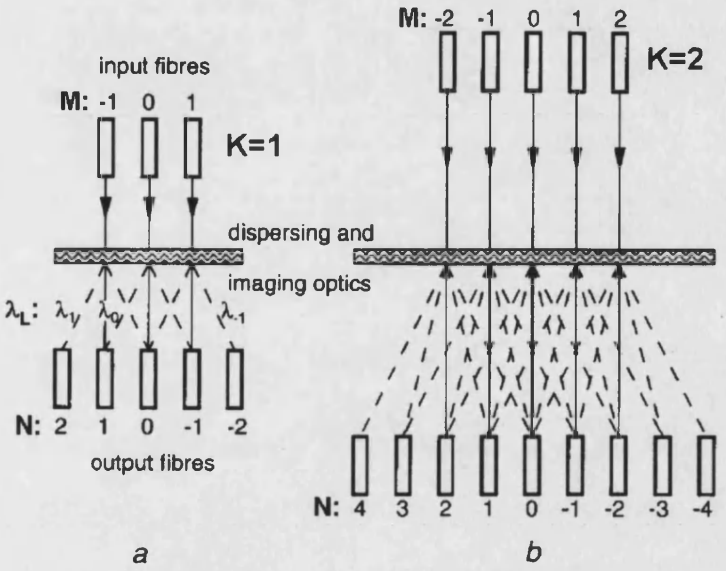

Fig. 3.9. **Schematic diagram of 3x3 (a) and 5x5 (b) wavelength router**

Two types of grating (ruled and holographic) and three aperture shapes (square, circular and diamond) were considered in this thesis to analyze how the increase in the number of ports results in the power penalty for free-space routers. Analysis is carried out for the worst-case operation when all the noise sources have an opposite phase to the signal and match its polarization. The necessity to design networks for the worst-case was highlighted in [3] and [4]. The incoherent crosstalk is not considered because it is completely defined by characteristics of demultiplexer or tunable filter before the receiver.

3.6.1 Scaling concept and basic equations

In the case of coherent crosstalk when the signal power P_s is much larger than that of noise P_n at the same wavelength, the system degradation is caused mainly by the signal oscillations [2] within the bounds $P_s \pm 2\sqrt{P_s P_n}$. The power penalty is defined by the lower bound corresponding to π phase shift between noise and signal. When there are several noise sources with powers P_M at the same wavelength we summarize their amplitudes, and for a fixed decision threshold [2]

$$\text{Penalty} = -10\log_{10}(1 - 2\sum_{M}\sqrt{P_M / P_s}) \ . \qquad (3.9)$$

Consider (2*K*+1)x(2*K*+1) router with a routing formula $N = L - M$, where L is the wavelength number, M is the number of the input fibre ($-K \le L, M \le K$) and N is that of output fibre. Assume that initially a 3x3 router (shown in Fig. 3.9a) is produced, the maximum power exchange between any two adjacent channels due to Fraunhofer diffraction and the diffuse (or in-plane) scattering is, respectively $P_f = \sigma_f P_s$ and $P_d = \sigma_d P_s$. This allows prediction of the power penalty increase when the same technology is applied to fabricate a router scaled up in the number of ports and optical scheme dimensions. By way of an example, consider the performance degradation for the central channel (*L*=*M*=*N*=0) caused by crosstalk from all the signals routed at the central wavelength (shown as solid lines in Fig. 3.9). The noise σ_f is defined by the tails of the fibre mode image whose asymptotic behaviour depends only on aperture shape as described in section 3.3.2. Tail envelopes decay as $1/\rho^2$, $1/\rho^3$, and $1/\rho^4$ for square, circular, and diamond aperture, respectively. Therefore, the upper bound of the Fraunhofer diffraction contribution into the central channel from an input fibre M can be estimated as $P_{fM} = \sigma_f P_s / |M|^{\alpha}$, where α=2,3,4 for square, circular, and diamond aperture,

correspondingly. The intensity of scattered light caused by in-plane scattering (dominant for ruled gratings) is inverse proportional to router size, i.e. to K, whilst in a case of diffuse scattering (holographic grating) it is proportional to $1/K^2$. Thus, the scattering contribution from any input fibre is given by $P_{dM} = \sigma_d P_s / K^{\beta}$, where β=1,2 for a ruled and holographic grating, respectively. Substituting the total noise power $P_M = (\sqrt{P_{fM}} + \sqrt{P_{dM}})^2$ from every input fibre ($M \neq 0$) in (3.9) we obtain for (2K+1)x(2K+1) router

$$\text{Penalty} = -10\log\left(1 - 4\sqrt{\sigma_d K^{2-\beta}} - 4\sum_{M=1}^{K}\sqrt{\sigma_f M^{-\alpha}}\right). \qquad (3.10)$$

3.6.2 Numerical results and discussion

For the calculations based on data from reference [17] we take $\sigma_f = 10^{-4}$, whilst background scattering contribution σ_d should be taken higher than their value of 10^{-6} because the "initial" 3x3 router is 16 times smaller than the 32x32 device . Fig. 3.10

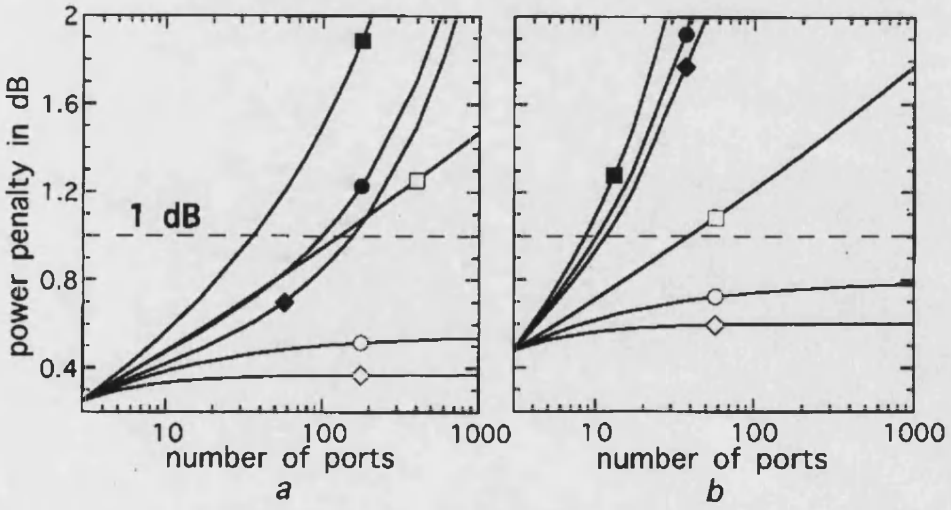

Fig. 3.10. **Power penalty against the number of ports for different routers. Marker shape corresponds to the shape of aperture, black and white markers are related to ruled and holographic gratings, respectively. Initial crosstalk contributions:** σ_f=10^{-4}, σ_d=1.6x10^{-5} **(a), and** σ_f=10^{-4}, σ_d=2.56x10^{-4} **(b).**

shows the power penalty as a function of the number of ports for different router types and "initial" crosstalk contributions. It can be seen that routers with circular or diamond aperture based on holographic grating are absolutely scalable, i.e. the power penalty converges to the limit for a very large number of ports. Thus holographic gratings are preferable from the scalability point of view. The scaling degradation for integrated optics devices is similar to the case of square aperture and ruled grating and can be estimated from (3.10) for $\alpha=2$, $\beta=1$.

3.7. Conclusions

This chapter studied the main origins of crosstalk in free-space WDM demultiplexers and wavelength routers. The necessity to use exact fibre mode solution for crosstalk calculations instead of its Gaussian approximation, which leads to an approximately 6 dB underestimation, was suggested and verified.

Analysis of aberrations demonstrated that crosstalk is most sensitive to the spherical aberration in dispersion direction. The next aberration to be corrected for better crosstalk performance in WDM devices is meridional coma.

A simple method was proposed for calculation of crosstalk in WDM grating demultiplexers, and three types of aperture shape were investigated for ideal and aberrated optical systems. It was shown that the best performance is provided by diamond aperture. To improve the crosstalk performance, a circular aperture should be used to mask the square and rectangular gratings. The aperture enlargement leads to a reduction in crosstalk until the contribution of edge-scattered light exceeds that due to aberrations. A moderately (within Rayleigh criterion) aberrated optical system with a correctly chosen aperture size and/or shape can provide crosstalk figures of better than -50 dB. The experimental results

on aperture effects are in good agreement with numerical simulations and demonstrate -60 dB background level of crosstalk for a holographic concave grating.

Contribution to the coherent crosstalk in wavelength routers from the Fraunhofer diffraction at the aperture and diffuse or in-plane scattering was analyzed. A simple formula estimating the power penalty due to simultaneous scaling up the number of ports and geometrical sizes of wavelength routers was derived. The router scalability is strongly dependent on the aperture shape and the type of grating used as dispersive element. It was shown that holographic grating-based routers with circular and diamond aperture are absolutely scalable from the crosstalk point of view and, hence, have the greatest potential for applications in densely spaced WDM networks.

References to Chapter 3

[1] M. K. Smit, and C. van Dam, "PHASAR-based WDM-devices: principles, design and applications," *IEEE J. Select. Topics Quantum Electronics*, vol.2, 1996, pp.236-250.

[2] Goldstein, E.L., Eskildsen, L., and Elrefaie, A.F.: "Performance Implications of Component Crosstalk in Transparent Lightwave Networks", *IEEE Photon. Technol. Lett.*, vol.6, 1994, pp.657-660.

[3] Goldstein, E.L., Eskildsen, L., Lin, C., and Silberberg, Y.: "Polarization Statistics of Crosstalk-Induced Noise in Transparent Lightwave Networks", *IEEE Photon. Technol. Lett.*, vol.7, 1995, pp.1345-1347.

[4] Jin, Y., and Kavehrad, M.: "An Optical Cross-Connect System as a High-Speed Switching Core and Its Performance Analysis", *J. Lightwave Technol.*, vol.14, 1996, pp.1183-1197.

[5] Takahashi, H., Oda, K., and Toba, H.: "Impact of Crosstalk in an Arrayed-Waveguide Multiplexer on NxN Optical Interconnection", *J. Lightwave Technol.*, vol.14, 1996, pp.1097-1105.

[6] E.G. Churin, P. Bayvel, J.E. Midwinter, and A.M. Hill, "The influence of aperture size and shape on crosstalk level in free-space grating demultiplexers for WDM networks", *IEEE Photon. Technol. Lett.*, vol.8, 1996, pp.1337-1339.

[7] E. G. Churin, P. Bayvel, "Coherent crosstalk and scalability of free-space wavelength routers", *IEE Electronics Letters*, vol.34, 1998, pp.1225-1227.

[8] D. Marcuse, "Loss analysis of single-mode fiber splices", *Bell System Technical Journal*, vol.56, 1977, pp.703-718.

[9] A. W. Snyder, and J. D. Love, *Optical waveguide theory.* London: Chapman and Hall, 1983.

[10] Born, M. and Wolf, E, *Principles of Optics.* Pergamon Press, London, 1970.

[11] J. P. Laude, "New athermal very dense wavelength division multiplexers", *Proc. ECOC 2000*, vol.3, pp.181-182.

[12] P. Martin, E. Taufflieb, B. Laloux, and H.C. Lefevre, "Optimized bulk-optic grating approach for D-WDW demultiplexers", *Proc. ECOC 1999*, vol.2, pp.110-111.

[13] M. C. Hutley, "The use of apodization to reduce stray light from diffraction gratings," *Opt. Commun.*, vol.40, 1982, pp.317-321.

[14] Koh-ichi Aoyama, and Jun-ichiro Minowa, "Low-loss optical demultiplexer for WDM systems in the 0.8 μm wavelength region," *Applied Optics*, vol.18, 1979, pp. 2834-2836.

[15] F. N. Timofeev, J. E. Midwinter, P. Bayvel, E. G. Churin, A. Stavdas, and M. N. Sokolskii, "Free-space aberration-corrected grating demultiplexer for application in

densely-spaced, subnanometre wavelength-routed optical networks," *IEE Electronics Letters*, vol.31, 1995, pp. 1368-1370.

[16] R. E. Wagner, and W. J. Tomlinson, "Coupling efficiency of optics in single-mode fibre components," *Applied Optics*, vol.21, 1982, pp. 2671-2688.

[17] Hill, A.M., Carter, S., Armitage, J., Shabeer, M., Harmon, R.A., and Rose, P.: "A Scaleable and Switchless Optical Network Structure, Employing a Single 32x32 Free-Space Grating Multiplexer", *IEEE Photon. Technol. Lett.*, vol.8, 1996, pp.569-571.

[18] K. R. Poguntke, J. B. D. Soole, H. P. LeBlanc, N. C. Andreadakis, P. Grabbe, R. Bhat, C. Caneau, and M. A. Koza, "High-performance InP reflecting-grating wavelength multiplexer," *IEE Electronics Letters*, vol.30, 1994, pp. 512-513.

[19] J.M. Lerner, J. Flamand, and A. Thevenon. *Proc. SPIE*, vol.503, 1984, pp.53-55.

[20] M.C. Hutley. *Diffraction Gratings*. Academic Press, London, 1982.

[21] J. F. Verrill, "The specification and measurement of scattered light from diffraction gratings," *Optica Acta*, vol.25, 1978, pp.531-547.

[22] Hawker, I., Tandon, V., Cotter, D., and Hill, A.: "Ultra-high-capacity wavelength-routed networks", *British Telecomms. Eng.*, vol.13, 1994, pp.103-111.

Chapter 4

Stationary anastigmatic mounts of concave grating

4.1 Introduction

As already mentioned in Chapter 2, the most important step in the design of concave grating multi/demultiplexers is the choice of a mount defining the positions of the input and output fibres relative to the grating centre. This allows the minimization of aberrations, and, therefore, the insertion losses within the operating spectral range. Theoretically, a grating can perform aberration-free imaging from any input to any output point at predetermined wavelength. However, other wavelengths within the operating range will be focused with aberrations. The largest chromatic aberration associated with concave gratings is astigmatism [1], when the meridional and sagittal rays at the same wavelength are focused at different points. In conventional spectrographs a moderate amount of astigmatism is admissible since it does not affect the resolution when the detectors' line coincides with the meridional focal curve. However, the reduction of astigmatism increases the useful output light intensity and, therefore, the signal-to-noise ratio. There is extensive literature on finding anastigmatic mountings (see the bibliography in Ref.[2]) using analytical techniques. The term anastigmatic is generally used to describe imaging with no astigmatism, although other aberrations can be present, whereas imaging with no

aberrations is described as stigmatic. Cordelle *et al* [3] described mounts of holographic concave gratings with three stigmatic points where the meridional and sagittal focal curves cross each other. This allows reduction of astigmatism over a relatively wide spectral region compared to the case when the focal curves intersect one or two times.

For the narrow band ($\Delta\lambda/\lambda_0<<1$) spectrographs [4], as is the case with demultiplexers and wavelength routers, it is sufficient to find the concave grating mounts which provide stationary astigmatism close to the central wavelength λ_0 when the meridional and sagittal focal curves are tangential to each other. Demultiplexers and routers, in contrast to spectrographs, must provide diffraction limited imaging of multi-wavelength point source, which is necessary for high coupling and imposes strict requirements on residual astigmatism.

In this chapter "ideal" spherical concave gratings forming a stigmatic image at a chosen wavelength are considered. General equations for their mounts, which provide stationary and superstationary astigmatism close to this wavelength, are derived [7]. The concept of an "ideal" grating simplifies the understanding and allows the separation of chromatic aberrations specific to a given mount from those introduced in the process of ruling or holographic recording. The problem of approximating the design of a holographic or ruled grating to that of an "ideal" one should be solved separately for every particular design.

Some novel and previously described special cases of stationary anastigmatic mounts are presented. Throughout this analysis, the usual root-mean-square (RMS) wave aberration is used as a measure of the performance quality.

An additional modification of stationary anastigmatic spectrograph into a novel retroreflective scheme by introducing a convex mirror concentric to the intermediate image is described [8]. This leads to a doubling of the dispersion, significant increase of the sagittal image field and substantial further compensation of the chromatic astigmatism.

4.2 The grating function and focal curves

Refer to Fig. 4.1 to define a Cartesian co-ordinate system $Oxyz$, whose origin O is at the grating centre, x axis is the normal to the grating surface, and xy is the dispersion plane. The grating spherical surface of radius R is described by equation

$$x(y,z) = R - \sqrt{R^2 - y^2 - z^2}\,. \qquad (4.1)$$

Following Peisakhson [9] consider the grating function $m(y,z)$ whose integer values define the positions of the grooves.

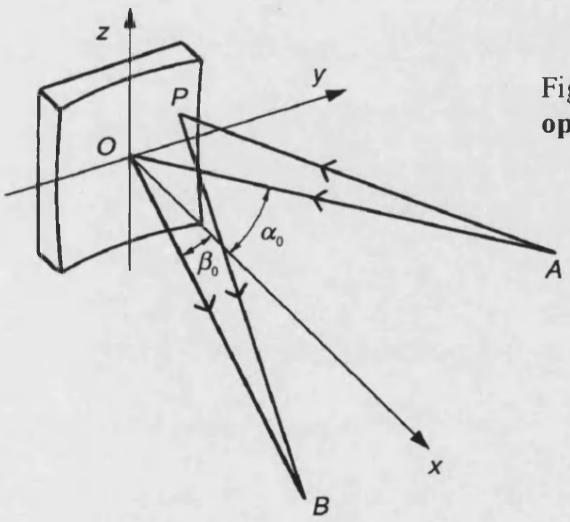

Fig.4.1. **Schematic diagram of the optical scheme.**

Assume that a light ray at the wavelength λ_0 (the central wavelength within our operating spectral range) radiated from a point source A $(x = r_{\alpha 0}\cos\alpha_0,\ y = r_{\alpha 0}\sin\alpha_0,\ z = 0)$ and diffracted in the k-th order at the arbitrary point $P(y,z)$ of the grating reaches the point B $(x = r_{\beta 0}\cos\beta_0,\ y = r_{\beta 0}\sin\beta_0,\ z = 0)$. Then the light path function [10] can be represented by

$$F(y,z) = < AP > + < PB > - k\lambda_0 m(y,z) \qquad (4.2)$$

where,

$$< AP >= \sqrt{(r_{\alpha 0}\cos\alpha_0 - x(y,z))^2 + (r_{\alpha 0}\sin\alpha_0 - y)^2 + z^2} \quad ,$$

$$< PB >= \sqrt{(r_{\beta 0}\cos\beta_0 - x(y,z))^2 + (r_{\beta 0}\sin\beta_0 - y)^2 + z^2} \quad ,$$

and $x(y,z)$ is defined by Eq. (4.1). $F(y,z)$=const corresponds to an aberration-free image at the point B. Therefore the function $m(y,z)$ of an ideal grating can be expressed as

$$m(y,z \mid \lambda_0,\alpha_0,\beta_0,r_{\alpha 0},r_{\beta 0}) = \frac{1}{k\lambda_0}[< AP > + < PB > -(r_{\alpha 0} + r_{\beta 0})] \quad ,(4.3)$$

where the co-ordinates y,z on the grating surface are separated by a line from the optical scheme parameters. The constant term $(r_{\alpha 0} + r_{\beta 0})$ is introduced to define, for convenience, $m(0,0) = 0$.

Expanding m into a power series up to the second order yields [9]

$$m(y,z) = M_{10}y + M_{20}y^2 + M_{02}z^2 \quad , \qquad (4.4)$$

where

$$M_{10} = -\frac{1}{k\lambda_0}(\sin\alpha_0 + \sin\beta_0) \qquad (4.5)$$

defines the angular dispersion,

$$M_{20} = \frac{1}{2k\lambda_0}\left(\frac{\cos^2\alpha_0}{r_{\alpha 0}} + \frac{\cos^2\beta_0}{r_{\beta 0}} - \frac{\cos\alpha_0 + \cos\beta_0}{R}\right) \qquad (4.6)$$

defines the grating power for the meridional rays ($z = 0$), and

$$M_{02} = \frac{1}{2k\lambda_0}\left(\frac{1}{r_{\alpha 0}} + \frac{1}{r_{\beta 0}} - \frac{\cos\alpha_0 + \cos\beta_0}{R}\right) \qquad (4.7)$$

defines the same for the sagittal rays ($y = 0$ on the grating surface).

Using these expansion coefficients one can define, in paraxial approximation, the positions of the meridional (β, $r_{\beta M}$) and sagittal (β, $r_{\beta S}$) foci for the same point source A at an arbitrary wavelength λ. After substituting $\lambda_0 \to \lambda$, $\beta_0 \to \beta$, in Eqs. (4.5-

4.7), $r_{\beta 0} \rightarrow r_{\beta M}$ in Eq.(4.6), $r_{\beta 0} \rightarrow r_{\beta S}$ in Eq.(4.7) and equating the resultant and initial expressions one obtains

$$\beta(\lambda) = \arcsin[\frac{\lambda}{\lambda_0}(\sin\alpha_0 + \sin\beta_0) - \sin\alpha_0] \tag{4.8}$$

$$r_{\beta M}(\lambda) = \cos^2\beta(\lambda)\left[\frac{\lambda}{\lambda_0}\left(\frac{\cos^2\alpha_0}{r_{\alpha 0}} + \frac{\cos^2\beta_0}{r_{\beta 0}} - \frac{\cos\alpha_0 + \cos\beta_0}{R}\right) - \frac{\cos^2\alpha_0}{r_{\alpha 0}} + \frac{\cos\alpha_0 + \cos\beta(\lambda)}{R}\right]^{-1} \tag{4.9}$$

$$r_{\beta S}(\lambda) = \left[\frac{\lambda}{\lambda_0}\left(\frac{1}{r_{\alpha 0}} + \frac{1}{r_{\beta 0}} - \frac{\cos\alpha_0 + \cos\beta_0}{R}\right) - \frac{1}{r_{\alpha 0}} + \frac{\cos\alpha_0 + \cos\beta(\lambda)}{R}\right]^{-1}. \tag{4.10}$$

These are the parametric equations for the meridional and sagittal focal curves in polar co-ordinates, which allow expression of the aberrations directly as a function of λ, although in the literature on concave gratings [2] these focal curves are usually given as functions of the angle β.

4.3 Wave aberration

The performance of stationary anastigmatic mounts described below is estimated by means of the wave aberration $W(y,z)$ defined as the deviation of the real wave front from a reference sphere centred on the predetermined image position [11], and expressed as a function of the grating surface co-ordinates y,z . The most appropriate characteristic to describe the image quality is the RMS wave aberration denoted as $\overline{W}$ and defined as

$$\overline{W}^2 = \frac{1}{\sigma}\iint_S W^2(y,z)dydz - \left[\frac{1}{\sigma}\iint_S W(y,z)dydz\right]^2 , \tag{4.11}$$

where S and σ are the grating surface and its area respectively. According to Marechal criterion an optical system is well corrected for $\overline{W} \leq \lambda/14$.

As was shown above, the function $m(y,z)$ of an ideal grating forming an aberration free image is determined by the wavelength λ_0 and the optical scheme geometry. The deviation $\Delta m(y,z)$ from the ideal grating function introduces additional phase delay of $2\pi k\Delta m$ to the diffracted beam corresponding to the wave aberration

$$W = k\lambda\Delta m \quad . \qquad (4.12)$$

At the wavelength $\lambda \neq \lambda_0$ the wave aberration on the meridional focal curve may be represented as

$$W(y,z) = k\lambda[m(y,z \mid \lambda_0,\alpha_0,\beta_0,r_{\alpha 0},r_{\beta 0}) - m(y,z \mid \lambda,\alpha_0,\beta(\lambda),r_{\alpha 0},r_{\beta M}(\lambda))] \ , \quad (4.13)$$

where $\beta(\lambda)$, $r_{\beta M}(\lambda)$ are defined by Eqs.(4.8, 4.9) and m is from Eq.(4.3). Now the second term in brackets corresponds to an ideal grating and the first to an aberrated one, when illuminated at $\lambda \neq \lambda_0$.

Real gratings produced by ruling [12] or holographic recording [2], in addition to the described chromatic aberrations, introduce aberrations caused by fundamental limitations, inherent in the fabrication process. These are not considered in this chapter.

4.4 Stationary astigmatism

The astigmatism is caused by the difference $\Delta r_\beta = r_{\beta M} - r_{\beta S}$ in the positions of the meridional and sagittal foci when $\lambda \neq \lambda_0$, therefore it becomes stationary if the sagittal and meridional focal curves are tangential for $\lambda = \lambda_0$, i.e.

$$\frac{\partial(r_{\beta M} - r_{\beta S})}{\partial\lambda} = 0 \qquad (4.14)$$

Substituting Eqs.(4.8-4.10) in (4.14) and differentiating gives the condition for the stationary anastigmatic mounts

$$\frac{1}{r_{\beta 0}} = \frac{\sin\alpha_0 - \sin\beta_0}{2r_{\alpha 0}\sin\beta_0} + \frac{\sin\beta_0[1+\cos(\beta_0-\alpha_0)]}{2R\,q_0\cos\beta_0} \quad . \quad (4.15)$$

where

$$q_0 = \sin\alpha_0 + \sin\beta_0 \quad . \tag{4.16}$$

4.5 Superstationary astigmatism

For the superstationary astigmatism, in addition to Eq.(4.14) one should require that when $\lambda = \lambda_0$

$$\frac{\partial^2 (r_{\beta M} - r_{\beta S})}{\partial \lambda^2} = 0 \tag{4.17}$$

Substituting Eqs.(4.8-4.10) in Eq.(4.17) and combining the result with Eq.(4.15) yields the simultaneous equations, which determine the superstationary anastigmatic mounts

$$\begin{cases} \dfrac{1}{r_{\alpha 0}} = \dfrac{\sin\beta_0\{q_0^2 + \cos^2\beta_0[q_0^2 - \sin^2(\beta_0 - \alpha_0) + q_0\cos\beta_0\sin(\beta_0 - \alpha_0)]\}}{R\,q_0^3\cos^3\beta_0} & (4.18) \\ \dfrac{1}{r_{\beta 0}} = \dfrac{\sin\beta_0\{4\sin^2\alpha_0\cos^2\beta_0[1 + \cos(\beta_0 - \alpha_0)] + q_0^2\sin\beta_0(\sin\alpha_0 - \sin\beta_0)\}}{2R\,q_0^3\cos^3\beta_0} & (4.19) \end{cases}$$

In these mounts sagittal and meridional focal curves have a second-order osculation point. This means that chromatic astigmatism grows only as $(\lambda - \lambda_0)^3$. In addition to the very low astigmatism, the remarkable feature of the superstationary anastigmatic mounts lies in the nearly flat image field. This is because both focal curves have the same curvature at the point where they are cross-tangential and that the sagittal curvature is generally very small.

4.6 Special cases and mounts

All the mounts described below are associated with the design of multi/demultiplexers with single mode fibre inputs/outputs for WDM optical communication systems. The RMS wave aberration is calculated on the meridional focal curve in the spectral range 1500-1600

nm for the gratings forming aberration-free image at the wavelength λ_0=1550 nm. The grating radius of curvature is R=270 mm and diameter D=60 mm is defined by the single mode fibre numerical aperture NA=0.11 when $r_{\alpha 0}$, $r_{\beta 0}$ are close to R. In the mount diagrams the meridional M and sagittal S focal curves are shown by solid lines, x-axis, Rowland circle and the straight line x=R by dotted lines, respectively.

4.6.1 Rowland circle

This is a widely used mount [2] with zero meridional grating power ($M_{20} = 0$) and positive sagittal power ($M_{02} > 0$) when the source and image positions are defined by

$$r_{\alpha 0} = R\cos\alpha_0 \ , \ r_{\beta 0} = R\cos\beta_0 \quad . \qquad (4.20)$$

Substituting these expressions into Eq.(4.15) provides

$$\frac{\sin\alpha_0(2-\sin^2\beta_0)+\sin\beta_0}{\cos^3\beta_0} - \frac{\sin^2\alpha_0}{\sin\beta_0\cos\alpha_0} = 0 \qquad (4.21)$$

A similar equation for holographic gratings was found by Grange [13] when optimising the recording scheme parameters. After additional analysis [14] it was found that this equation has only two real roots:

$$\sin\alpha_0 = \sin\beta_0 \frac{\cos^2\beta_0 \pm \sqrt{1+\cos^2\beta_0}}{1+\sin^2\beta_0\ \cos^2\beta_0}, \qquad (4.22)$$

with the positive value of the square root corresponding to the higher dispersion, when the source and image lie on the same side of the x-axis. The diagram of solutions $\beta_0(\alpha_0)$ is shown in Fig. 4.2.

Superstationary astigmatism cannot be realised on the Rowland circle because the simultaneous equations (4.18, 4.19) have no solutions under the conditions (4.20).

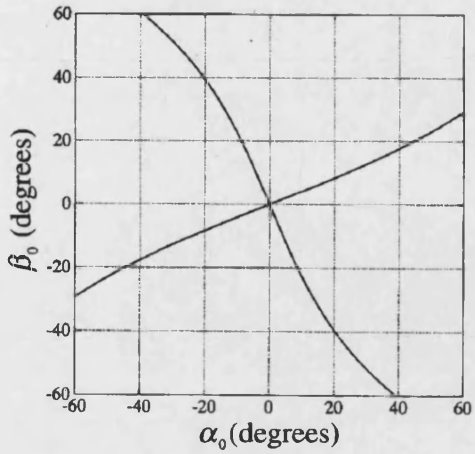

Fig.4.2.**The diagram of solutions $\beta_0(\alpha_0)$ providing stationary astigmatism on the Rowland circle.**

4.6.2 Sagittal straight line

This is another commonly used mount [15] with zero sagittal grating power ($M_{02} = 0$) and negative meridional power ($M_{20} < 0$) corresponding to straight grooves, suitable for mechanical ruling. The source and image lie on the straight line $x=R$ tangential to the Rowland circle in the centre of grating curvature and their positions are defined by

$$r_{\alpha 0} = R / \cos\alpha_0 \ , \ r_{\beta 0} = R / \cos\beta_0 \quad . \qquad (4.23)$$

Sakayanagi [16] described two stationary anastigmatic solutions for this mount

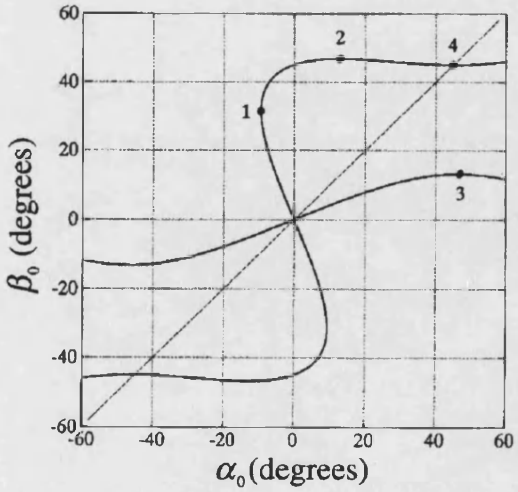

Fig.4.3.**The diagram of solutions $\beta_0(\alpha_0)$ for stationary astigmatism on the straight line $x=R$**

($\alpha_0 = 0$, $\beta_0 = 45°$ and $\alpha_0 = \beta_0 = 45°$). Substituting Eq.(4.23) into Eq.(4.15) yields

$$\frac{\sin\beta_0[1+\cos(\beta_0-\alpha_0)]}{q_0\cos\beta_0} - \frac{q_0\cos\alpha_0+\sin(2\beta_0)-\sin(2\alpha_0)}{\sin\beta_0} = 0 \qquad (4.24)$$

The diagram of solutions $\beta_0(\alpha_0)$ calculated numerically shown in Fig. 4.3 which is more complex than that for the Rowland circle mount and provides some interesting instructive cases. Point 1 ($\alpha_0 = -9.447°, \beta_0 = 31.399°, \partial\beta_0/\partial\alpha_0 = \infty$) satisfies Eqs.(4.18, 4.19) and corresponds to the superstationary astigmatism. This mount and its RMS wave aberration curve $\overline{W}(\lambda)/\lambda$ are shown in Fig. 4.4a and b, respectively. The dashed line $\beta_0 = \alpha_0$ helps

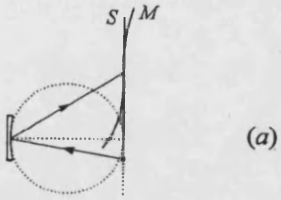

(a)

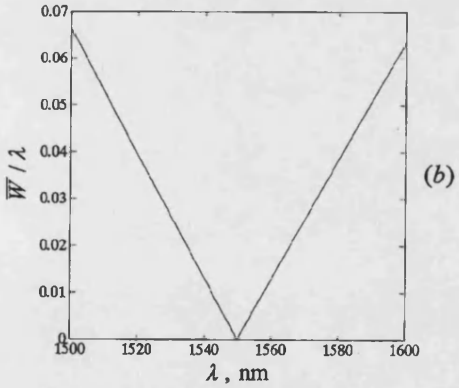

(b)

Fig. 4.4. **(a) Superstationary anastigmatic mount on the sagittal straight line** (α_0=-9.447°, β_0=31.399°) **and (b) its RMS wave aberration as**

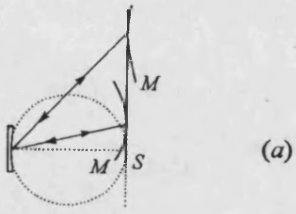

(a)

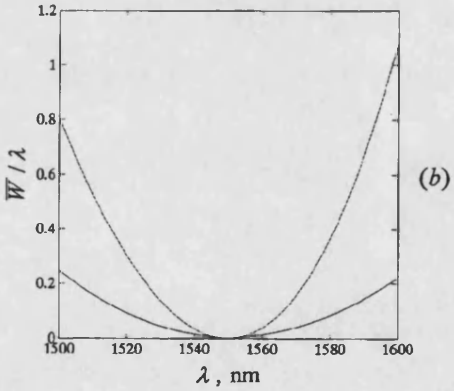

(b)

Fig. 4.5. **(a) The mount on the sagittal straight line stationary anastigmatic in both directions** (α_0=46.77866°, β_0=13.22135°) **and (b) its RMS wave aberration for through (solid line) and inverse (dashed line) optical schemes.**

to find the stationary anastigmatic Littrow mount of Sakayanagi (point 4, $\alpha_0 = \beta_0 = 45°$), which will be described below, in section 4.6.4. Points 2 and 3 belonging to the different solution branches are symmetric relative to the line $\beta_0 = \alpha_0$, so these mounts are the inverse of each other. Therefore, the optical scheme ($\alpha_0 = 46.77866°$, $\beta_0 = 13.22135°$) is stationary anastigmatic in both directions (see Fig. 4.5), which can be useful in WDM devices.

4.6.3 Normal imaging

For brevity we designate in this way the family of mounts in which a ray diffracted at the grating vertex is normal to the meridional and sagittal focal curves for $\lambda = \lambda_0$. This provides close to normal incidence onto the image surface within the operating spectral range and, therefore, significantly simplifies the positioning of optical fibres at the output of the demultiplexer.

To ensure the condition of normal imaging, $r_{\beta M}(\lambda)$ and $r_{\beta S}(\lambda)$ should be extrema at $\lambda = \lambda_0$, i.e. $\partial r_{\beta M} / \partial \lambda = \partial r_{\beta S} / \partial \lambda = 0$. Substituting (4.8) into (4.9) and differentiating the result give the condition for normal imaging on the meridional focal curve as

$$\frac{\cos^2 \alpha_0}{r_{\alpha 0}} = \frac{1 + \cos(\beta_0 - \alpha_0)}{R \cdot \cos \beta_0} - \frac{\cos^2 \beta_0 + 2 q_0 \sin \beta_0}{r_{\beta 0}} \qquad (4.25)$$

For the case of stationary astigmatism, the sagittal focal curve is perpendicular to the above-mentioned ray as well, because it is tangential to the meridional one at this point. Using Eqs.(4.15, 4.25) one can express $r_{\alpha 0}$ and $r_{\beta 0}$ as functions of α_0 and β_0 for the case of stationary astigmatism with normal imaging

$$\begin{cases} \dfrac{1}{r_{\alpha 0}} = \dfrac{\sin\beta_0\,(q_0+\sin\alpha_0)[1+\cos(\beta_0-\alpha_0)]}{R\,q_0^2\cos\beta_0} & (4.26) \\ \dfrac{1}{r_{\beta 0}} = \dfrac{\sin^2\alpha_0\,[1+\cos(\beta_0-\alpha_0)]}{R\,q_0^2\cos\beta_0} & (4.27) \end{cases}$$

For the cases of the Rowland circle and sagittal straight line mounts the pair of simultaneous equations (4.26, 4.27) has only a trivial solution $\alpha_0=\beta_0=0$ which corresponds to zero dispersion, this implies that the conditions of stationary astigmatism and normal imaging are incompatible for these mounts.

For comparison consider three different stationary anastigmatic mounts having the same value of $q_0 = 0.5$, which corresponds to the grating period T=$2\lambda_0$ at the vertex O (see Fig. 4.1). These are (i) the normal imaging mount ($\alpha_0 = 20.70481°$, $\beta_0 = 8.421058°$, $r_{\alpha 0} = r_{\beta 0} = 1.000673R$), the mount (ii) on the Rowland circle ($\alpha_0 = 20.48454°$, $\beta_0 = 8.62930°$), and (iii) on the sagittal straight line ($\alpha_0 = 20.95274°$, $\beta_0 = 8.186875°$) whose configurations and the corresponding RMS wave aberrations are shown in Figs. 4.6, 4.7, and 4.8, respectively. The source and image in all three mounts lie on the same side of the x axis which provides sufficiently large dispersion for relatively small angles and close values of $r_{\alpha 0}$ and $r_{\beta 0}$. These correspond to close numerical apertures of the source and its image and, therefore, to high coupling efficiency [17] in WDM systems. Experimental results and analysis of similar mounts using holographic [18, 19] and ruled [20] gratings with single mode optical fibre inputs/outputs have been reported. To determine the mount parameters for the superstationary anastigmatic normal imaging Eqs.(4.18, 4.19, and 4.25) should be solved simultaneously. One possible solution ($\alpha_0 = -18.37351°$, $\beta_0 = 49.55110°$, $r_{\alpha 0} = r_{\beta 0} = 0.943098R$) is shown in Fig.4.9.

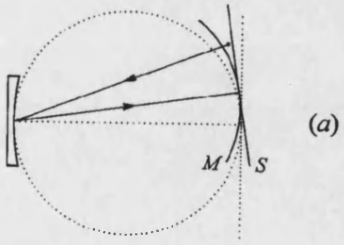

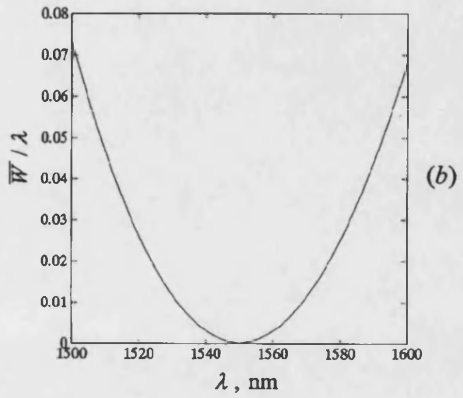

Fig.4.6. **(a) Stationary anastigmatic mount with normal imaging** (α_0=20.70481°, β_0=8.421058°, $r_{\alpha 0}$= $r_{\beta 0}$=1.000673R) **and its RMS wave aberration (b).**

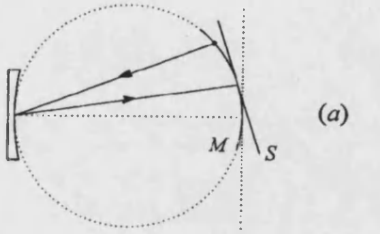

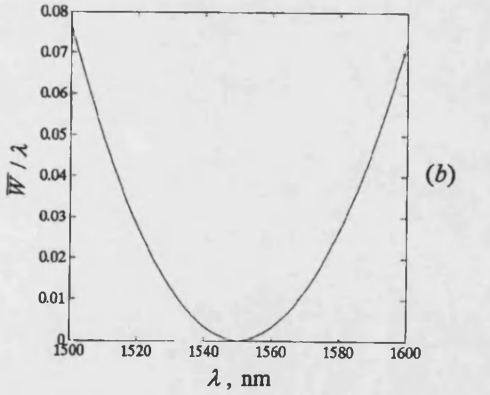

Fig. 4.7. **(a) Stationary anastigmatic mount on the Rowland circle** (α_0=20.48454°, β_0=8.62930°) **and its RMS wave aberration (b).**

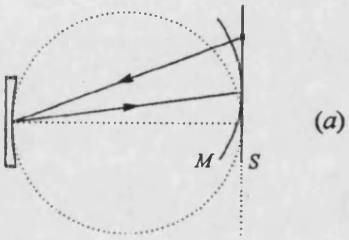

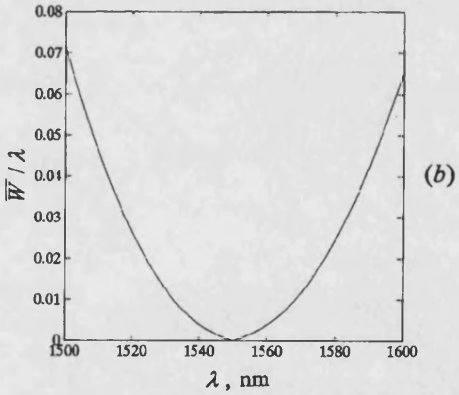

Fig. 4.8. **(a) Stationary anastigmatic mount on the sagittal straight line** (α_0=20.95274°, β_0=8.186875°) **and its RMS wave aberration (b).**

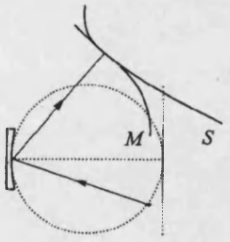

(*a*)

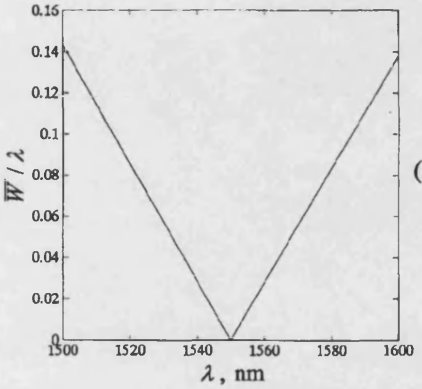

(*b*)

Fig. 4.9. **(a) Superstationary anastigmatic mount with normal imaging and (b) its RMS wave aberration.**

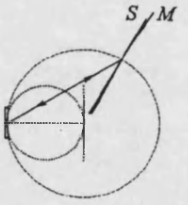

(*a*)

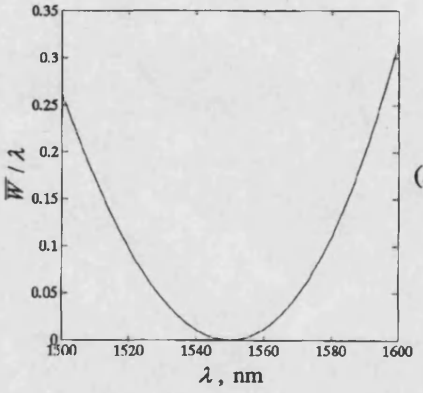

(*b*)

Fig. 4.10. **(a) Stationary anastigmatic Littrow mount ($\alpha_0 = \beta_0 = 30^\circ$) and (b) its RMS wave aberration.**

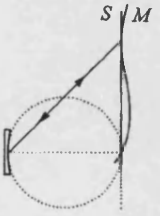

(*a*)

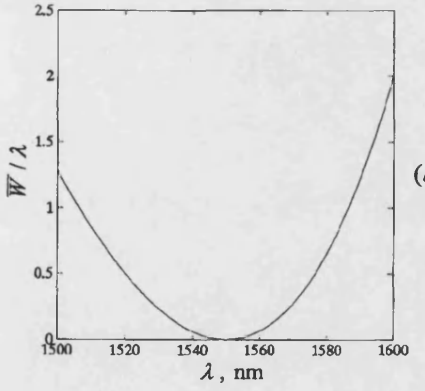

(*b*)

Fig. 4.11. **Same as Fig. 4.10 except** $\alpha_0 = \beta_0 = 45^\circ$.

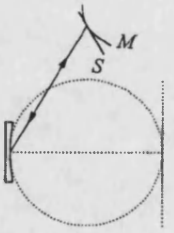

(*a*)

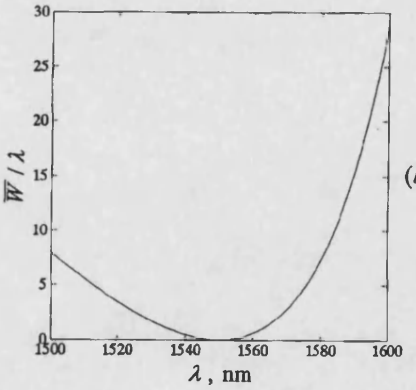

(*b*)

Fig. 4.12. **Same as Fig. 4.10 except** $\alpha_0 = \beta_0 = 60^\circ$.

4.6.4 Littrow mount

In this mount the positions of the source and its image coincide at $\lambda = \lambda_0$, i.e.

$$r_{\alpha 0} = r_{\beta 0}, \quad \alpha_0 = \beta_0 \ , \qquad (4.28)$$

but they can be separated by a small displacement of the input and output fibres from the dispersion plane. Substituting Eqs.(4.28) into Eq.(4.15) provides

$$r_{\alpha 0} = 2R\cos\alpha_0 \qquad , \qquad (4.29)$$

Three Littrow mounts satisfying Eqs.(4.28, 4.29) with $\alpha_0 = 30°$, $\alpha_0 = 45°$ (Sakayanagi mount) and $\alpha_0 = 60°$ are shown in Figures 4.10, 4.11 and 4.12, respectively. Equation (4.29) implies that all stationary anastigmatic Littrow mounts lie on the circle of radius R (a factor of 2 larger than that of the Rowland circle) shown in Fig. 4.10 by a dashed line. Using Eq.(4.15) it can be also shown that for a source located at the centre of the grating curvature ($\alpha_0 = 0$, $r_{\alpha 0} = R$) the stationary anastigmatic images can be formed only on this circle. Moreover, there is an interesting feature, the grating operating in this configuration in the k-th diffraction order also provides stationary anastigmatic imaging in the Littrow mount, but in the $2k$-th order.

The stationary anastigmatic Littrow mount is incompatible with Rowland circle, normal imaging and superstationary astigmatism, which can be easily proved after substituting Eqs (4.28) into Eq.(4.22), Eqs(4.26, 4.27) and Eqs (4.18, 4.19), respectively.

4.6.5 Wadsworth mount

In the well-known Wadsworth mount [2] a parallel beam ($r_{\alpha 0} = \infty$) incident at an arbitrary angle forms, after diffraction, a stationary anastigmatic focus on the x axis ($\beta_0 = 0$). Although Eq.(4.15) in this case contains an undefined product of 0∞, Eqs.(4.26, 4.27) provide the family of Wadsworth mounts with normal imaging described by

$$r_{\beta 0} = R/(1+\cos\alpha_0) \ . \qquad (4.30)$$

The performances of three Wadsworth mounts for $\alpha_0 = 60°$: $r_{\beta 0} = R/2$, $r_{\beta 0} = R/1.5$ (normal imaging), and $r_{\beta 0} = R$ shown in Figures 4.13, 4.14, and 4.15 respectively. Mounts with $r_{\beta 0} = R$ have been studied by Peisakhson [21] who showed that the sagittal focal curve in this case is a straight line parallel to the incident beam and described how these gratings can be holographically recorded.

It is interesting to note that stationary anastigmatic mounts for a parallel incident beam can also be realised off the x-axis. Substituting $r_{\alpha 0} = \infty$ in Eq.(4.15) provides for $\beta_0 \neq 0$

$$\frac{1}{r_{\beta 0}} = \frac{\sin\beta_0[1+\cos(\beta_0 - \alpha_0)]}{2R\, q_0 \cos\beta_0} \quad . \qquad (4.31)$$

With the same substitution Eqs.(4.26, 4.27) for the normal imaging mount become

$$\begin{cases} \sin\beta_0 = -2\sin\alpha_0 & (4.32) \\ \dfrac{1}{r_{\beta 0}} = \dfrac{1+\cos(\beta_0 - \alpha_0)}{R\cos\beta_0} & (4.33) \end{cases}$$

One mount satisfying Eqs.(4.32, 4.33) ($\alpha_0 = -20.70481°$, $\beta_0 = 45°$, $r_{\beta 0} = 0.50098R$) is shown in Fig. 4.16. Eqs.(4.18, 4.19), which ensure superstationary astigmatism, can also be solved for $r_{\alpha 0} = \infty$, the mount example with parameters $\alpha_0 = -11.75530°$, $\beta_0 = 33.62344°$, $r_{\beta 0} = 0.618326R$ satisfying these conditions is shown in Fig. 4.17.

Finally, consider one more superstationary anastigmatic mount with parameters $\alpha_0 = 30°$, $\beta_0 = 12.77°$, $r_{\alpha 0} = 2.146733R$, $r_{\beta 0} = 1.66327R$ (see Fig. 4.18). In this mount both the meridional and sagittal focal curves are close to a straight line, corresponding to a flat image surface, desirable for devices using arrays of detectors or fibres in the output plane .

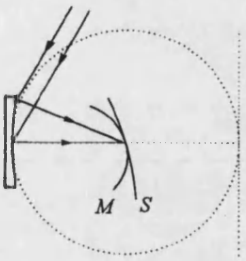

(a)

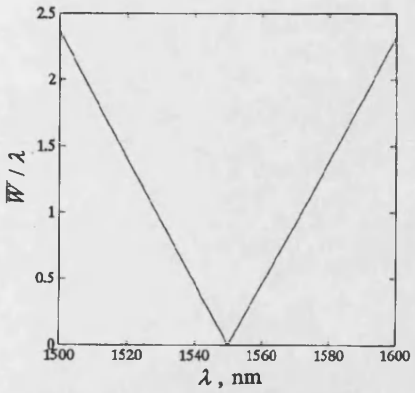

(b)

Fig. 4.13. **(a) Wadsworth mount (α_0 =60°, $r_{\beta 0}$=R/2) and its RMS wave aberration (b).**

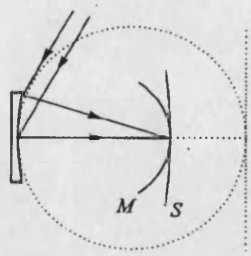

(a)

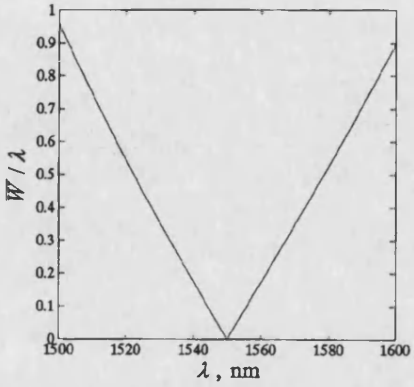

(b)

Fig. 4.14. **Same as Fig. 4.13 except normal imaging** (α_0=60°, β_0=R/1.5).

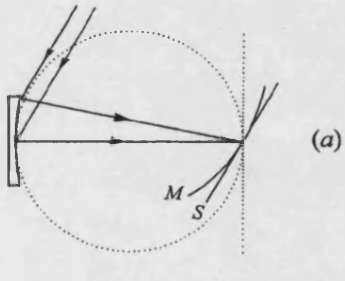

(a)

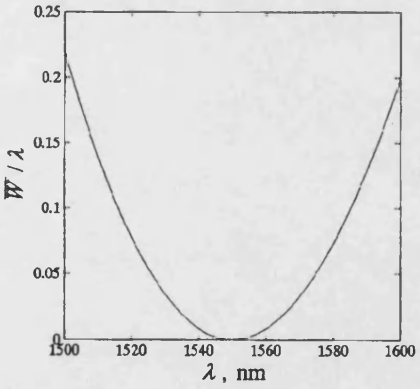

(b)

Fig. 4.15. **Same as Fig. 4.13 except** $r_{\beta 0}$=R .

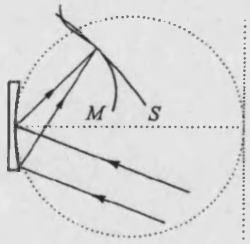

(a)

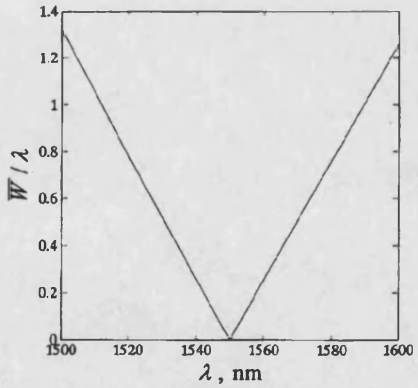

(b)

Fig. 4.16. **(a) Normal imaging for parallel incident beam** (α_0 = -20.7048°,β_0 =45°, $r_{\beta 0}$=0.501R) **and (b) its RMS wave aberration.**

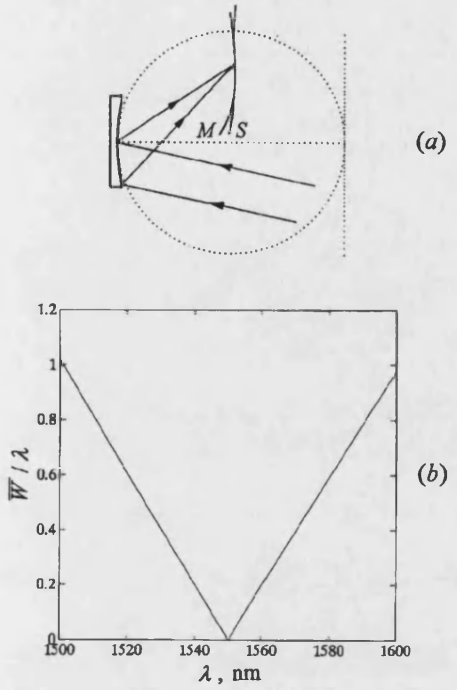

Fig. 4.17. **(a) Superstationary anastigmatic mount for parallel incident beam** (α_0=-11.75530°, β_0=33.62344°, $r_{\beta 0}$=0.618326R) **and (b) its RMS wave aberration.**

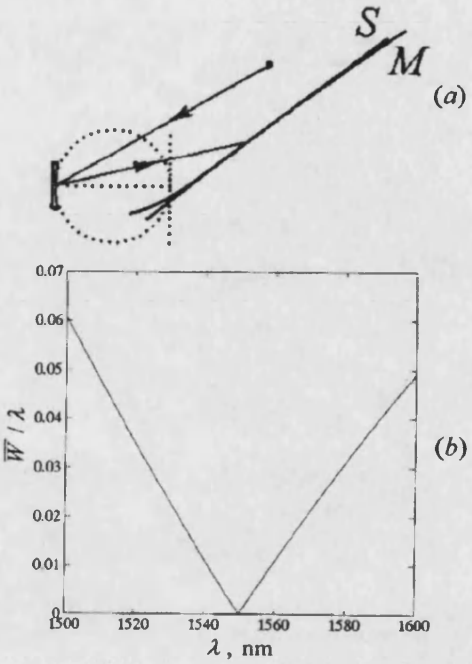

Fig. 4.18. **(a) Superstationary anastigmatic mount with flat image surface** (α_0=30°, β_0=12.77°, $r_{\alpha 0}$=2.146733R, $r_{\beta 0}$=1.66327R) **and (b) its RMS wave aberration.**

4.7. Discussion of the presented mounts

The spectral diagrams of the RMS wave aberration in Figures from 4.4 to 4.18 allow comparison of the performance of the various mounts. The pseudo parabolic dependence of RMS wave aberration in Figures 4.5, 4.6, 4.7, 4.8, 4.10, 4.11, 4.12, 4.15, means that the total aberration is practically stationary and ensures that coma and spherical aberrations are still negligibly small in comparison with astigmatism, because only astigmatism was required to be stationary. Additional computer simulations have shown that the main aberration in Figures 4.4, 4.16, 4.17, and 4.18 is meridional coma proportional to $\Delta\lambda\, y^3$. In Figures 4.9, 4.13, 4.14 the meridional coma is combined with the coma proportional to $\Delta\lambda\, yz^2$.

The mounts presented in Figures 4.4, 4.6, 4.7, 4.8, 4.18 provide diffraction limited performance in the spectral range 1500-1600 nm, whilst the mounts in Figures 4.9, 4.10, 4.15 provide the same only within the C-band 1525-1565 nm. The mounts of Figures 4.6-4.8 are optimal for using in WDM optical communication systems because of very good performance ($\overline{W} < \lambda / 70$) within the C-band, and close values of numerical apertures for the source and image.

For a wider operating spectral range, the parabolic aberration behaviour becomes a disadvantage in comparison with linear one and the superstationary mounts presented in Figures 4.4, and 4.18 will provide better performance then those in Figures 4.6-4.8.

The heavy penalty in chromatic aberration, which must be paid for an increase in the system angular dispersion, can be seen from the comparison of the Littrow mounts presented in Figures 4.10-4.12. These show that the chromatic RMS wave aberration of the optical system increases much faster than the grating spatial frequency $\nu_0 = q_0 / \lambda_0$, which determines the angular dispersion.

4.8. Additional improvement by introducing convex mirror

Characteristically all the mounts described above suffer from a narrow image field in the sagittal direction and, therefore, do not allow a large number of independent multi/demultiplexers be realized using the same grating, limiting the node throughput.

This section describes how the performance of narrow-band stationary anastigmatic spectrographs can be substantially improved by introducing a convex mirror into the optical scheme. This modification is based on ideas of the Offner 1:1 imaging system [22] consisting of concentric concave and convex mirrors which led to a number of publications

[23, 24] on concentric all-reflecting spectrographs. The Offner system provides stigmatic sagittal imaging and its meridional imaging suffers from higher order field curvature and residual spherical aberration only [25]. In concentric spectrographs the initial system symmetry cannot be maintained for all the wavelengths because of dispersion; however they provide essential compensation of aberrations, a flat field and allow the use of a long entrance slit. In a proposed modification the two principles of the Offner system are used, namely (i) the unit magnification and (ii) the algebraic sum of the two reflecting surface powers being zero. The third principle of the concentric reflecting surfaces is substituted by the condition that (iii) the convex mirror introduces no aberrations into the image at the wavelength of correction (in reality this means that the mirror is concentric to the intermediate image). Additionally, this scheme provides double diffraction at the concave grating, not used in the reported concentric versions [23, 24]. The software DEMOS [26] was used to ray-trace the spectrographs.

4.8.1 Basic concave grating spectrograph

Consider a stationary anastigmatic normal imaging mount of a concave grating satisfying Eqs. (4.26, 4.27) and shown in Fig. 4.19a (λ_0=1550 nm, R=270.4 mm, $r_{\alpha 0}$= $r_{\alpha 0}$=1.00123R, α_0=24.054167°, β_0=9.720003°, NA=0.11). The reciprocal linear dispersion is 9.8 nm/mm corresponding to 80 (0.5 nm spaced) channels within the spectral range 1530-1570 nm, separated by 51 μm in the image plane. The curvature of the sagittal focal curve is negligibly small whilst the meridional focal curve radius is close to R/2 (the Rowland circle radius). A ray tracing analysis was carried out using an ideal grating forming the aberration-free image at the central wavelength. The root-mean-square wave aberration within the operating spectral range did not exceed λ/40 for a source situated in the plane of dispersion. Fig. 4.20a shows the output spot diagrams calculated on the focal plane normal

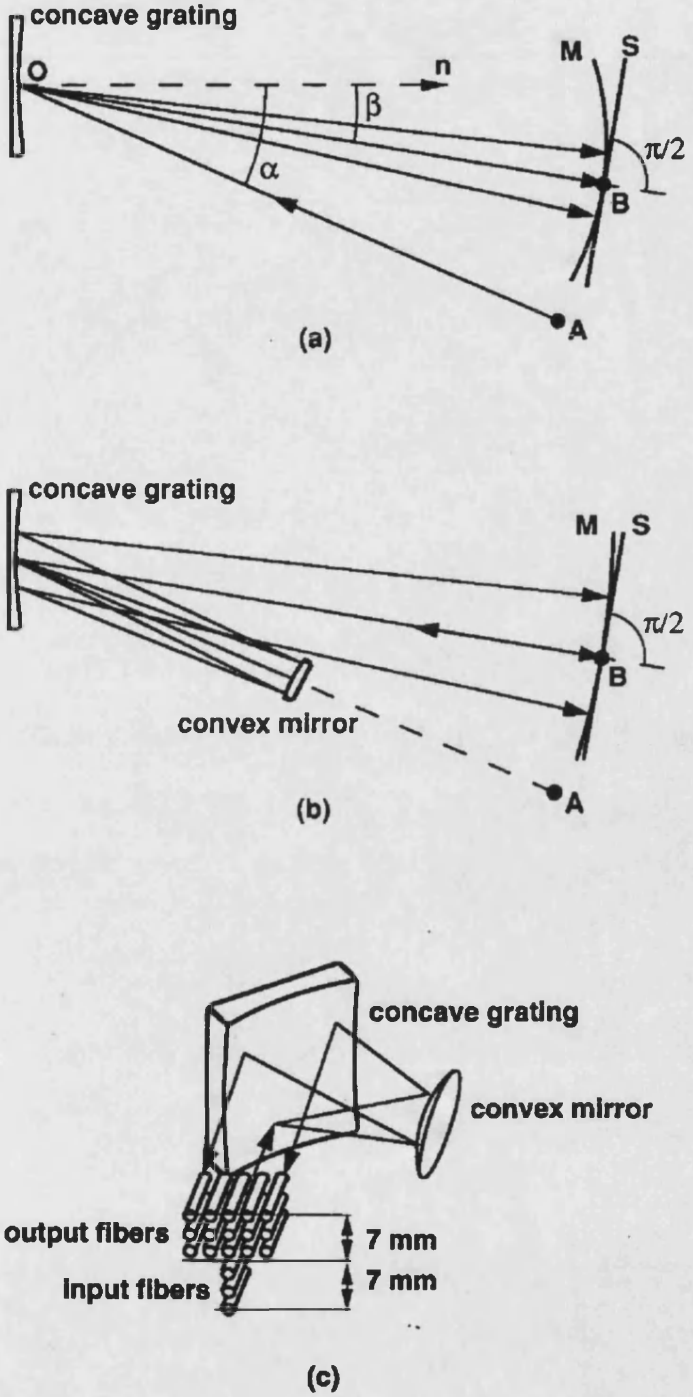

Fig.4.19. **The dispersion plane layout of a concave grating spectrograph (a), its retroreflective modification using a convex mirror (b), and positioning of input and output fibres in retroreflective demultiplexer (c).**

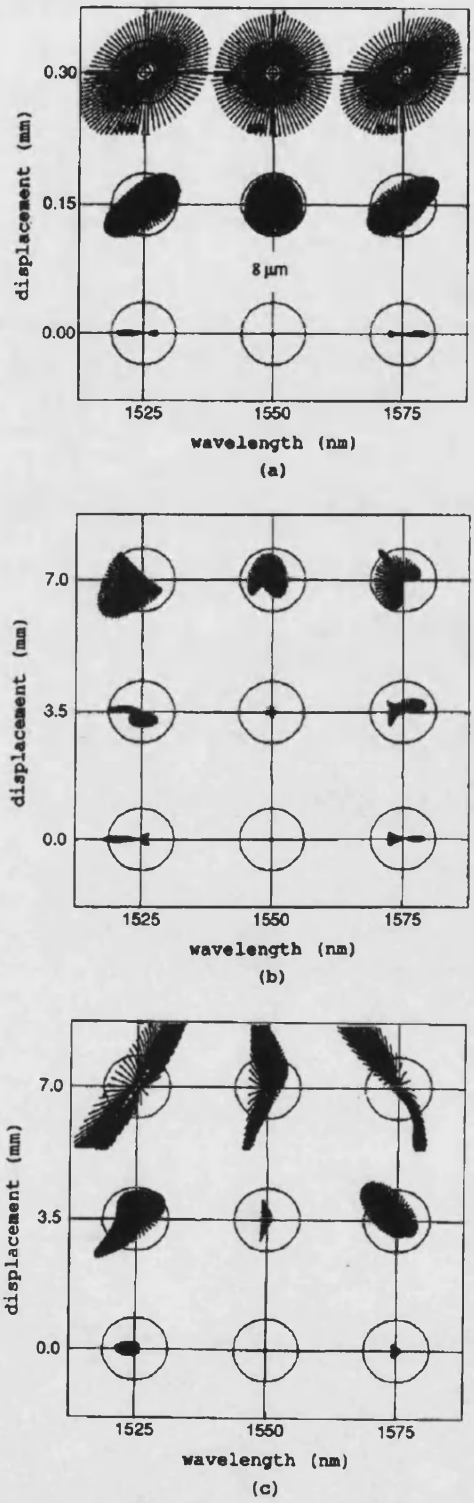

Fig.4.20. **Ray tracing spot diagrams at various wavelengths and source displacements with respect to the dispersion plane for concave grating spectrograph (a), and for its retroreflective modification with the convex mirror radius $R_2=R/2$ (b) and $R_2=0.433R$ (c).**

to the chief ray at the wavelength λ_0 for different source displacements h in the sagittal direction. The acceptable size of a spot diagram is restricted to the value of 8 μm corresponding to a typical diameter of the fundamental fibre mode at e^{-2} intensity level. This restriction leads to the permissible displacement h of 150 μm corresponding to only 7 input fibres, separated by 50 μm in sagittal direction, with the total number of channels of 7x80=560.

4.8.2 Retroreflective modification

The mount of a retroreflective spectrograph is shown in Fig. 4.19b. The source is placed at the former image point B and the grating now forms an aberration-free image at point A at the wavelength λ_0. A spherical convex mirror of radius $R_2=R/2$ is inserted concentric to the point A. It does not introduce any aberration into the image at the central wavelength, which is now formed at the source point B. Double diffraction at the concave grating results in approximately double dispersion and allows demultiplexing of 160 (0.25 nm spaced) channels within the same spectral range. The spot diagrams shown in Fig. 4.20(b) demonstrate the dramatic increase of the image field in the sagittal direction. The permissible displacement reaches 7 mm and we can use 140 parallel output fibre arrays corresponding to the total number of channels 140x160= 22400, i.e. 40 times larger. It should be noted that in this scheme the input and output fibres are separated by the dispersion plane, as shown in Fig. 4.19c.

The dispersed images on the focal plane of a point source having a spectral range of 1525 nm ≤ λ ≤ 1575 nm for any displacement h≤7mm are perfect straight lines of length 10216±1 μm parallel to the dispersion plane.

A key advantage which should be noted is that whilst for a basic concave grating spectrograph double dispersion, resulting from a factor of 2 smaller grating period, leads to a factor of 4 increase in astigmatism within the operating spectral region, in the retroreflective scheme it remains practically the same. This is due to the stationary type of astigmatism, which can also be compensated by the convex mirror concentric to the intermediate image. The radius of the meridional focal curve in the retroreflective scheme is about 4.5 times larger than in the basic scheme, which corresponds to a small under-compensation of astigmatism. Complete compensation is provided by the convex mirror radius R_2=0.433R (see Fig. 4.20c), however in this case there is a penalty of a factor of 2 reduction of the image field in the sagittal direction.

4.9 Conclusions

In this chapter, the general analytic formulae that define the parameters of spherical concave grating mounts providing stationary and superstationary astigmatism at the wavelength of correction are derived. Important special cases of concave grating mounts such as Rowland circle, sagittal straight line, normal imaging, Littrow and Wadsworth mounts are considered. The spectral diagrams of the RMS wave aberration demonstrate that the presented results can be readily used for design of diffraction-limited multi/demultiplexers for WDM systems and high-resolution narrow band spectrographs.

The stationary anastigmatic concave grating spectrograph has been modified into a novel retro-reflective scheme by introducing a convex mirror concentric to the intermediate image. The considerable advantages of this modification lie in (a) much larger image field in the sagittal direction providing the large number of parallel multi/demultiplexers, (b) a factor of two higher dispersion without an increase in chromatic astigmatism, as shown in Fig. 4.19 c, (c) the same grating can be used with and without a convex mirror. The

shortcomings of the modification are (a) an extra optical element, (b) increased loss especially for gratings with low diffraction efficiency, (c) it is a factor of two more critical to aberrations introduced during the grating fabrication process.

The results of this chapter are used for the design of the demultiplexer, wavelength router and channel equaliser, described in Chapters 5, 6, and 7, respectively. Specifically, the normal imaging mount of concave grating derived in a section 4.6.3 is the basis of a demultiplexer and a channel power equalizer and the Littrow mount from section 4.6.4 is used for the design of a router.

References to Chapter 4

[1] H. Noda, T. Namioka, and M. Seya, "Geometric theory of the grating", *J. Opt. Soc. Am.*, vol.64, 1974, pp.1031-1048.

[2] M.P.Chrisp, "Aberration-Corrected Holographic Gratings and Their Mountings", in *Applied Optics and Optical Engineering*, R.R.Shannon and J.C.Wyant, eds. (Academic, London, 1987), Vol.10, pp.391-454.

[3] J. Cordelle, J. Flamand, G. Pieuchard, and A. Labeyrie, "Aberration-corrected concave gratings made holographically", in *Optical Instruments and Techniques*, J. Home Dikson, ed. (Oriel, Newcastle upon Tyne, UK, 1970), pp. 117-124.

[4] R. Grange, "Aberration-reduced holographic spherical gratings for Rowland circle spectrographs", *Applied Optics*, vol.31, 1992, pp.3744-3749.

[5] T. Kita and T. Harada, "Use of aberration-corrected concave gratings in optical demultiplexers ", *Applied Optics*, vol.22, 1983, pp.819-825.

[6] E. Desurvire, *Erbium-doped fiber amplifiers: principles and applications*, New York, A Wiley-Interscience publication, 1994.

[7] E.G.Churin, P.Bayvel, A.Stavdas, J.E.Midwinter, A.M.Hill. "Stationary anastigmatic mounts of concave gratings", *Applied Optics*, vol.36, 1997, pp.3444-3451.

[8] E.G.Churin, P.Bayvel, V.B.Smirnitskii, F.N.Timofeev, J.E.Midwinter "Concave grating and convex mirror double dispersion spectrograph for optical network applications", *Applied Optics*, vol.36, 1997, pp.7822-7825.

[9] I.V.Peisakhson, and Yu. V. Bazharov, "Concave spherical diffraction gratings with compensated astigmatism in Rowland mountings", *Sov. J. Opt. Technol.*, vol.44, 1977, pp.273-276.

[10] H.Beutler, "The Theory of the Concave Grating", *J. Opt. Soc. Am.*, vol.35, 1945, pp.311-350.

[11] M. Born, and E. Wolf, *Principles of Optics*. Pergamon Press, London, 1970.

[12] T. Harada, and T. Kita, "Mechanically ruled aberration corrected concave gratings", *Applied Optics*, vol.19, 1980, pp.3987-3993.

[13] R. Grange, "Holographic spherical gratings: a new family of quasi-stigmatic designs for the Rowland circle mounting", *Applied Optics*, vol.32, 1993, pp.4875-4880.

[14] E.G. Churin, P.Bayvel, A.Stavdas, J.E.Midwinter, A.M.Hill. "Optimization of rowland circle mounts for grating demultiplexerrs and narrow-band spectrographs", *Optics Letters*, vol.21, 1996, pp.1084-1086.

[15] B. Gale, "The theory of variable spacing gratings", *Optica Acta*, vol.13, 1966, pp.41-54.

[16] Y. Sakayanagi, "A Stigmatic Concave Grating with Varying Spacing", *Sci. Light (Tokyo)*, vol.16, 1967, pp.129-137.

[17] D. Marcuse, "Loss analysis of single-mode fiber splices", *Bell System Technical Journal*, vol.56, 1977, pp.703-718.

[18] F.N. Timofeev, J.E. Midwinter, P. Bayvel, E.G. Churin, A. Stavdas, and M.N. Sokolskii, "Free-space aberration-corrected grating demultiplexer for application in densely-spaced, subnanometre wavelength-routed optical networks", *IEE Electronics Letters*, vol.31, 1995, pp. 1368-1370.

[19] A. Stavdas, P. Bayvel, J. E. Midwinter, "Design and performance of concave holographic gratings for applications as multiplexers/demultiplexers for wavelength routed optical networks", *Optical Engineering,* vol.35, 1996, pp.2816-2823.

[20] F.N. Timofeev, P. Bayvel, J.E. Midwinter, and M.N. Sokolskii, "High performance, free-space ruled concave grating demultiplexer", *IEE Electronics Letters*, vol.31, 1995, pp. 1466-1467.

[21] I.V.Peisakhson, "Holographic diffraction gratings, focusing parallel ray bundles", *Sov. J. Opt. Technol.*, vol.46, 1979, pp.338-340.

[22] A. Offner, " New Concepts in Projection Mask Aligners", *Optical Engineering,* vol.14, 1975, pp.130-132.

[23] L. Mertz, "Concentric spectrographs" , *Applied Optics*, vol.16, 1977, pp.3122-3124.

[24] N. C. Das and M. V. R. K. Murty "Flat field spectrograph using convex holographic diffraction grating and concave mirror." *Pramana - J. Phys.*, vol. 27, 1986, pp.171-192.

[25] A. Suzuki, "Complete analysis of a two-mirror unit magnification system" , Part 1, *Applied Optics*, vol.22, 1983, pp.3943-3949.

[26] M. A. Gan, D. D. Zhdanov, V. V. Novoselskiy, S. I. Ustinov, A. O. Fedorov, I. S. Potyemin, "DEMOS: State-of-the-art application software for design, evaluation, and modelling of optical systems", *Optical Engineering,* vol.31, 1992, pp.696-700.

Chapter 5

Concave holographic grating demultiplexer: design, fabrication and characterization

5.1 Introduction

One of the aims of the thesis was to design an athermal demultiplexer for 49, 100 GHz spaced, channels operating in the C-band. The optical frequency range 191500 GHz ≤ ν ≤ 196300 GHz corresponds to the wavelength in vacuum 1527.216 nm ≤ λ ≤ 1565.496 nm (at the central wavelength λ_0=1546.119 nm 100 GHz corresponds to 0.8 nm channel spacing). The work on assembly, and experimental verification of the concave holographic grating demultiplexer was carried out in E-Tek Dynamics from July 1999 till November 2000. The gratings were fabricated by American Holographic.

This chapter describes, in detail, the design procedure and theoretical analysis of a concave holographic grating demultiplexer, including a technique for calculating the transmission spectrum of each demultiplexer channel. In the design the period of the grating was chosen to minimize polarization dependent losses (PDL). A multimode interference coupler (MMI) was used at the input of the demultiplexer to flatten and broaden the channels' passband. The necessity to use an ultra-low thermal expansion housing and hermetic sealing to create an athermal device was demonstrated in this work. The adjustment and fixing procedures are described. Tolerance analysis and performance characteristics of a fully packaged demultiplexer are presented.

5.2 Design requirements and procedure

The design of a concave grating demultiplexer can be subdivided into two parts: the selection of a suitable mount (optical scheme of demultiplexer) and the optimization of the holographic recording scheme for this mount. First of all, before the start of the design of the demultiplexer, the requirements on the performance and, resultant restrictions on the optical scheme geometry were formulated. Then, the sequence in the design procedure and the possible iterations were determined. During the work at this thesis, the following requirements and design sequence were proposed:

1) Fixing the grooves' period at the grating centre. The period d has to be chosen to provide sufficiently high and approximately equal diffraction efficiencies for the S- and P-polarizations.

2) Stationary anastigmatic mount, required to guarantee small aberrations within the operating spectral range, is selected.

3) Normal incidence onto facet of output fibre array, to avoid technological difficulties when fabricating fibres in a V-groove chip. Points 2) and 3) are defined by solving the simultaneous equations (4.26, 4.27).

4) Approximately one-to-one imaging ($r_{\alpha 0}/r_{\beta 0} \approx 1$), so that the fibre mode and its image are close in size. This is necessary to avoid additional losses due to mode mismatch.

5) The choice of linear dispersion to determine the spacing between the output fibres.

At the first stage of the design procedure, in the point 4 above, the accurate fulfilment of $r_{\alpha 0}/r_{\beta 0} \equiv 1$ is established. Therefore, the first four requirements completely define four parameters $r_{\alpha 0}/R$, $r_{\beta 0}/R$, α_0, β_0 (for the notation see Chapter 4) of the dimensionless geometry of the mount. The addition of the point 5 determines the grating curvature radius R and all the optical scheme dimensions.

At the second step the computer optimization of holographic recording scheme is realized to minimize the aberrations at the central wavelength.

At the third stage some deviation from the unity ratio $r_{\alpha 0}/r_{\beta 0}$ within predetermined boundaries is introduced, and the full procedure is repeated. Small variations of the value $r_{\alpha 0}/r_{\beta 0}$ allow additional freedom, and results in better performance of designed optical scheme. These iterations are continued until the minimum aberrations are obtained.

The choice of grating period, linear dispersion, boundaries for $r_{\alpha 0}/r_{\beta 0}$ ratio, and the design procedure are described in detail in the following sections.

5.3 Grating period and PDL

Low-frequency holographic gratings with sinusoidal profile are considered to have low diffraction efficiencies in comparison to ruled blazed gratings. The efficiency of gratings in the region $\lambda/d<0.2$, where d is the groove spacing, can be determined from scalar theory [1]. This theory predicts a maximum diffraction efficiency $\eta(\lambda)$ of 34% for a sinusoidal grating and 100% for a blazed grating. Moreover, the S- and P-polarization efficiency curves $\eta(\lambda)$ are essentially the same. When the wavelength is of the same order as the groove depth h and period, electromagnetic theory is used to predict the diffraction efficiencies. This leads to an important result that high efficiencies can be also obtained with sinusoidal gratings. However, the efficiency curve for the S-polarization differs from that for the P-polarization substantially, and thus, for low polarization dependent losses it is necessary to operate in the vicinity of their intersection point.

High-efficiency sinusoidal gratings can be achieved if the wavelength and the groove spacing d allow only one diffraction order to propagate. The energy from the grating is then shared between this diffracted order and the zero order. By adjusting the groove depth all

the energy can be channelled into the diffracted order. An experimental efficiency of 75% for a holographic sinusoidal grating has been measured by Hutley [2], and the condition for high diffraction efficiency was $0.7<\lambda/d<1.65$, assuming angles of incidence and diffraction of less than 60° from the normal [3].

Diffraction grating efficiencies calculated from the electromagnetic theory have been clearly presented by Loewen *et al.* [4]. These authors give the efficiency curves for P- and S-polarization, using the infinite-conductivity model, for the sinusoidal plane periodic gratings operating in reflection mode.

The application of electromagnetic theory for the calculation of diffraction efficiencies is beyond the subject of this thesis and is not presented here. However, according to [4] the groove period at the grating centre was chosen to satisfy

$$\lambda_0/d=\sin\alpha_0+\sin\beta_0=0.849 \quad (5.1)$$

corresponding to the intersection of the efficiency curves for the profile depth $h=0.36d$. It should be noted that the concave grating has variable spacing and curved grooves, and, besides this, is illuminated by a diverging beam, so that the diffraction conditions vary across the grating area. Because of this, during the gratings' fabrication (all gratings described here were fabricated by American Holographic) the groove depth was adjusted so, that integrated across the grating area, the diffraction efficiencies for S- and P-polarizations are equal at the wavelength of 1546 nm.

Before use in the demultiplexer each grating was experimentally evaluated to measure PDL in the following way. Monochromatic light from a tunable polarized laser source was coupled into a polarization scrambler. The scrambler output was connected to the input fibre, fixed in the designed position relative to the concave grating. The optical power meter, placed at the grating focus was used to measure the power of the light diffracted by the grating. First, by scrambling all the possible polarization states, the

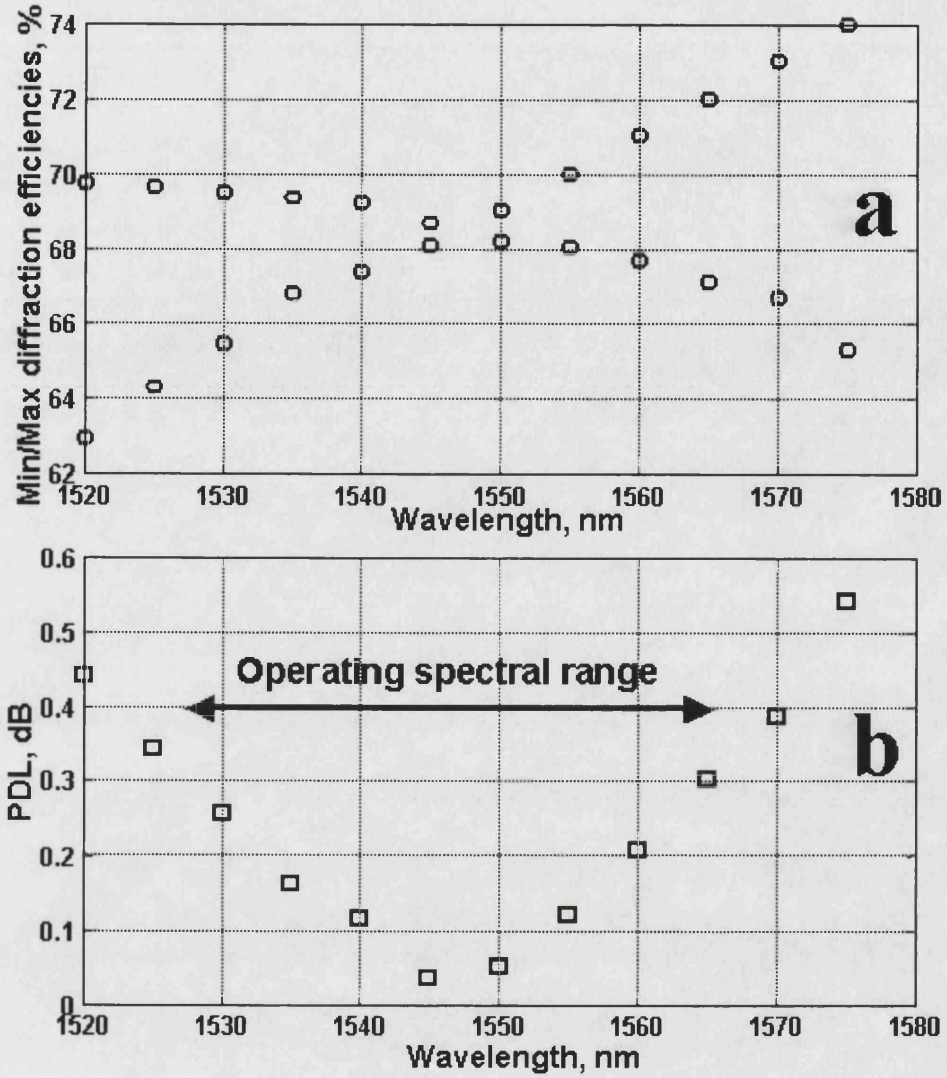

Fig.5.1. **Minimum and maximum measured diffraction efficiencies (a), and PDL (b) of concave grating.**

minimum and maximum diffraction efficiencies η_{min} and η_{max} were found for 12 wavelengths. Then PDL was calculated as $10\log_{10}(\eta_{max}/\eta_{min})$. Typical experimentally measured data for the minimum and maximum diffraction efficiencies and PDL are shown in Fig. 5.1a and b, respectively. Generally, over the operating spectral range PDL did not exceed 0.4 dB.

5.4 Linear dispersion

The angular dispersion at the central wavelength can be easily derived from Eq. (4.8) as

$$\left.\frac{d\beta}{d\lambda}\right|_{\lambda=\lambda_0} = \frac{\sin\alpha_0 + \sin\beta_0}{\lambda_0 \cos\beta_0}$$

The linear dispersion $D_L = r_{\beta 0} \cdot d\beta/d\lambda$ was chosen to be

$$D_L = r_{\beta 0} \frac{\sin\alpha_0 + \sin\beta_0}{\lambda_0 \cos\beta_0} = 0.05 \text{ mm/nm}, \quad (5.2)$$

corresponding to 40 μm spacing between adjacent output fibres. This spacing is large enough from the crosstalk point of view, and can be realized technologically by etching the cladding of standard 125 μm single mode fibres [5].

5.5 Optimization of the grating mount and recording scheme

5.5.1 Initial mount and recording scheme

All the parameters of the mount of concave grating, operating in the first diffraction order (k=1), are defined for the central wavelength λ_0=1546.112 nm. The holographic grating was recorded using light from an Ar-laser at λ_H=457.935 nm.

At the initial step it is required that the grating mount should satisfy the condition

$r_{\alpha 0}=r_{\beta 0}$. (5.3)

Solving the simultaneous Equations (4.26), (4.27), (5.1), (5.2), and (5.3) defines uniquely the demultiplexer mount as follows:

R=87.5912 mm, $r_{\alpha 0}$=$r_{\beta 0}$=88.1952 mm, α_0=36.89380°, β_0=14.39861°.

That is the same class of mounts as in Fig. 4.6, but with different grating period.

Besides the chromatic aberrations of an "ideal" grating described in Chapter 4, a holographic grating introduces additional aberrations. This is because the resultant holographic grating function $m_H(y,z)$ differs from the ideal one $m(y,z)$. The holographic grating is produced by exposing a photoresist-coated substrate to the interference pattern generated by two coherent point sources $C\,(x = r_C\cos\gamma,\ y = r_C\sin\gamma,\ z = 0)$, and $D\,(x = r_D\cos\delta,\ y = r_D\sin\delta,\ z = 0)$ shown in Fig. 5.2. The grating function for

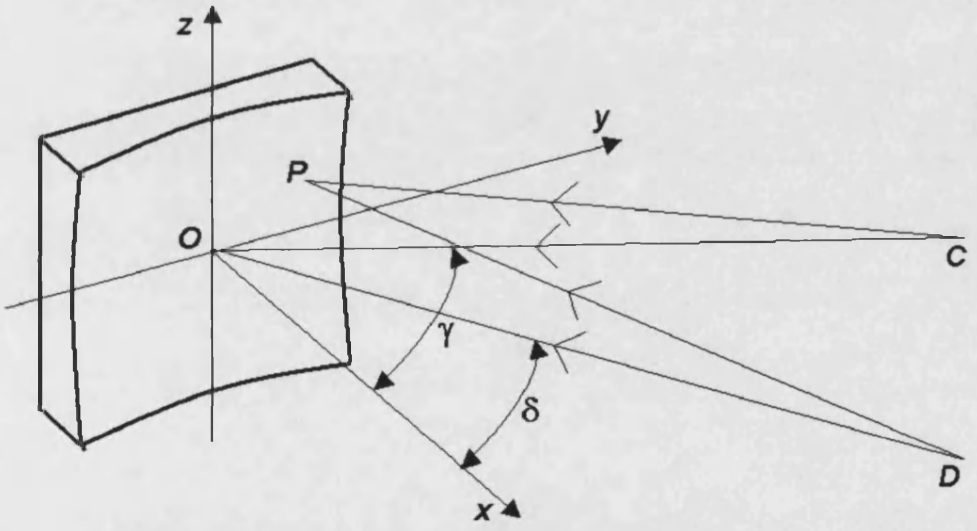

Fig.5.2. **Illustrating the holographic recording scheme.**

holographic concave grating with the curvature radius R is given [6] by:

$$m_H(y,z\,|\,\lambda_H,\gamma,\delta,r_C,r_D) = \frac{1}{\lambda_H}[< CP > - < DP > -(r_C - r_D)], \quad (5.4)$$

where

$$< CP >= \sqrt{(r_C\cos\gamma - x(y,z))^2 + (r_C\sin\gamma - y)^2 + z^2} \quad ,$$

$$< DP >= \sqrt{(r_D \cos\delta - x(y,z))^2 + (r_C \sin\delta - y)^2 + z^2} \quad ,$$

$$x(y,z) = R - \sqrt{R^2 - y^2 - z^2} \, .$$

At the wavelength λ_0 wave aberration of the holographic grating operating in the first diffraction order is

$$W_0(y,z) = \lambda_0[m_H(y,z \mid \lambda_H, \gamma, \delta, r_C, r_D) - m(y,z \mid \lambda_0, \alpha_0, \beta_0, r_{\alpha 0}, r_{\beta 0})] \quad ,$$

where $m(y,z)$ is defined from Eq. (4.3).

Expanding W_0 into a power series yields

$$W_0(y,z)=A_{10}y+A_{20}y^2+A_{02}z^2+A_{30}y^3+A_{12}yz^2+A_{40}y^4+A_{22}y^2z^2+A_{40}z^4+...$$

The terms with odd powers of z are absent due to the symmetry relative to dispersion plane. The explicit forms of first three coefficients are given as follows [6]:

$$A_{10} = -\sin\alpha_0 - \sin\beta_0 + \frac{\lambda_0}{\lambda_H}(\sin\gamma - \sin\delta),$$

$$A_{20} = \frac{1}{2}\left(\frac{\cos^2\alpha_0}{r_{\alpha 0}} + \frac{\cos^2\beta_0}{r_{\beta 0}} - \frac{\cos\alpha_0 + \cos\beta_0}{R}\right) - \frac{\lambda_0}{2\lambda_H}\left(\frac{\cos^2\gamma}{r_C} - \frac{\cos^2\delta}{r_D} - \frac{\cos\gamma - \cos\delta}{R}\right)$$

$$A_{02} = \frac{1}{2}\left(\frac{1}{r_{\alpha 0}} + \frac{1}{r_{\beta 0}} - \frac{\cos\alpha_0 + \cos\beta_0}{R}\right) - \frac{\lambda_0}{2\lambda_H}\left(\frac{1}{r_C} - \frac{1}{r_D} - \frac{\cos\gamma - \cos\delta}{R}\right).$$

The recording scheme has four free parameters: γ, δ, r_C, and r_D. The angle δ was varied during the optimization to minimize the RMS wave aberration $\overline{W_0}$ expressed in Eq. (4.11), whilst other three parameters were defined by setting A_{10}=A_{20}=A_{02}=0 as follows:

$$\gamma = \arcsin\left[\frac{\lambda_H}{\lambda_0}(\sin\alpha_0 + \sin\beta_0) + \sin\delta\right]$$

$$r_D = \frac{\sin^2\delta/\sin^2\gamma - 1}{\frac{\lambda_H}{\lambda_0}\left(\frac{1}{r_{\alpha 0}} + \frac{1}{r_{\beta 0}} - \frac{\cos\alpha_0 + \cos\beta_0}{r} - \frac{\sin^2\alpha_0}{r_{\alpha 0}\sin^2\gamma} - \frac{\sin^2\beta_0}{r_{\beta 0}\sin^2\gamma}\right) + \frac{\cos\gamma - \cos\delta}{r}}$$

$$r_C = \frac{\sin^2 \gamma}{\frac{\lambda_H}{\lambda_0}\left(\frac{\sin^2 \alpha_0}{r_{\alpha 0}} + \frac{\sin^2 \beta_0}{r_{\beta 0}}\right) + \frac{\sin^2 \delta}{r_D}}$$

For the initial concave grating mount, the optimization procedure resulted in $\overline{W}_0 = 0.059\lambda$ within NA=0.11, and yielded the following parameters for the recording scheme:

r_C=156.3741 mm; r_D=111.8399 mm; γ=59.85671°; δ=37.82940°

The facets of fibres at the demultiplexer output must be fixed at the straight line *MM'* perpendicular to the segment *OB*, as shown in Fig. 5.3. At an arbitrary wavelength λ the wave aberration of the holographic grating on this line may be represented as

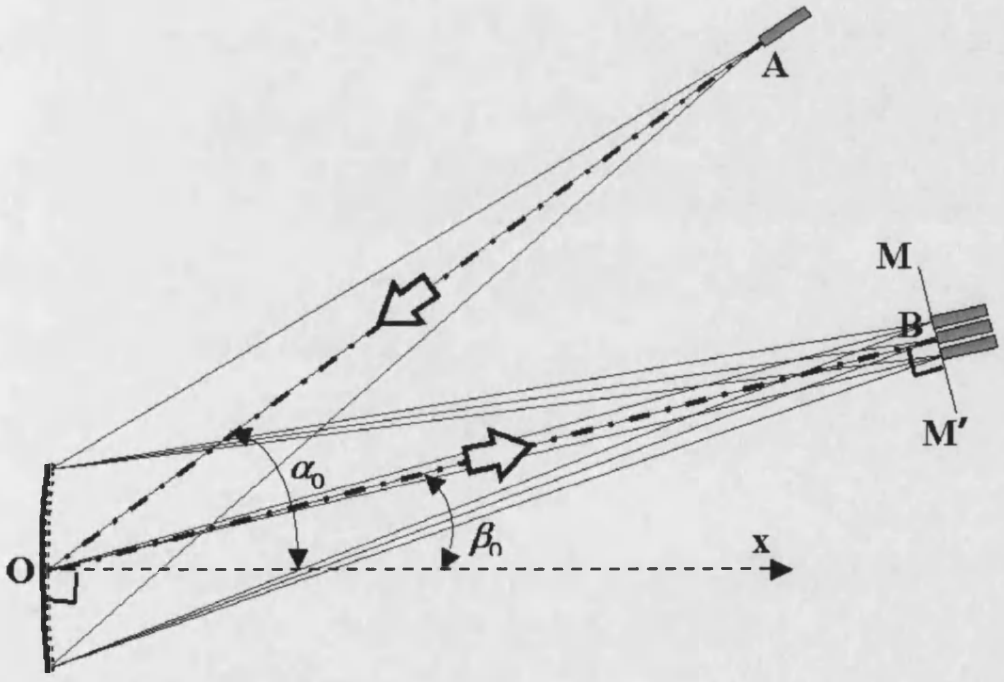

Fig.5.3. **Schematic diagram of demultiplexer.**

$$W(y,z) = \lambda[m_H(y,z \mid \lambda_H, \gamma, \delta, r_C, r_D) - m(y,z \mid \lambda, \alpha_0, \beta(\lambda), r_{\alpha 0}, r_\beta(\lambda))], \quad (5.5)$$

where $\beta(\lambda)$ is defined by Eq.(4.8), m_H and m are from Eq.(5.4) and Eq.(4.3),

respectively, and $r_\beta(\lambda)=r_{\beta 0}/\cos[\beta(\lambda)-\beta_0]$.

The RMS wave aberrations $\overline{W}(\lambda)$, calculated over diameter D=19.4 mm (input NA=0.11) for the ideal and holographic gratings after the first iteration, are shown in Fig. 5.4a.

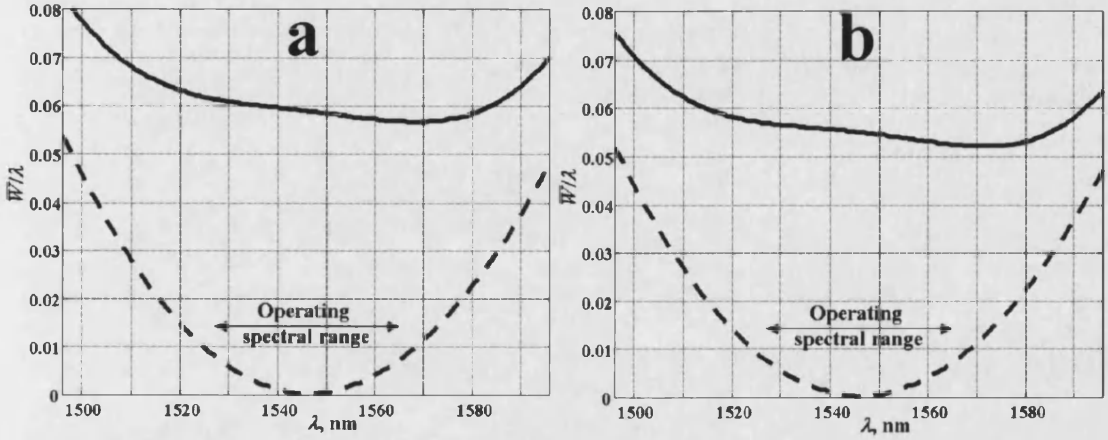

Fig. 5.4. **RMS wave aberration as a function of wavelength for initial (a) and final (b) step of design procedure. Dashed line is for ideal grating and solid line is for holographic grating.**

5.5.2 Final mount and recording scheme

In the next stages of the design process the ratio $r_{\alpha 0}/r_{\beta 0}$ was varied within the limits 0.95÷1.05 and for each case the procedure described in the previous section was started from the beginning. The process was terminated when a minimum wave aberration of $\overline{W}_0 = 0.055\lambda$ was achieved, corresponding to the final grating mount

R=86.5206 mm, $r_{\alpha 0}$=85.6452 mm, $r_{\beta 0}$=88.0950 mm, α_0=36.59011°, β_0=14.65°

and the recording scheme

r_C=151.2318 mm; r_D=107.4626 mm; γ=61.17258°; δ=38.65402°.

The RMS wave aberrations $\overline{W}(\lambda)$ calculated over the grating diameter D=18.8 mm (input NA=0.11) for the ideal and holographic gratings after the last iteration are shown in Fig. 5.4b. The wave aberration within the operating spectral range for the "ideal grating" is

approximately a factor of 5 lower than that for the real holographic grating. However, $\overline{W}$ for the real grating does not exceed $\lambda/17$, and, according to the Marechal criterion ($\overline{W} \le \lambda/14$), the image quality can be considered as diffraction limited. To confirm this, ray tracing spot diagrams were calculated (using the ZEMAX software) for uniformly illuminated grating (D=18.8 mm) and are shown in Fig. 5.5a. It can be seen that all the rays are within the Airy radius [7] $R_A=0.61\lambda_0/\mathrm{NA}=8.6$ μm, that is falling within the fibre core. The wave aberration as a function of y,z-coordinates on a grating surface is shown in Fig. 5.5b, the main contribution (approximately 70%) is from the balanced coma, proportional to y^3-3.4yz^2. The image of the focused spot and its cross-section in the dispersion plane, calculated numerically by means of Fourier analysis, are shown in Fig. 5.5c, and d, respectively.

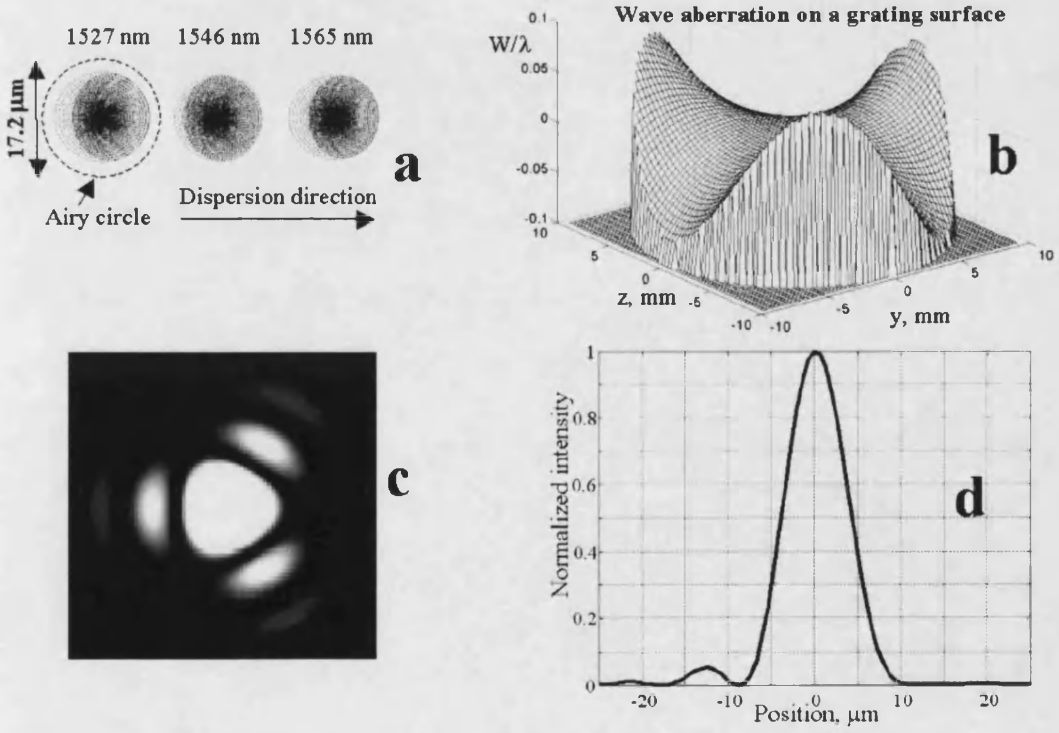

Fig.5.5. **Aberration analysis of designed demultiplexer. (a) Ray-tracing spot diagrams; (b) wave aberration map; (c) image pattern; (d) image intensity profile in the dispersion plane.**

5.5.3 Coupling losses due to mode mismatch and tilts

The main losses in the designed concave grating demultiplexer, caused by aberrations, misalignments, and limited diffraction efficiency, will be discussed later. In this sub-section, the losses caused by the geometry of the optical scheme are estimated for the Gaussian fibre mode approximation using equations from reference [8].

Firstly, consider the effect of tilted incidence onto a fibre facet. The central channel is coupled normally to the central fibre, whilst edge channels are coupled at the angle of θ=±0.65°. For the fibre mode radius w_0=5 μm and a wavelength λ=1546 nm this corresponds to the loss

$$L_{ang} = -10\log_{10}\{\exp[-(\pi w_0 \sin\theta/\lambda)^2]\} = 0.057\,\text{dB}. \quad (5.6)$$

Secondly, the deviation from the one-to-one imaging ($r_{\alpha 0}/r_{\beta 0}$=0.96) results in a mismatch between the fibre mode (radius w_0) and its image (radius w_1) and introduces an additional loss

$$L_m = -10\log_{10}\left[\frac{4}{(w_1/w_0 + w_0/w_1)^2}\right] = -10\log_{10}\left[\frac{4}{(r_{\beta 0}/r_{\alpha 0} + r_{\alpha 0}/r_{\beta 0})^2}\right] = 0.007\,\text{dB}$$

Thirdly, consider the effect of the fibre mode compression in the direction of dispersion (y). This happens due to broadening of output beam by the factor of $\cos\beta_0/\cos\alpha_0$=1.2, and results in a loss

$$L_{my} = -10\log_{10}\left[\frac{2}{w_{1y}/w_{0y} + w_{0y}/w_{1y}}\right] = 0.07\,\text{dB}.$$

Thus, it can be see that the described "geometrical" losses are negligible compared to diffraction efficiency of –1.7 dB (68%) for the fabricated holographic gratings and can be neglected in the subsequent analysis.

5.5.4 Non-uniform spacing between the output fibres

The spacing between output fibres is not constant, and this effect cannot be neglected for a large number of channels [9]. The channel frequencies are given by ν_J=193900-100J GHz, where -24≤J≤24. According to Eq.(4.8), diffraction angles for the corresponding wavelengths are

$$\beta_J = \arcsin[\frac{\lambda_J}{\lambda_0}(\sin\alpha_0 + \sin\beta_0) - \sin\alpha_0], \quad (5.7)$$

and the facets of the output fibres are at the points

$$B_J\ (x = r_{\beta J}\cos\beta_J, y = r_{\beta J}\sin\beta_J, z = 0) \quad (5.8)$$

where

$$r_{\beta J}=r_{\beta 0}/\cos(\beta_J-\beta_0) \quad (5.9)$$

Positions Y_J of output fibres on the line MM', shown in Fig. 5.3, are defined from

$$Y_J = r_{\beta 0}\tan(\beta_J - \beta_0). \quad (5.10)$$

This gives variations in fibre spacing $Y_{J+1} - Y_J$ from 38.98 to 41.12 μm within the operating spectral range. The fibre-in-the-V-groove non-uniform array was fabricated by ZYGO corporation (USA) on a silicon wafer according to Eq.(5.10) with absolute position accuracy of 0.2 μm.

5.6 Transmission spectrum as an overlap integral

The wave aberration for the "imaging" point $A\ (x = r_{\alpha 0}\cos\alpha_0, y = r_{\alpha 0}\sin\alpha_0, z = 0)$ into point B_J (5.8) at arbitrary wavelength λ is given by

$$W_{ABJ}(y,z) = \lambda[m_H(y,z\,|\,\lambda_H,\gamma,\delta,r_C,r_D) - m(y,z\,|\,\lambda,\alpha_0,\beta_J,r_{\alpha 0},r_{\beta J})], \quad (5.11)$$

where β_J, $r_{\beta J}$, m_H and m are defined by (5.7), (5.9), (5.4) and (4.3), correspondingly. The coupling efficiency η_J from input fibre into the output fibre in the point B_J at a wavelength λ can be calculated from an overlap integral [10] at the grating surface σ

$$\eta_J(\lambda) = \left| \iint_{\sigma} |E_A E_{BJ}| \exp(j2\pi W_{ABJ} / \lambda) dydz \right|^2 , \qquad (5.12)$$

where $E_A(y,z)$ is the normalized amplitude of the input fibre mode at the grating, and $E_{BJ}(y,z)$ is that of the output fibre number J. The amplitudes on the grating surface were calculated in scalar approximation as Fresnel-Kirchhoff integrals [7].

Refer to Fig. 5.6 to define a Cartesian co-ordinate systems (x,y,z) with the origin at the grating centre, (y_A,z_A) and (y_{BJ},z_{BJ}) with origins at the centre of input and J-th output fibre facet, respectively. The axes x, y, y_A and y_{BJ} lie in the dispersion plane, and the axes z, z_A and z_{BJ} are normal to the dispersion plane.

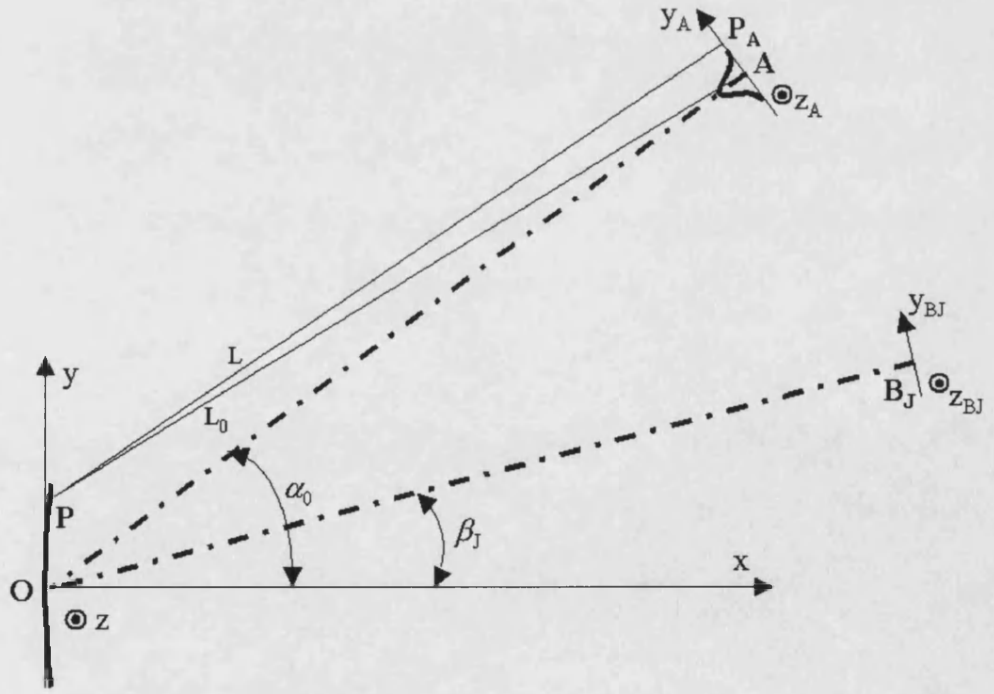

Fig. 5.6. **Illustrating the derivation of the amplitude on the grating surface**

Consider an input fibre, the distance L from any point $P_A(y_A,z_A)$ on a fibre facet Ω to arbitrary point $P(y,z)$ on the grating surface may be expressed in the form

$$L=[(r_{\alpha 0}\cos\alpha_0 - y_A\sin\alpha_0 - x(y,z))^2+(r_{\alpha 0}\sin\alpha_0 + y_A\cos\alpha_0 - y)^2+(z_A-z)^2]^{1/2}, \quad (5.13)$$

where $x(y,z)$ is from Equation (4.1) of the grating surface. The distance L_0 from the centre of fibre facet to the point P is

$$L_0=[(r_{\alpha 0}\cos\alpha_0 - x(y,z))^2+(r_{\alpha 0}\sin\alpha_0 - y)^2+z^2]^{1/2}. \quad (5.14)$$

The amplitude from an input fibre at the point $P(y,z)$ is given by

$$E_A(P)=\frac{a}{L_0}\iint_{\Omega}\psi\exp(j2\pi L/\lambda)dy_A dz_A\ , \quad (5.15)$$

where the fibre mode field $\psi(\sqrt{y_A^2+z_A^2})$ is described by (3.2), and normalizing parameter a is defined from the condition $\iint_{\sigma}|E_A|^2 dydz=1$. The amplitude from the output fibre is calculated similarly.

The intensity distributions $|E_A|^2$ and $|E_{B0}|^2$ on the grating surface radiated from input and central output fibres, respectively, are shown in Fig. 5.7. This numerical simulation

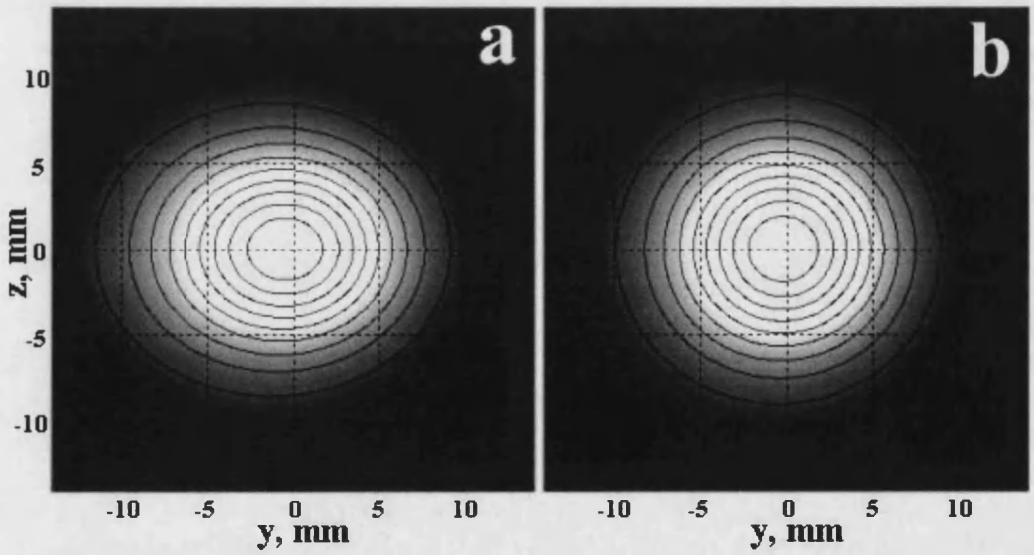

Fig. 5.7. **The intensity patterns and isophotes on the grating surface from input (a) and output (b) fibers.**

clearly demonstrates the effect of the fibre mode compression, described in a section 5.5.3.

The transmission spectrum and its central part were calculated as an overlap integral using Eq (5.12) for the central output fibre and are shown in Fig. 5.8a and b, correspondingly. The experimental passbands of the demultiplexer for six different gratings

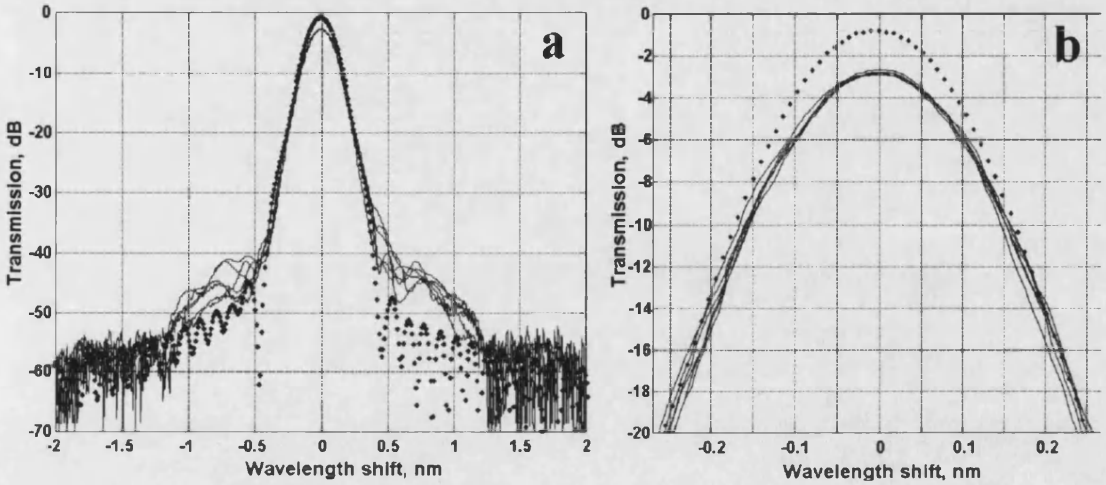

Fig. 5.8. **Theoretical (dotted line) and experimental (solid lines) passband of demultiplexer (a), and its central part (b).**

are also shown for comparison. The measurements were carried out using an unpolarized broadband light source. The shape of the calculated passband is in a good agreement with the experiment over the bandwidth of ±0.35 nm, and up to the level of –30 dB. The moderate increase of side slopes for experimental curves can be explained by the inaccuracy in the recording scheme alignment, resulting in additional spherical aberration. 0.8 dB theoretical coupling loss at the top of a passband can be directly related to the residual aberrations of the holographic grating. The experimental transmission at the central wavelength is about 2 dB lower compared to theoretical one. The main contribution to this difference is due to the grating diffraction efficiency (1.7 dB), and remainder of 0.3 dB can be accounted for the fibre connector losses.

For a more accurate analysis of the transmission spectrum the integral in Eq (5.12) should be calculated separately for the S- and P-polarizations. Moreover, the amplitude E_A must be substituted by $E_A\sqrt{\kappa(y,z)}$, where $\kappa(y,z)$ is the diffraction efficiency at a given point on the concave grating.

5.7 Multimode interference coupler for passband flattening

The pseudo parabolic top of the demultiplexer transmission spectrum shown in Fig. 5.8 is clearly a shortcoming. The resultant 0.5 dB bandwidth of 0.08 nm limits the signal bit rate and requires the accurate control of the transmitted wavelength. Ideally, one would like the passband to be a rectangular function, which is unrealizable [11], and several techniques have been proposed to produce suitable approximations [12]-[14]. In this work a method of passband flattening based on the use of multimode interference coupler (MMI) [15] was chosen for the designed demultiplexer.

The main idea behind this method is to reshape the profile of the light spot launched into the output fibre. The passband of the demultiplexer can be calculated as an overlap integral between the fibre mode ψ and reshaped field ψ' at the output plane (y_{BJ},z_{BJ}), shown in Fig. 5.6. The transmission function for the J-th channel of aberration-free system is given, in the wavelength domain, by

$$\eta(\lambda-\lambda_J)=\left|\iint\psi(y_{BJ},z_{BJ})\psi'[y_{BJ}-(\lambda-\lambda_J)D_L,z_{BJ}]dy_{BJ}dz_{BJ}\right|^2, \qquad (5.16)$$

where D_L is the linear dispersion from (5.2), and $\iint|\psi(y,z)|^2dydz=\iint|\psi'(y,z)|^2dydz=1$. An acceptable compromise between the band-centre flatness and the edge steepness is

provided by a reshaped field function that is described by the sum of two shifted fibre modes, separated in the dispersion plane by some distance Δ:

$$\psi'(y,z) = \psi(y - \Delta/2, z) + \psi(y + \Delta/2, z). \qquad (5.17)$$

Generally a flat-top passband corresponds to 60% dip between the two peaks of the intensity profile $|\psi'|^2$. This method of flattening introduces insertion loss due to the mismatch between the "camel-like" reshaped field and the fibre mode.

Such "camel-like" field may be generated by a centre-fed multimode interference coupler (MMI). MMI filters ensure the predictable evolution of the modes within a multi-mode waveguide, as illustrated in Fig.5.9. Soldano and Pennings [16] have demonstrated

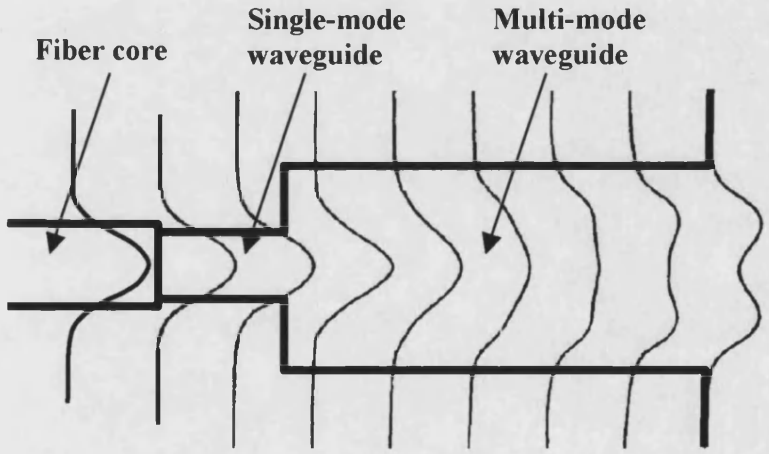

Fig. 5.9. **Mode evolution in the imaging MMI**

that the envelope of the field profile for MMI develops a number of symmetric self-images of the input field at fixed distances along the multi-mode waveguide. In particular, the field, as it propagates along the waveguide initially spreads out and flattens, but then sharpens into peaks. The multi-mode waveguide can then be 'diced' at the point where the "camel-shaped" image is disposed symmetrically about a centre line with peaks occurring at approximately ¼ and ¾ of the waveguide width.

The silica-based MMI on a silicon wafer was designed by BBV Design & Software (The Netherlands) and produced by IONAS (Denmark). The refractive index contrast is 0.7%, the thickness of waveguide core is 7 μm, the length of multi-mode waveguide is 380 μm, and core widths of single- and multi-mode waveguide are 7 and 21 μm, respectively. The wafer with the MMI was diced and polished on both sides and pigtailed to the input fibre, the output facet was anti-reflection coated. The image of the MMI output facet is shown in Fig.5.10. The coupling loss due to the mode mismatch between fibre and single-mode waveguide is approximately 0.3 dB, MMI propagation loss is 0.2 dB, and flattening penalty is 2.1-2.2 dB.

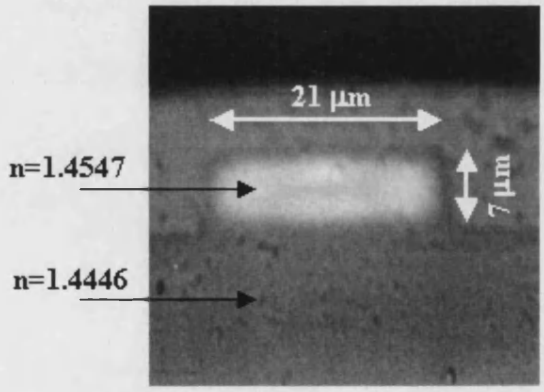

Fig. 5.10. **Microscope image of the output facet of MMI viewed with visible light.**

A data array describing the expected MMI field ψ' was supplied by BBV, and the amplitude created by the MMI on the grating surface was calculated from equation (5.15) with ψ' instead of ψ. The theoretical intensity profiles of the light beam from the MMI at the output facet and on a grating surface are shown in Fig. 5.11a and b, correspondingly.

The passband of an aberration-free demultiplexer, from Eqn. (5.16), is shown by the solid line in Fig. 5.12. The loss due to flattening is 2.2 dB, and 0.5 dB bandwidth is 0.34 nm. The transmission spectrum for the central channel of the designed demultiplexer with

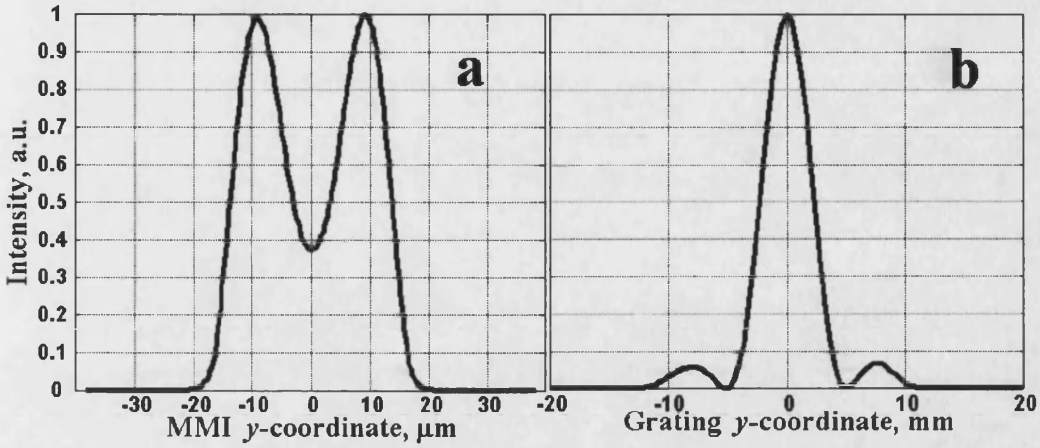

Fig. 5.11. **Intensity profiles of the light beam from MMI at the output facet (a), and on the grating surface (b).**

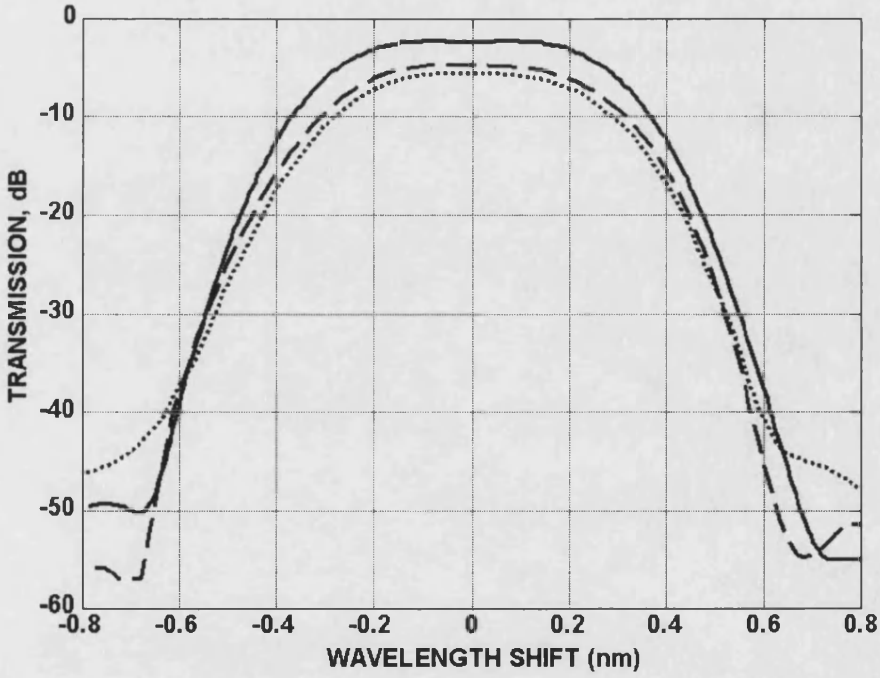

Fig. 5.12. **Passband of demultiplexer with MMI. Ideal case (solid line), real device simulation (dashed curve) and experiment (dotted curve).**

the MMI, calculated from (5.12) (dashed line) results in 4.7 dB loss (including -1.7 dB diffraction efficiency) and 0.26 nm of 0.5 dB bandwidth. The experimentally measured passband of the demultiplexer with losses of 5.5 dB and bandwidth of 0.24 nm is shown by the dotted line. The shape of the calculated passband is in a good agreement with

experiment up to the level of –32 dB from the minimum loss. About a 10 dB increase in the side slopes was explained in section 5.6. An additional loss of 0.8 dB measured in the experiment can be accounted for as follows: 0.3 dB fibre/waveguide mode mismatch; 0.2 dB MMI propagation; 0.3 dB fibre connectors and others. Finally, the use of MMI resulted in a factor of 3 bandwidth increase at the expense of 2.7 dB additional loss (as can be seen from the experimental results in Fig. 5.8 and Fig. 5.12).

5.8 Adjustment and fixing

Before the assembly procedure the concave grating was glued to the housing with thermo-epoxy in an oven. Then the housing with grating was fixed on the optical bench. The input MMI and output fibres array were mounted on six-axis positioners. The light from an unpolarized broadband (1500-1650 nm) source was fed to the input MMI. The first, the central, and the last output fibres, corresponding to channel wavelengths 1527.216, 1546,119 and 1565.496 nm, were connected to ANDO spectrum analyzers. The main experimental adjustment steps were as follows:

1) Approximately mount all elements in their designed positions.

2) Centre the input MMI and central output fibre radiation diagrams relative to the grating vertex. At this stage both the MMI and central output fibre are fed from the broadband light source.

3) Adjustment of the output fibre array to maximise the coupling efficiency into the central fibre at λ=1546.119 nm.

4) Move MMI and fibres array in the opposite directions, perpendicular to dispersion plane, to maximize the coupling into the central fibre. This ensured that the MMI and central output fibres lay in the dispersion plane.

5) Rotate the fibre array around the axis of the central fibre and move it perpendicular to dispersion plane to obtain simultaneously the maximum coupling into the central and the edge fibres. At this step the wavelengths for edge fibres are not adjusted. This guaranteed that all output fibres are in the dispersion plane.

6) Vary the position of the MMI in the dispersion plane, and repeat point 3) to determine the absolute maximum coupling into the central fibre. This ensured that the MMI and central output fibre are very close to designed positions.

7) Move the fibre array to (or from) the grating along the line BO, shown in Fig. 5.3, and compensate for the defocus by a displacing the MMI from (or to) the grating along the line AO to centre the transmission spectra of the three output fibres, relative to the channel wavelengths. This is necessary to obtain the required linear dispersion.

After the described procedure the input MMI was prefixed in the housing using UV epoxy. Then thermo-epoxy was injected between the housing and the MMI and cured in the oven. After that the housing with the concave grating and MMI was again fixed on the optical bench, and the array of the output fibres was aligned separately, as described in the points 3), 5), and 7). Then the fibre array was glued to the housing in the same way as with the MMI.

Separate fixing of the MMI and fibre array allow a potential increase of the yield. This is because possible misalignments of MMI after curing can be compensated for by minor readjustment of the output fibres.

5.9 Tolerances

To determine all the possible tolerances, 3 criteria were established, so that any admissible misalignment or imperfection should not result in:

1) Additional losses higher than 0.3 dB

2) Decrease of 0.5 dB bandwidth by more than 0.01 nm

3) Decentring of the passband relative to the channel wavelength by more than 0.02 nm

The first two criteria are conditional, whilst the third one can be explained as follows. To transmit the signal with the bit rate of 10 Gb/s, a spectral window of 0.16 nm is required, so that useful margins on each side of 0.24 nm of 0.5 dB- bandwidth is 0.04 nm. The channel wavelength drift is assumed to be within ±0.02 nm, and therefore, the residual tolerances for any possible misalignments are also ±0.02 nm, corresponding to the source (or image) shift in the dispersion direction of ±1 μm. The third criterion defines the desired accuracy of linear dispersion as $\delta D_L=(\pm 1\ \mu m/W_A)\cdot D_L=\pm 0.052\ \mu m/nm$, where $W_A=960\ \mu m$ is a half-width of the output fibres array. This also implies that defocus of the fibre array should not exceed the value of $(\pm 1\ \mu m/W_A)r_{\beta 0}=\pm 92\ \mu m$.

5.9.1 Clearance window for the MMI position

The clearance window defines how accurately the MMI should be fixed within the demultiplexer housing. Firstly, this requires the calculation of the tolerances for angular misalignments of the MMI. The rotation of the MMI around its axis of symmetry results in a reduction of the 0.5 dB- bandwidth, as shown in Fig. 5.13a. The tolerances at this angle are defined from the above criterion 2 as ±10°, which is very loose. The tilt of the MMI in the dispersion plane results in a moderate broadening of the bandwidth but introduces a

substantial loss, as shown in Fig. 5.13b. According to the criterion 1 this tilt must not exceed ±0.7°. The acceptable tilt of MMI axis relative to the dispersion plane is defined

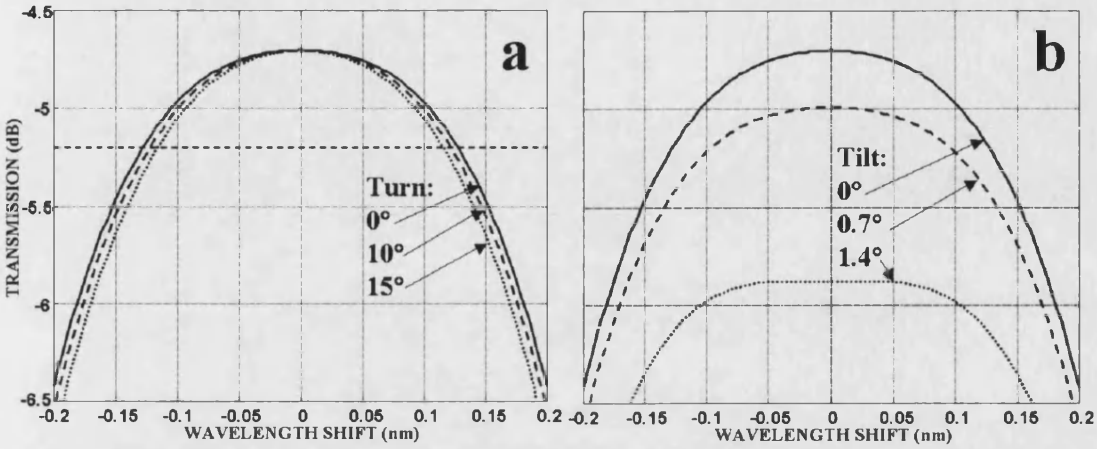

Fig. 5.13. **Numerical simulation for the effects of MMI rotation around its axis of symmetry (a), and the tilt of MMI in the dispersion plane (b).**

from criterion 1 and Equation (5.6) (L_{ang}=0.3 dB) as ±1.5°. Rectilinear misalignments of the MMI are compensated for, to some extent, by readjustments in the position of the output fibre array. The admissible deviation from the dispersion plane and the transverse shift in dispersion direction were determined experimentally, according to criterion 1, as ±89 μm and ±58 μm, respectively. The defocus of the MMI according to criterion 1 was experimentally compensated for by the opposite defocus of the fibre array up to ±120 μm, but the third criterion in this case imposes stronger restrictions of ±92 μm. The described clearances for the input MMI array position are shown in Fig. 5.14 for lucidity.

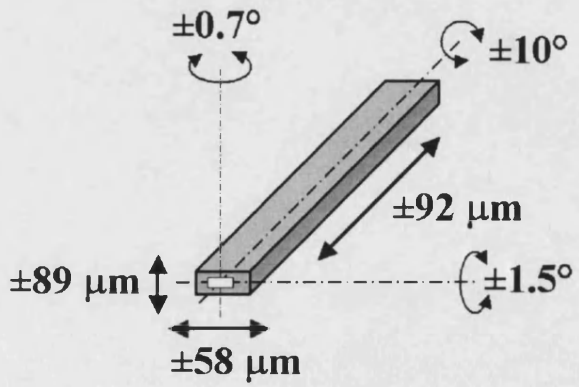

Fig. 5.14. **Clearances for MMI fixing.**

5.9.2 Tolerances for the alignment of the output fibre array

As described in section 5.8, the fibre array is fixed at the last moment and tolerances for its alignment are very tight. The admissible misalignments of the output fibres in the dispersion direction are directly determined by the criterion 3 as δU_D=±1 μm. For the definition of other types of misalignments the first criterion was used. The allowable tolerances for defocus and deviation from the dispersion plane were studied experimentally. As shown in Fig. 5.15, 0.3 dB additional losses correspond to a defocus

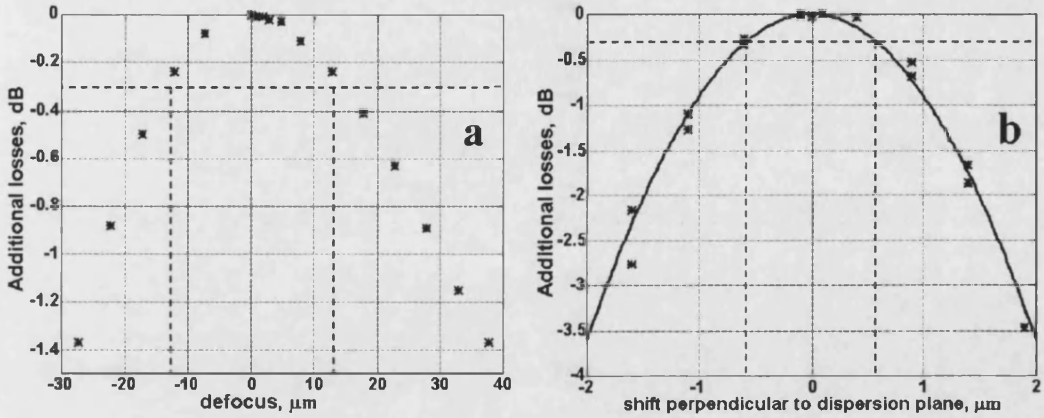

Fig. 5.15. **Additional losses due to misalignments of fiber array: defocus (a), and the deviation from the dispersion plane (b).**

δU_F=±12 μm and a deviation from the dispersion plane δU_P=±0.6 μm. The admissible tilt $\delta\theta_D$ of the output fibres array around the axis of the central fibre is defined by δU_P so that the first and last fibres are within ±0.6 μm of the dispersion plane. The half-width of the fibre array is W_A=960 μm, so that $\delta\theta_D$=atan($\delta U_P/W_A$)= ±0.036°. Tolerances for the rotation of the fibre array in dispersion plane are defined by the resulting defocus of the end fibres and can be determined as $\delta\theta_F$=atan($\delta U_F/W_A$)= ±0.72°. The admissible tilt around the line crossing the facets of the output fibres is determined from Equation (5.6) as $\delta\theta_P$=±1.5°. All

the described tolerances for the output fibre array position are shown in Fig. 5.16 for clarity.

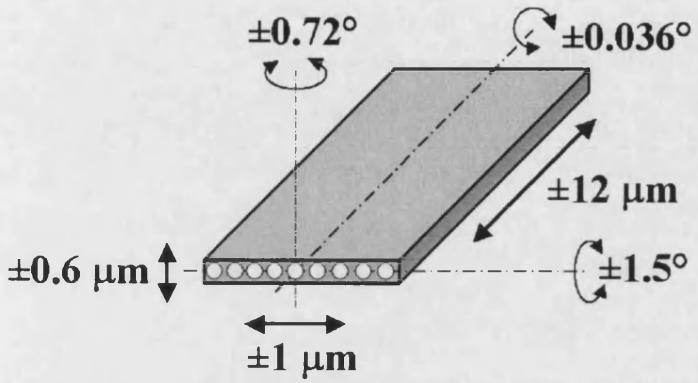

Fig. 5.16. **Tolerances for position of output fiber array.**

5.9.3 Concave grating accuracy requirements

Finally, we must determine the fabrication tolerances for the only optical element used in the demultiplexer, namely the concave surface quality and the accuracies in the adjustment of the holographic recording scheme.

The acceptable deviation from sphericity of less than 0.1 μm ($\lambda/15$ for our spectral range) is not problematic for commercially available concave optical surfaces. The most difficult is to guarantee the strict limits on the value of the grating curvature radius. Typically, the radius relative accuracy $\delta R/R$ varies in the range of 0.1% (Oriel Instruments) to 1% (Melles Griot). The tolerances for the radius of curvature were determined from the first criterion. For a chosen value δR, MATLAB simulation program varied the input MMI position parameters $r_{\alpha 0}, \alpha_0$ to maximize the merit function $MF = \min[\eta_{-24}(\lambda_{-24}), \eta_0(\lambda_0), \eta_{24}(\lambda_{24})]$, where $\eta_J(\lambda_J)$ is the coupling efficiency at a wavelength λ_J into the J-th output fibre. The coupling efficiencies were calculated from (5.12), the channel wavelengths λ_J and relative positions of output fibres were defined in

section 5.5.4. For each iteration the angular position β_0 of the central output fibre was determined by equating to zero the first expansion term of the wave aberration [6] as

$$\sin\beta_0 = -\sin\alpha_0 + \frac{\lambda_0}{\lambda_H}(\sin\gamma - \sin\delta),$$

where all the notations are from section 5.5.1. The distance $r_{\beta 0}$ from the central fibre to the grating vertex was defined from (5.2) as

$$r_{\beta 0} = \frac{D_L \lambda_0 \cos\beta_0}{\sin\alpha_0 + \sin\beta_0},$$

where D_L=0.05 mm/nm is the design linear dispersion. The fibre array was always oriented so that the chief ray at the central wavelength was normal to the facets of the output fibres. Less than 0.3 dB decrease of the merit function compared to the initial value for R=86.5206 mm corresponds to -0.3 mm < δR < 0.44 mm.

Parameter	Designed value	Tolerances
Curvature radius (mm)	**86.5206**	**+0.44 -0.30**
First point source angle	**61.17258°**	**+0.028° -0.040°**
First point source distance (mm)	**151.2318**	**+0.040 -0.024**
Second point source angle	**38.65402°**	**+0.020° -0.012°**
Second point source distance (mm)	**107.4626**	**+0.028 -0.040**
Recording wavelength (nm)	**457.935**	

Table 5.1. Tolerances on the fabrication of concave holographic grating

The tolerances on each of the recording scheme parameters were determined separately using the same algorithm and are given in Table 5.1. The recording wavelength from an Ar-laser is generally defined with a relative accuracy of 10^{-6} and does not require tolerance definition.

5.10 Environmental stability

An extremely important factor influencing the design of any optomechanical system is the environment to which that system is to be exposed during its lifetime [17]. Especially tough requirements are imposed on optical telecommunication devices with a lifetime of 25 years, and all devices must be subjected to a series of special tests without performance degradation. Typical reliability tests are: mechanical shock (5 times in 6 directions with acceleration of 500 G); vibration (from 20 to 2000 Hz with acceleration of 20 G, for 16 minutes along each axis); high and low temperature storage (2,000 hrs at 85°C and -40°C in dry atmosphere); thermal shock (several replacements from one thermostat to another with the temperature difference of 100 °C); damp heat (500 hrs at 85°C and 85% relative humidity); thermo-cycling (100 cycles from -40°C to 70°C with a rate of 2°C /min). Detailed description of the reliability testing results is beyond the subject of this thesis, however, it should be noted that after a few redesigns of the housing and fixing techniques, the required reliability was achieved.

In this section we describe, in detail, how the optical misalignments due to thermal expansion and change of the air refractive index, when the demultiplexer is operating in different environments, can be avoided.

5.10.1 Thermal expansion and materials

Temperature is perhaps the most critical of environmental parameters. For the fabrication of a truly passive athermal demultiplexer operating over a wide temperature range, materials with an extremely low *CTE* (coefficient of thermal expansion) are required. Among all the possible material candidates, only ULE glass (ultra-low-expansion glass, CTE=0.03x10^{-6}/°C, Corning Corporation) and Zerodur (CTE=0.10x10^{-6}/°C, Schott Corporation) are reasonably well characterized in refereed technical literature [18]. ULE is fused silica glass doped with 7% titanium silicate. This material was used for the grating substrate due to its good adhesion to photoresist. Zerodur is described as a glass ceramic, consisting of a crystalline and glassy phases. This substance was chosen for the demultiplexer housing, shown in Fig. 5.17a, because of easier mechanical processing.

The main misalignments due to the thermal expansion are the defocus, as a result of uniform housing increase, and the image (or wavelength) shift, because of the variation in the grating period.

The defocus due to a temperature difference ΔT is $\delta U_F = 2r_{\beta 0} CTE \cdot \Delta T$ where $r_{\beta 0}$ is the distance from concave grating to the central output fibre. For the Zerodur housing ΔT=60°C results in δU_F=1.04 μm. For comparison, an invar holder (CTE=1.2x10^{-6}/°C) gives δU_F=12.5 μm, which is outside the tolerances described in section 5.9.2.

A thin (about 0.5 μm) layer of photoresist deposited on the grating is sufficiently elastic, so that thermal variations in a grating period are completely defined by the substrate properties. The shift of the focused spot in the dispersion direction at the output fibre facet due to thermal expansion can be estimated. Using the formula for the diffraction angle $\beta = \arcsin(\lambda/d - \sin\alpha_0)$ [7], it can be easily shown, that variation of $-\delta d$ in the groove period gives the angle variation of $\delta\beta = \delta d \cdot \lambda/(d^2 \cos\beta_0) \approx 0.88\,\delta d/d$. Therefore, the spot shift in the dispersion direction is $\delta U_D = r_{\beta 0}\delta\beta = 0.88 r_{\beta 0} CTE \cdot \Delta T$. For the ULE glass ΔT=60°C results in

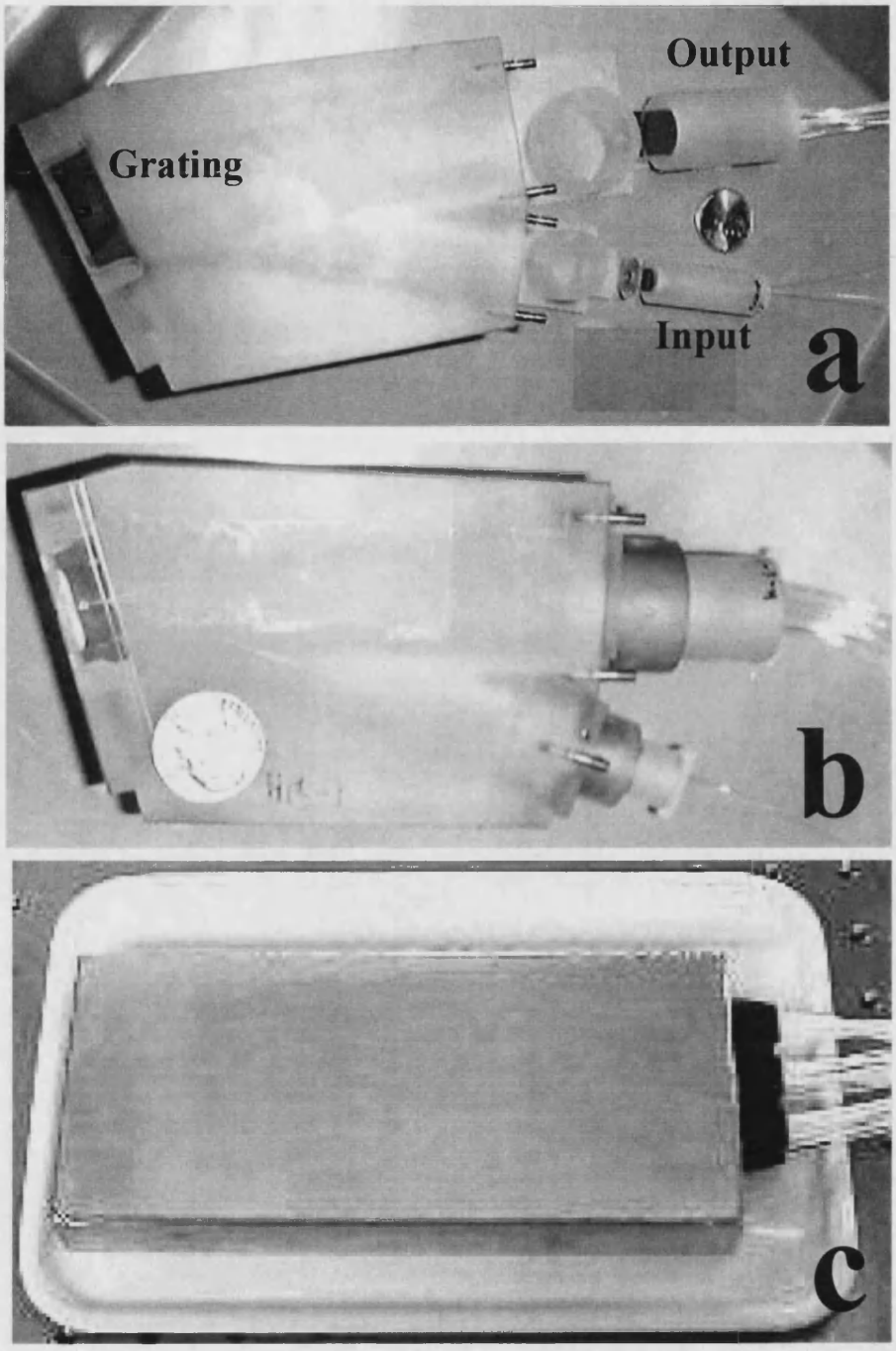

Fig.5.17. **Demultiplexer: components (a), assembled (b), hermetically sealed (c).**

δU_D=0.14 μm. For comparison, a fused silica substrate (CTE=0.51x10^{-6}/°C) gives δU_D=2.4 μm which is far outside the tolerances of ±1 μm.

Finally, the expansion of the output fibre array fabricated on the silicon wafer with CTE=2.0x10^{-6}/°C must be assessed. The distance between the first and the last fibre of 1920 μm varies by only 0.23 μm due to temperature variation of 60°C. Therefore, all possible thermal misalignments are much less than the established tolerances.

5.10.2 Refractive index of air, hermetic sealing

The diffraction angle at the grating, and therefore the position of focused light spot for a given channel, is determined by the wavelength in air

$$\lambda_A=\lambda_V/n_A, \qquad (5.18)$$

where λ_V is the wavelength of light in vacuum, and n_A is the refractive index of air.

At optical frequencies the refractive index of dry air is given [19] by

$$n_A=1+[\ 77.6\text{x}10^{-6}+0.5836/(\lambda_V)^2\ ]\ P/T_K, \qquad (5.19)$$

where λ_V is the wavelength in nanometres, P is the atmospheric pressure in millibars, and T_K is the temperature in Kelvin scale. The refractive index of air can vary from 1.00016 to 1.00034 for environmental conditions -20°<T_C<70° and 700mbar<P<1100mbar. The effects of humidity results in wavelength variations of less than ±1.5 pm [20] and may generally be neglected, except that it would be essential to avoid water condensing on the demultiplexer optics.

Assuming that the device was assembled and fixed at P=1000 mbar and T_C = 20°C, and considering the channel frequency 193900 GHz corresponding to λ_V =1546.119 nm, Equations (5.18) and (5.19) give λ_A =1545.709 nm. Standard permissible variations from

the assembly conditions δT_C = 32°C or δP=-100 mbar result in a wavelength shift in air of $\delta\lambda_A$ =0.04 nm, which is outside the criterion 3 from section 5.9.

On the other hand, in a sealed volume the ratio P/T_K is reasonably constant, so that the refractive index does not depend on the external environment. This implies that the optical scheme of demultiplexer should be hermetically sealed. For this purpose the ZERODUR housing with optical scheme was placed in a soldered stainless steel housing as shown in Fig.5.17c. The input and output fibres were centre-stripped of plastic jacket, gold-coated, fed through the holes and hermetically soldered to the box, as described in [21].

The wavelength shift due to the temperature change from 5°C to 65°C was studied experimentally at a constant pressure of 1005 mbar for an open and hermetically sealed demultiplexer. The device was placed into an oven/refrigerator, the broadband light source

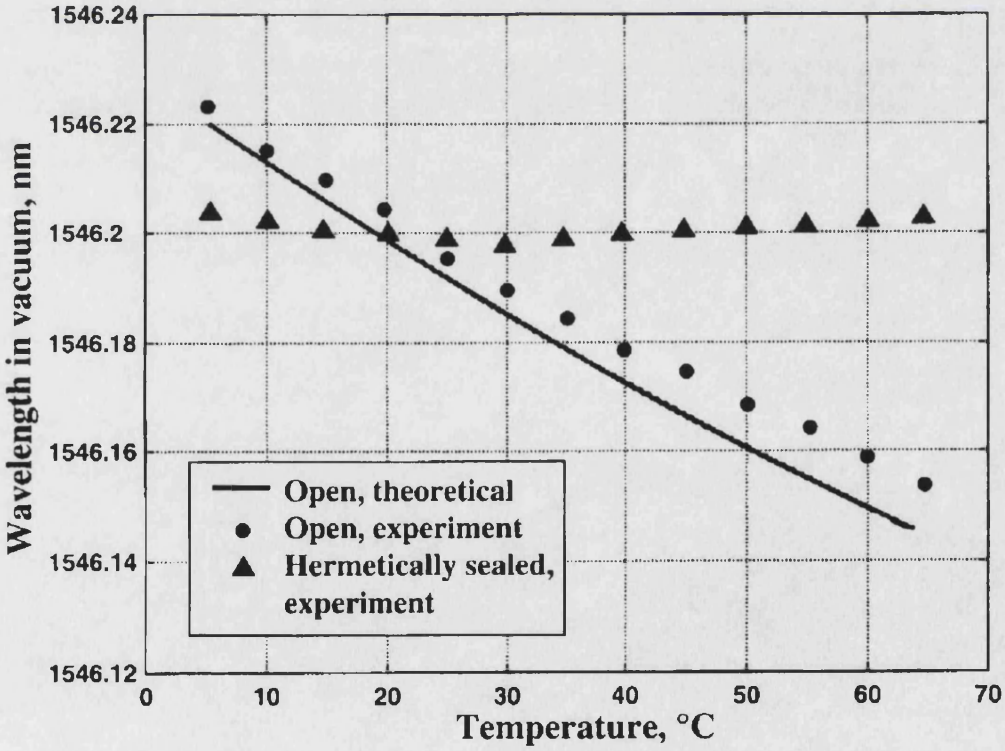

Fig.5.18. **Wavelength as a function of temperature for the open and hermetically sealed demultiplexer.**

was coupled into the input MMI and the signal from the central output fibre was analysed using an optical spectrum analyzer. Fig.5.18 shows the wavelength at which minimum optical losses were measured, as a function of temperature for the open (theory and experiment) and hermetically sealed (experiment) demultiplexer. The hermetic housing allows a dramatic reduction in the wavelength variations. The residual drift within ±4 pm corresponds to the image shift of 0.2 μm and can be explained by small deformations of ZERODUR holder.

5.11 Performance characteristics

The performance characteristics of each channel were experimentally investigated in detail after the demultiplexer was assembled and hermetically sealed. The transmission spectra of all 49 channels of demultiplexer with the MMI input at 24°C were measured and are shown in Fig. 5.19a. The enlarged part of this plot for 7 channels is shown in Fig. 5.19b.

The numerical processing of these data reveals that the insertion losses are within 5.3-5.8 dB, the adjacent channels crosstalk does not exceed –38 dB, and background crosstalk is less than -49 dB. The variations in the measured bandwidth from channel to channel are shown in Fig. 5.20. The minimum bandwidth at 0.5- and 1 dB-levels is 0.24 and 0.32 nm, correspondingly. Fig. 5.21 shows the excursion of the central passband wavelength for each channel, relative to the International Telecommunications Union (ITU) grid. The systematic excursion, shown by a dashed straight line can be related to the residual misalignment of the demultiplexer, whilst the random fluctuations around this line are mostly due to errors in the positions of the output fibres in the V-groove array.

Similar measurements have been carried out with demultiplexer placed into the oven/refrigerator and thermo-cycled during 10 days within an operating range from -5 to

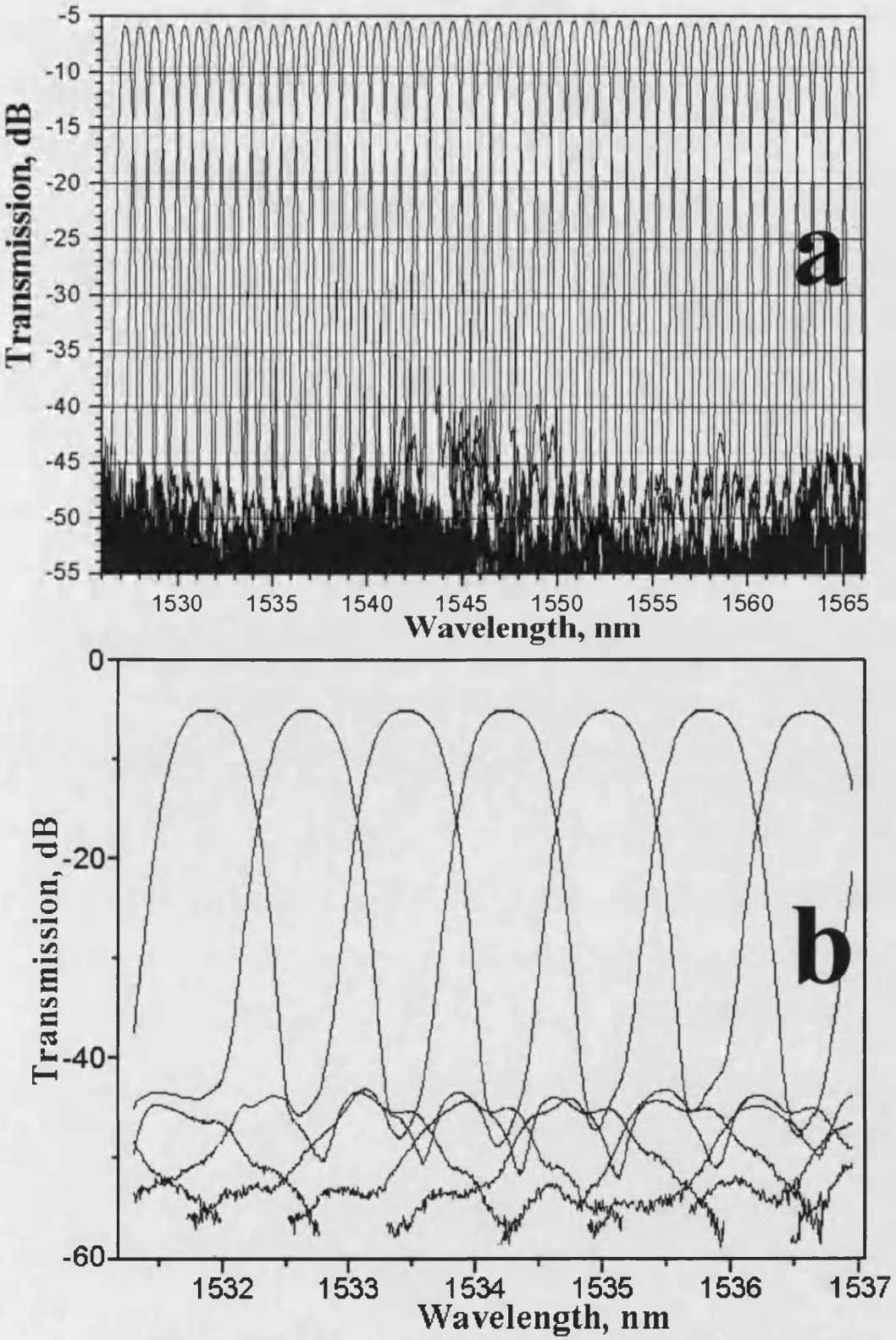

Fig.5.19. **Transmission spectra of demultiplexer. All channels (a), and 7 adjacent channels (b)**

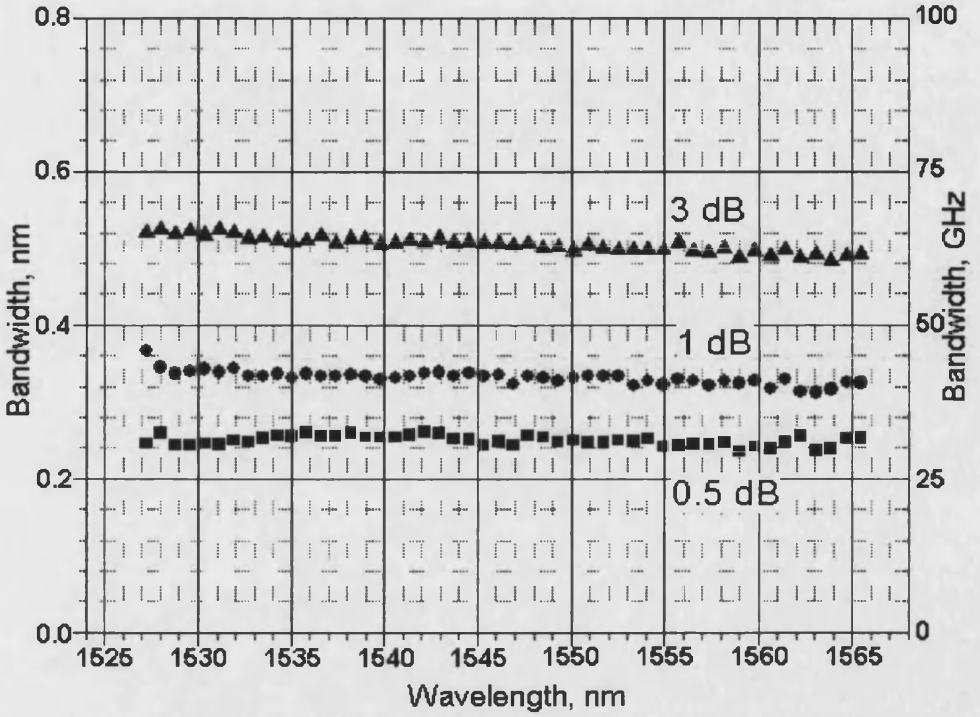

Fig.5.20. **Bandwidth of all channels, measured at a different levels**

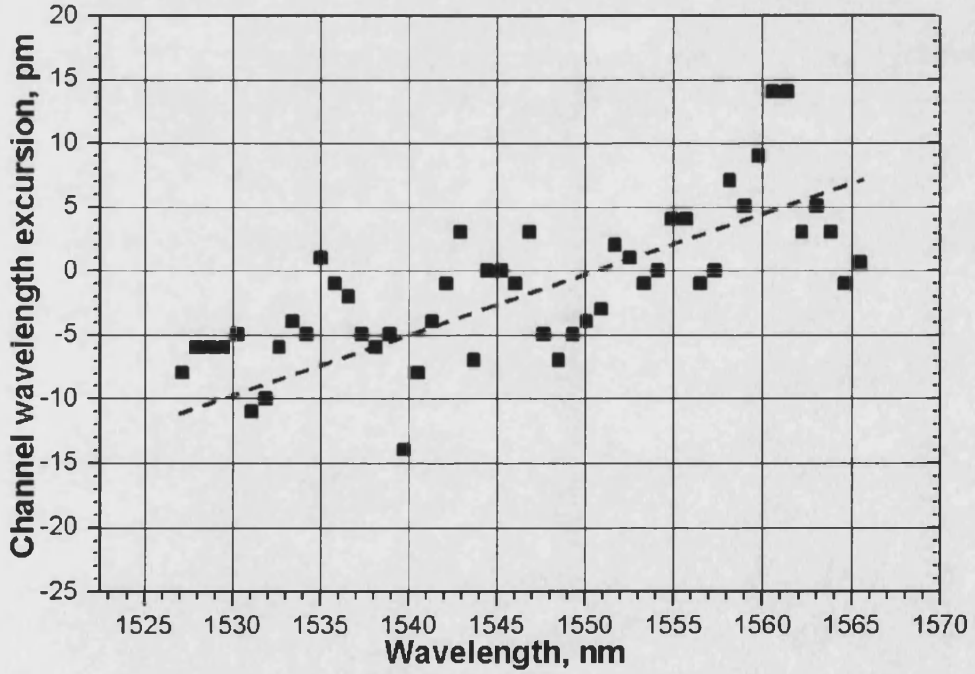

Fig.5.21. **The excursion of channels' wavelengths with respect to ITU grid**

+65°C. The resultant summary of these performance characteristics is shown in Table 2, in comparison with a recently developed free-space plane grating demultiplexer MICS-40/100 [22, 23] from Nettest Inc.

Specifications	MICS-40/100	Concave grating
Number of channels	40	49
Channel spacing	100 GHz	100 GHz
Channel center accuracy	±50 pm	±15 pm
0.5 dB bandwidth	?	0.24 nm
1 dB bandwidth	0.22 nm	0.32 nm
Insertion loss	<5.5 dB	<5.8 dB
Insertion loss uniformity	±0.5 dB	±0.25 dB
PDL	<0.4 dB	<0.4 dB
Adjacent channel crosstalk	<-30 dB	<-38 dB
Cumulative crosstalk	<-23 dB	<-30 dB
Operating temperature range	-10 to +65°C	-5 to +65°C *
Wavelength temperature variations	±48 pm	±18 pm
Insertion loss temperature dependence	±0.5 dB	±0.2 dB
Dimensions	148x26x68 mm^3	140x24x65 mm^3

Table 5.2. Specifications for Nettest MICS-40/100 and concave grating demultiplexers. * range tested.

5.12 Conclusions

This chapter described the main stages and details in the design of a free-space concave holographic grating-based demultiplexer. First, the requirements to the optical scheme were formulated to obtain the optimal performance. It was shown that these requirements define the concave grating mount with very small margins.

The period of the grating was chosen to provide PDL<0.4 dB and a diffraction efficiency of nearly 68% within the operating spectral range. The developed procedure for the simultaneous optimization of the holographic recording scheme and the grating mount is described in detail. The choice of 40 μm spacing between the output fibres resulted in low crosstalk levels and reasonable device dimensions. The coupling losses due to the fibre

mode mismatch and tilted incidence were shown to be negligible compared to the diffraction efficiency losses. The method developed for the accurate calculation of a passband for each demultiplexer channel was shown to be in excellent agreement with the experimentally measured data. The use of the multimode interference coupler at the input of the demultiplexer resulted in a factor of 3 bandwidth increase at the expense of 2.7 dB additional loss. The developed sequence in the adjustment and fixing procedure is described and the tolerance analysis for the fabrication of the concave grating and fixing of the demultiplexer parts is presented. The analysis of the temperature misalignments and behaviour of the air refractive index demonstrated the necessity to use ultra low thermal expansion housing and hermetic sealing to achieve an athermal device.

A complete, fully packaged free-space concave grating demultiplexer was demonstrated for the first time. This truly passive athermal device does not need a thermo-electric cooler (TEC) nor active temperature control, which greatly improves its reliability. The data shown it Table 2 demonstrate that the only optical element (concave grating) instead of five elements in MICS-40/100 demultiplexer [22] can achieve demultiplexer performance with substantially improved characteristics.

Eleven devices were assembled and fixed in Zerodur housing; three of them were hermetically sealed. The project was closed in March 2001 due to the crisis in the telecommunications industry.

References to Chapter 5

[1] D. Maystre, M. Neviere, and R. Petit. In *Electromagnetic Theory of Gratings* (R. Petit, ed.), pp.159-209. Springer-Verlag, Berlin and New York, 1980.

[2] M. C. Hutley, "Blazed interference diffraction grating for the ultra-violet" *Optica Acta*, vol.22, 1975 pp.1-13.

[3] M. C. Hutley, *Sci. Prog. (Oxford)*, vol.61, 1974, p.301-305.

[4] E.G. Loewen, M. Neviere, and D. Maystre, " Grating efficiency theory as it applies to blazed and holographic gratings", *Applied Optics*, vol.16, 1977, pp.2711-2721.

[5] J. Hegarty, S. D. Poulsen, K. A. Tackson and P. Raminov, "Low-loss single-mode wavelength division multiplexer with etched fibre array", *IEE Electronics Letters*, vol.20, 1984, p.685-686.

[6] M.P.Chrisp, "Aberration-Corrected Holographic Gratings and Their Mountings", in *Applied Optics and Optical Engineering*, R.R.Shannon and J.C.Wyant, eds. (Academic, London, 1987), vol.10, pp.391-454.

[7] M. Born, and E. Wolf, Principles of Optics.1970, Pergamon Press, London.

[8] D. Marcuse, "Loss analysis of single-mode fiber splices", *Bell System Technical Journal*, vol.56, 1977, pp.703-718.

[9] E. G. Churin, P. Bayvel, "Design of free-space WDM router based on holographic concave grating", *IEEE Photon. Technol. Lett.*, vol.11, 1999, pp.221-223.

[10] R. E. Wagner, and W. J. Tomlinson, "Coupling efficiency of optics in single-mode fibre components," *Applied Optics*, vol.21, 1982, pp. 2671-2688.

[11] K. Okamoto and H. Yamada, "Arrayed-waveguide grating multiplexer with flat response," *Optics Letters*, vol.20, 1995, pp.43-45.

[12] C. Dragone, T. Strasser, G. A. Bogert, L. W. Stulz, and P. Chou, "Waveguide grating router with maximally flat passband produced by spatial filtering", *IEE Electronics Letters*, vol.33, 1997, pp. 312-314.

[13] Y. P. Ho, H. Li, and Y. Chen, "Flat channel-passband-wavelength multiplexing and demultiplexing devices by multiple-Rowland-circle design," *IEEE Photon. Technol. Lett.*, vol.9, 1997, pp.342-344.

[14] A. Rigny, A. Bruno, and H. Sik, "Multigrating method for flattened spectral response wavelength multi/demultiplexers", *IEE Electronics Letters*, vol.33, 1997, pp. 1701-1702.

[15] M. R. Amersfoort, J. B. D. Soole, H. P. LeBlance, N. C. Andreadakis, A. Rajhel, and C. Caneau, "Passband broadening of integrated arrayed waveguide filters using multimode interference couplers," *IEE Electronics Letters*, vol.23, 1996, pp. 449-451.

[16] L. B. Soldano and E. C. M. Pennings, "Optical multi-mode interference devices based on self-imaging: Principles and applications," *J. Lightwave Technol.*, vol.13, 1995, pp.615-627.

[17] P. R. Yoder, *Opto-mechanical system design*, Marcel Dekker, New York, 1993.

[18] W. P. Barnes, "Optical Materials – Reflective", in *Applied Optics and Optical Engineering*, Vol. VII, Ghap.4 (R. R. Shannon and J. C. Wyant, eds), Academic Press, New York, 1979.

[19] B. Elden, "The refractive Index of Air," *Metrologia*, vol.2, 1966, pp.71-80.

[20] D. Derickson, *Fiber Optic Test and Measurement.* Prentice Hall RTR, New Jersey, 1998.

[21] E. Suhir, C. Paola and W. M. Macdonald, "Input/Output Fiber Configuration in a laser package Design", *J. Lightwave Technol.*, vol.11, 1993, p. 2087-2097.

[22] P. Martin, E. Taufflieb, B. Laloux, and H.C. Lefevre, "Optimized bulk-optic grating approach for D-WDW demultiplexers", *Proc. ECOC 1999*, vol.2, pp.110-111.

[23] www.photonetics.com/products/pdf/mics.pdf, 2001

Chapter 6

Design of the wavelength router

6.1 Introduction

As already mentioned in Chapter 2, the greatest advantage of WDM is achieved by implementing wavelength routing [1] of high-capacity optical signals according to their wavelength, without optoelectronic conversion or processing [2]. This provides the network node-pairs with end-to-end optical channels, known as lightpaths [3], resulting in protocol transparency [4] and simplified management and processing compared to routing in systems using digital cross-connects [5]. Optical routers with a large number of ports (>32) have emerged as key elements for wavelength routing, provisioning and restoration in future WDM networks.

The main problem with wavelength routers, compared to conventional demultiplexers, is the coherent crosstalk arising from the same wavelength re-use within different ports. This implies strict limitations on the amount of stray light and restricts the number of interconnected users. Free-space optics provides significantly better crosstalk performance than integrated optics devices [6] and is more expedient for the realization of high-capacity routers.

Another problem, associated with wavelength routers, based on bulk or arrayed waveguide gratings, is that they cannot use the standard ITU grid with constant frequency separation when operating with large ports counts [7]. Probably, the constant carrier frequency pitch for the WDM networks is historically based on frequency periodic transmission properties of the commonly used Fabry-Perot etalon. However, for the router

operation input channels are equally spaced in wavelength, rather than frequency. This is due to the intrinsic diffraction properties of the grating. The well-known relation between the sine of the incidence angle α and the sine of diffraction angle β is linear in wavelength λ and inversely proportional in frequency

$$\nu.\sin\alpha+\sin\beta=\lambda/b=c/(\nu b), \quad (6.1),$$

where c is the velocity of light. This permits the set of equally spaced wavelengths successfully to interconnect all input and output fibres.

As already discussed, concave grating-based free-space devices are particularly attractive, since a single optical element performs both dispersive and focusing functions, and that holographic gratings, fundamentally, contribute significantly less scattered light compared to ruled gratings [8], and therefore, are preferable from the crosstalk point of view [9]. The concave grating mount designed for the 1xN demultiplexer and described in Chapter 5 cannot be used for an NxN WDM router because it does not provide diffraction limited imaging for all the N-input fibres.

In this chapter a design of a new free-space switchless 91x91 router [10] with 0.333 nm channel separation is presented. The router consists of a concave holographic grating configured in a stationary anastigmatic Littrow mount (see section 4.6.4) and 2 arrays of input and output fibres. A simple method for calculating directly the coupling efficiency, crosstalk and transmission spectrum is developed. Methods for the realisation of full-mesh routing are discussed. Tolerances analysis, aberrations, and transmission characteristics are described.

6.2 Routing realization and formulae

Consider a $(2K+1)$x$(2K+1)$ router with $2K+1$ input fibres. Each input fibre has the same set of $2K+1$ equally spaced wavelengths. In this case we need $4K+1$ output fibres to

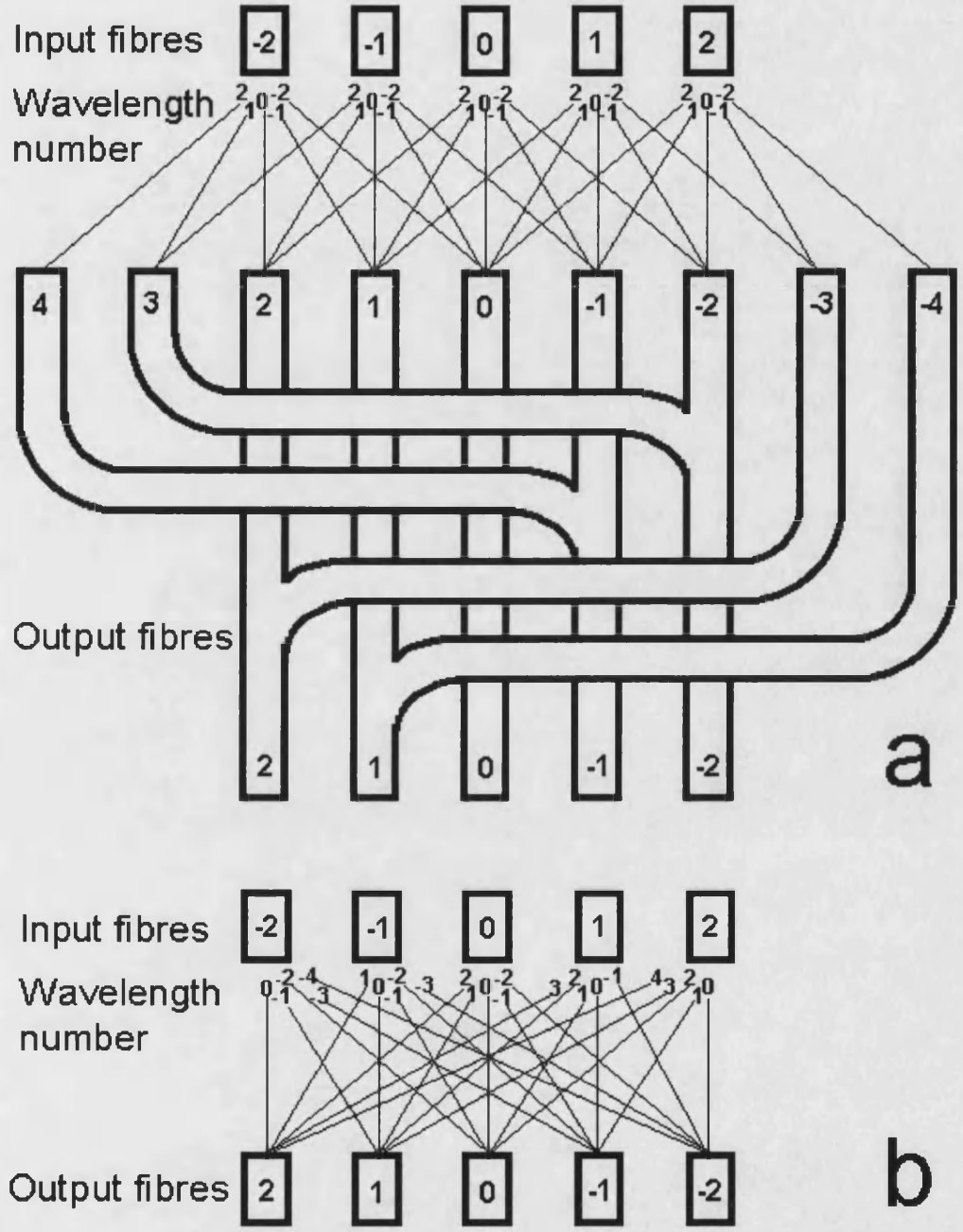

Fig.6.1. **Schematic configuration of 5x5 router with a set of 5 wavelengths (a), and 9 wavelengths (b).**

select all the channels, as shown in Fig. 6.1a for $2K+1=5$. For the sake of symmetry we assign the number 0 to the central wavelength, input, and output fibres. This results in negative numbers, but gives a simple routing formula

$L=M+N$ (6.2),

where L is the wavelength number ($-K \leq L \leq K$), M is the number of input fibre ($-K \leq M \leq K$), and N is that of output fibre ($-2K \leq N \leq 2K$). However the main goal of a $(2K+1)$x$(2K+1)$ passive wavelength router is to provide a cyclic (full-mesh) interconnection between $(2K+1)$ nodes. For this purpose the output fibres can be combined in pairs by Y couplers as shown in Fig. 6.1 a at the expense of 3 dB additional loss. Each I-th output fibre ($I<0$) is connected with J-th output fibre ($J>0$) according to the formula $I=J-(2K+1)$. Consequently, this realizes $(2K+1)$x$(2K+1)$ full-mesh connections with only $(2K+1)$ wavelengths. The routing formula for this approach can be expressed as

$L=(M+N)-(2K+1)\mathbf{fix}[(M+N)/(K+1)]$, (6.3)

where function **fix** rounds the argument to the nearest integer towards zero.

The resulting logical connectivity patterns become a $(2K+1)$x$(2K+1)$ star network as shown in Fig. 6.2a ($2K+1=5$). All the nodes can communicate with each other at the same time,

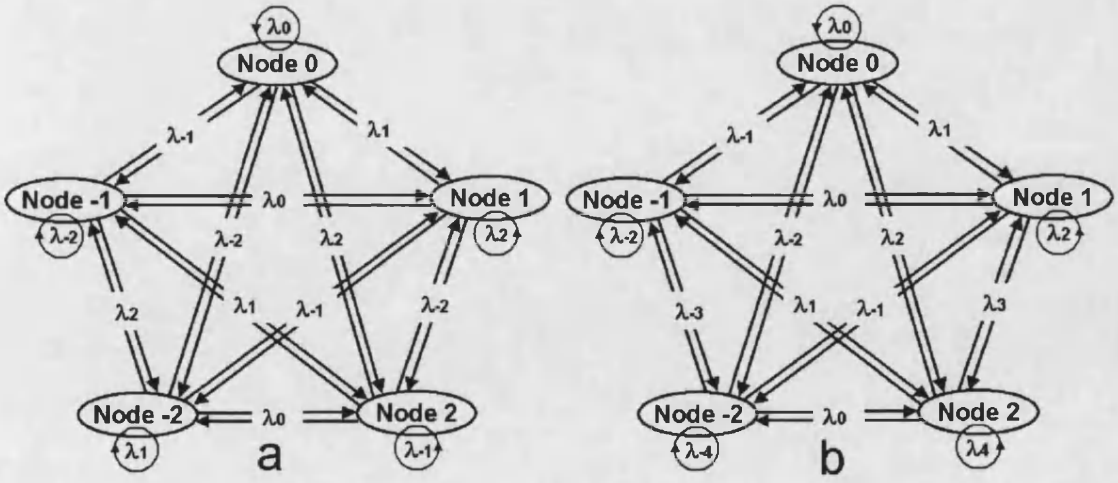

Fig.6.2. **Logical connectivity for 5x5 router with a set of 5 wavelengths (a), and 9 wavelengths (b).**

thus enabling $(2K+1)^2$ optical interconnections simultaneously.

Full-mesh interconnection according to Equation (6.2) can be realized using the set of $4K+1$ equally spaced wavelengths and $2K+1$ input/output fibres, as shown in Fig. 6.1b. Each input and output port has $2K+1$ wavelengths as before, but their composition varies from fibre to fibre. This eliminates the 3 dB combining loss at the expense of doubling in the number of wavelengths used. The logical connectivity for this case is shown in Fig.6.2b.

The cyclic property of wavelength routers provides an important additional functionality, as compared to simple multiplexers or demultiplexers, and plays a key role in more complex devices such as add/drop multiplexers and wavelength switches. To realize such an interconnectivity scheme in a strictly non-blocking way using a single wavelength, a huge number of fibres and switches would be required. Using the cyclic property, this functionality can be achieved with only one wavelength router.

6.3 Basic equations for losses, crosstalk, and passband calculations

We refer to Fig. 6.3 to define a Cartesian co-ordinate system $Oxyz$, whose origin O is at the grating vertex, xy is the dispersion plane, and the x axis is normal to the grating spherical surface $x(y,z) = R - \sqrt{R^2 - y^2 - z^2}$, where R is the curvature radius. Denote $S(y,z \mid Q) = \sqrt{(x_Q - x(y,z))^2 + (y_Q - y)^2 + (z_Q - z)^2}$ as the distance from an arbitrary point $Q(x = x_Q, y = y_Q, z = z_Q)$ to the point (y,z) on the grating surface. Assume that the facet of the input fibre M directed towards the grating vertex is at point A_M and facet of the

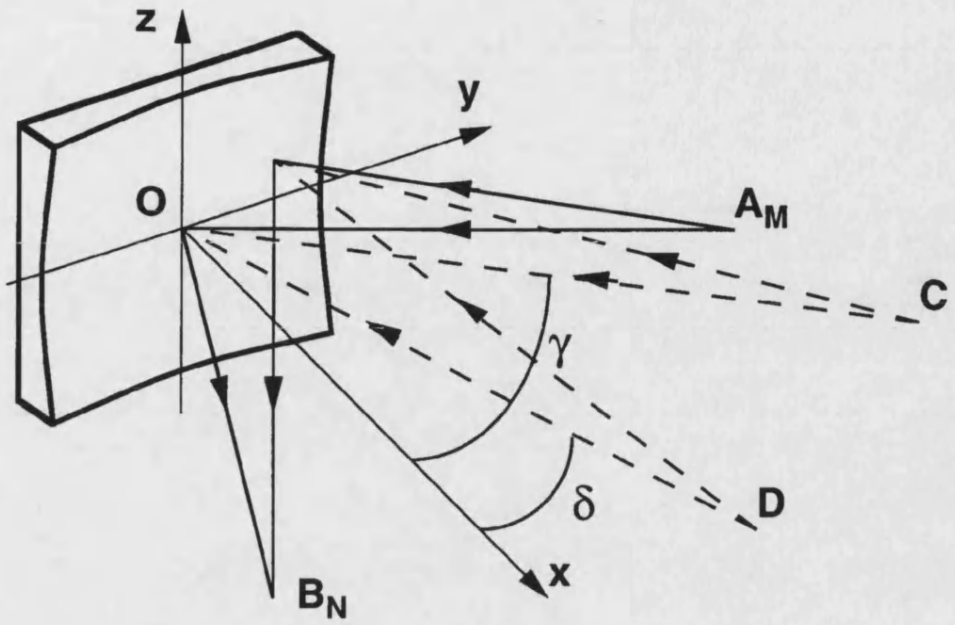

Fig. 6.3. **Illustrating the positions of input/output fibres and recording sources.**

output fibre N is at point B_N. The wave aberration of the first diffraction order concave holographic grating for "imaging" A_M into B_N at the wavelength λ_L can be written as [11]

$$W_{LMN}(y,z) = \lambda_L m_H(y,z) - S(y,z \mid A_M) - S(y,z \mid B_N) \ , \qquad (6.4)$$

where $m_H(y,z) = [S(y,z \mid C) - S(y,z \mid D)]/\lambda_H$ is the function describing the holographic grating recorded at the wavelength λ_H by two point sources C and D shown in Fig. 6.3.

The coupling efficiency η_{LMN} from input fibre M into the output fibre N at the wavelength λ_L can be expressed as an overlap integral [12] at the grating surface σ

$$\eta_{LMN} = \left| \iint_{\sigma} |E_M E_N| \exp(j 2\pi W_{LMN} / \lambda_L) dydz \right|^2 \ , \qquad (6.5)$$

where E_M and E_N are the normalized amplitudes of the input and output fibres, respectively, calculated using equation (5.15). The useful coupling efficiency for the signal routed, according to formula (6.2), from the input fibre M into the output fibre N

is $\tau_{M\to N} = \eta_{LMN}$ when $L = M + N$. The spectral response for this signal can be calculated by varying the wavelength λ_L in Equations (6.4) and (6.5). All other values η_{LMN} when $L \neq M + N$ are the various crosstalk contributions into the output fibre *N*. The presented equations are valid for any mount of concave grating and input/output fibres' positions.

6.4 Router configuration

As shown in Chapter 4, the stationary anastigmatic (SA) mounts of a concave grating [11] can provide diffraction limited imaging of a multi-wavelength point source within the C-band of the gain bandwidth (around 1530-1570 nm) of erbium-doped fibre amplifiers. This allows a high coupling efficiency and low level of crosstalk in WDM demultiplexers. However, unlike the demultiplexer, the router must have both input and output fibre arrays, with a large number of fibres to maximize the port count. To achieve diffraction limited imaging from every input fibre to every output fibre the concave grating mount should be stationary anastigmatic in both directions. Numerical analysis of different mounts leads to the conclusion that the optimal performance is provided by a stationary anastigmatic Littrow mount described in section 4.6.4. The combination of a high diffraction efficiency (>90%) and low PDL (<0.25 dB) for a holographic grating with a specially distorted sinusoidal profile [13] can be achieved for the incidence and diffraction angles in a range of 30°±4°. These uniquely determine the chosen router geometry.

The proposed router layout is shown in Fig. 6.4 a. The grating curvature radius is *R*=100 mm. The facets of all input and output fibres must lie in a step-wise shape along the x'-axis originating at the grating curvature centre O', with the angle of 60° to the *x*-axis. The array of input fibres is 25 μm above the dispersion plane and the output fibre array is 25 μm below this plane. Central input and output fibres are directed towards the grating

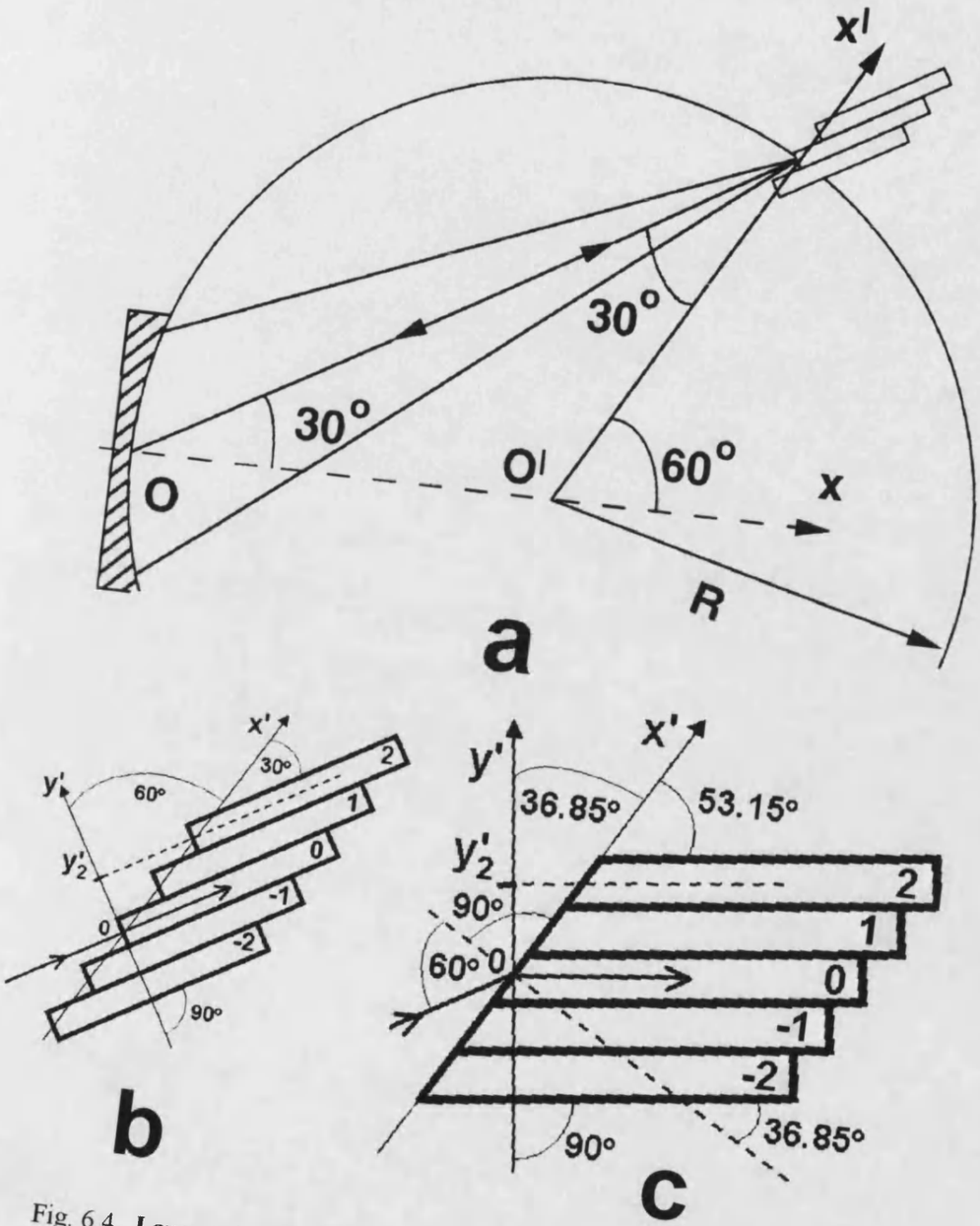

Fig. 6.4. **Layouts in dispersion plane for wavelength router (a), staircase fibre array (b), and diced fibre array (c).**

vertex and fixed one under another at the point where the x'-axis crosses the continuation of grating sphere. This mount is stationary anastigmatic for the central input fibre and both focal curves are tangential to the x' axis.

The chief ray at the central wavelength λ_0=1552 nm from the central input fibre is incident at the angle of 30° to the grating vertex and diffracts back at the same angle into the central output fibre. Therefore, according to Eq. (6.1), the period at the grating centre is $b=\lambda_0$.

As before, consider a (2K+1)x(2K+1) router (K=45) with a routing formula $L=N+M$, where L is the wavelength number, M is the number of input fibre, and N is that of output fibre. The total number of input fibres is 2K+1 ($-K\leq M\leq K$). The number of routing wavelengths can be 2K+1 ($-K\leq L\leq K$) or 4K+1, resulting in 4K+1 ($-2K\leq N\leq 2K$), or 2K+1 ($-K\leq N\leq K$) output fibres, correspondingly, as shown in Fig. 6.1. For the second case each input fibre M still has 2K+1 wavelengths with $-K+M\leq L\leq K+M$. The L-th wavelength is determined by $\lambda_L = \lambda_0 + L\Delta\lambda$, where $\Delta\lambda$=0.333 nm. First find the angular positions a_M for each input fibre to meet the routing $L=M+0$ to the central output fibre. In this case the diffraction angle β_0 at the grating centre is constant ($\sin\beta_0=1/2$), and the incidence angle a_M from the M-th input fibre is defined from (6.1) as

$\sin\alpha_M=[\lambda_0+M\Delta\lambda]/\lambda_0-\sin\beta_M=M\Delta\lambda/\lambda_0+1/2$.

In the same way, the angular positions (the diffraction angles) β_N are determined for each output fibre to meet all possible routes $L=M+N$

$\sin\beta_N=[\lambda_0+(M+N)\Delta\lambda]/\lambda_0-\sin\alpha_M=N\Delta\lambda/\lambda_0+1/2$.

So, this means that the position of the N-th output fibre is independent of the route (input fibre) for the case of equally spaced routing wavelengths, which is not valid for a periodic

frequency comb. Moreover, the input and output fibres with equal numbers M=N=J have the same angular position θ_J in xy plane defined as

θ_J=asin[$J\Delta\lambda/\lambda_0$+1/2]. (6.6)

The fibre positions in a grating coordinate system $Oxyz$ can be derived trigonometrically as

$$x_J = \frac{\sqrt{3}}{2}\frac{R\cos\theta_J}{\sin(60^\circ - \theta_J)};\ y_J = \frac{\sqrt{3}}{2}\frac{R\sin\theta_J}{\sin(60^\circ - \theta_J)};\ z_J = \pm 25\,\mu\text{m}, \quad (6.7)$$

where θ_J is from Eq. (6.6), z_J=+25 μm for the input and –25 μm for the output fibres. These formulae are to be substituted into Equations (6.4) and (6.5) for calculating the router performance characteristics. The distance from the central input/output fibre to the grating vertex is $r_{\alpha 0}$=$r_{\beta 0}$=2Rcos30°=173.2051 mm.

Now determine the position y'_J in V-groove array for J-th input/output fibre, as shown in Fig. 6. 4 b. Simple trigonometric computations and setting $y'_0 = 0$ result in

$$y'_J = R[\sin\theta_J / \sin(60^\circ - \theta_J) - 1]\cos 60^\circ. \quad (6.8)$$

Substituting (6.6) into (6.8) gives

$$y'_J = R[1/(\sqrt{3/(1/2 + J\Delta\lambda/\lambda_0)^2 - 3} - 1) - 1/2]. \quad (6.9)$$

The fibre spacing y'_J - y'_{J-1} varies within the range of 41.07-44.90 μm for 91 input fibres and 39.35-47.08 μm for 181 output fibres.

However, it is extremely difficult to fix all the fibres in a staircase array. More feasible is to cut and polish the facet of the fibre array as shown in Fig. 6.4 c. The refractive index 1.444 of a fused silica at 1552 nm and 60° incidence angle give the refraction angle of 36.85°. This defines the cutting angle relative to the fibre core as 90-36.85=53.15°. Fibres' positions in V-groove array for this configuration are determined as

$y'_J = R[\sin\theta_J / \sin(60^\circ - \theta_J) - 1]\cos 36.85^\circ$, and fibre spacing varies from 62.97 to 75.34 μm for the case of 181 output fibres.

The main side effect for such type of fibre array is a high PDL due to a large incidence angle at the air-fused silica boundary. It can be derived from Fresnel formulae [14], that refraction leads to a PDL = $-10\log[\cos^2(\gamma_i - \gamma_r)]$, where γ_i and γ_r are incidence and refraction angles, respectively. In our case, after double refraction, the PDL=1.46 dB. This effect can be eliminated using special multilayer anti-reflection coatings [15].

6.5 Optimisation of the recording scheme

This analysis was carried out for a holographic grating recorded at the wavelength λ_H=457.935 nm. Initially, the recording scheme minimizing RMS wave aberration $\overline{W}_{000}$, defined by Eq. (6.4), for imaging from the central input fibre to the central output fibre at λ_0=1552 nm was found using the method described in a section 5.5.1. A minimum value $\overline{W}_{000}=0.0046\lambda$ (a factor of 15 smaller than the diffraction limit) within NA=0.11 is provided by recording sources $C\,(x = r_C\cos\gamma,\ y = r_C\sin\gamma,\ z = 0)$, and $D\,(x = r_D\cos\delta,\ y = r_D\sin\delta,\ z = 0)$ defined by

r_C=2.292028R; r_D=1.269899R; γ=41.461850°; δ=21.534414°.

However, imaging from the input fibres at the extreme ends of the array gives much higher aberrations, as shown in Fig. 6.5 a and b, for the cases of 91- and 181- wavelength routers, respectively. Balancing the aberrations between all the possible routes results in the following recording schemes:

r_C=2.293051R; r_D=1.270339R; γ=41.449630°; δ=21.524568°

for 91 wavelengths router, and

r_C=2.292256R; r_D=1.270016R; γ=41.457281°; δ=21.530733°

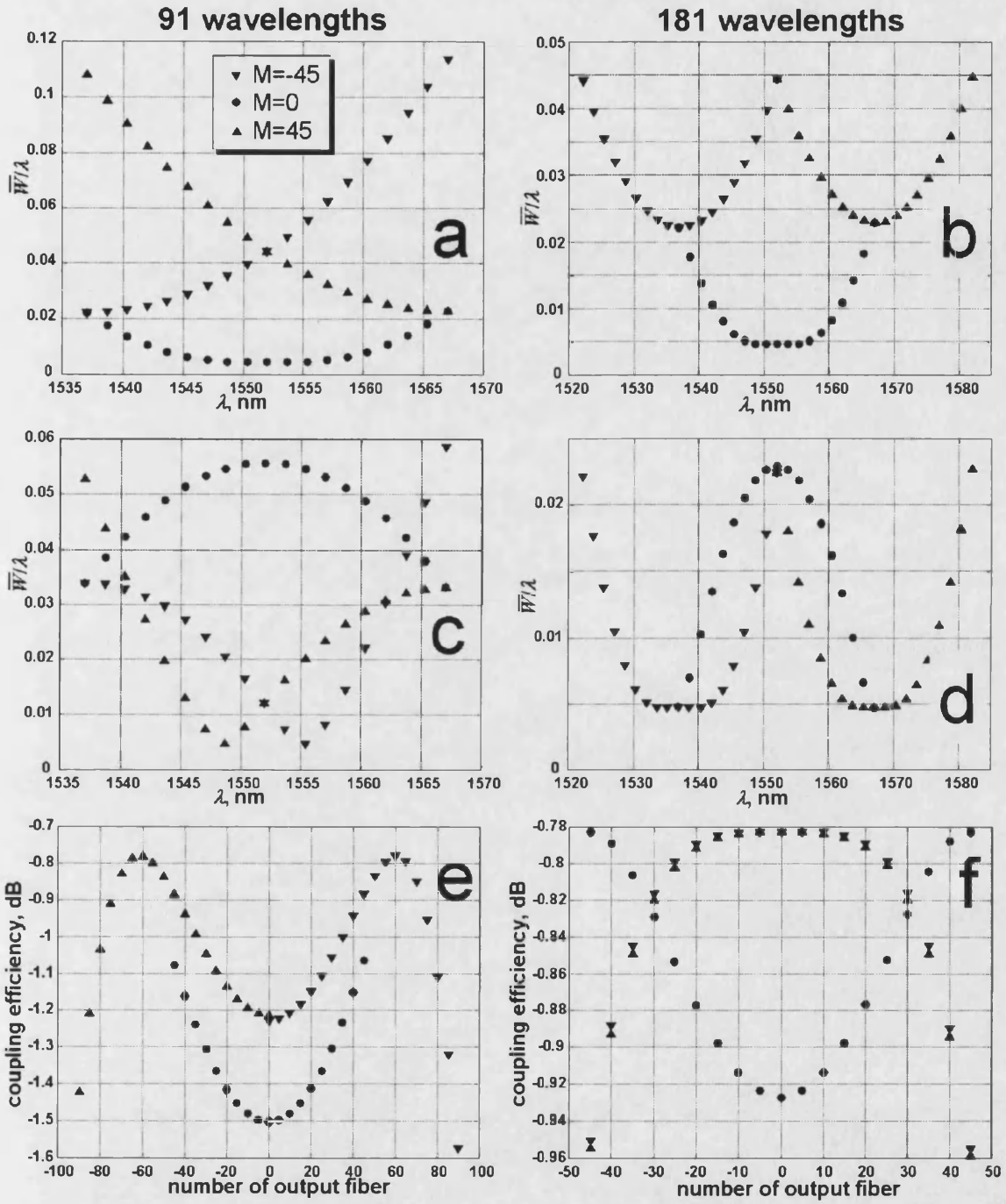

Fig. 6.5. **RMS wave aberration as a function of wavelength for three input fibres (M=-45, 0, 45): initial (a, b) and final (c, d) step of optimization. The coupling efficiency for different routes $M \rightarrow N$ (e, f) of optimised design.**

for 181 wavelength router. The resultant aberrations for these recording parameters are shown in Fig. 6.5 c and d, correspondingly. The coupling efficiencies from the central and edge input fibres to various output fibres, calculated from Equation (6.5), are shown in Fig. 6.5 e and f for 91 and 181 wavelengths router, respectively. These calculations are realized for fibres with a numerical aperture of 0.1 and grating diameter of 64 mm. 0.46 dB of additional losses are added to each channel matching minimum diffraction efficiency of 90% from the reference [13]. A higher number of wavelengths, and, correspondingly, smaller number of output fibres, give a factor of 2.5 lower aberrations and about 0.5 dB higher coupling efficiency.

6.6 Tolerances

Tolerances on the misalignments and accuracy of the concave grating fabrication were estimated for the 181 wavelength router by constraining the additional losses to 0.3 dB. The input and output fibres are fixed together as a single element and therefore, all possible misalignments in the router are defined by the displacement of the fibre array relative to the grating vertex. Because the input and output fibres are misaligned simultaneously in the same direction, any linear displacement gives a double lateral shift of image or twice the defocus, relative to the output fibre facet. This results in 0.3 μm admissible lateral displacements and 6 μm defocus, which are a factor of two smaller compared to the tolerances for the output fibre array in the demultiplexer, described in section 5.9.2. All allowable tilts around the midpoint of the central fibre facet are defined by the requirements that the resulting lateral displacements of the edge fibres' facets are within ±0.3 μm. The calculated angular margins of ±0.005° and ±0.009° are a real

challenge for adjustment and tuning. All the described tolerances on the position of input/output fibres array are shown in Fig. 6.6 for clarity.

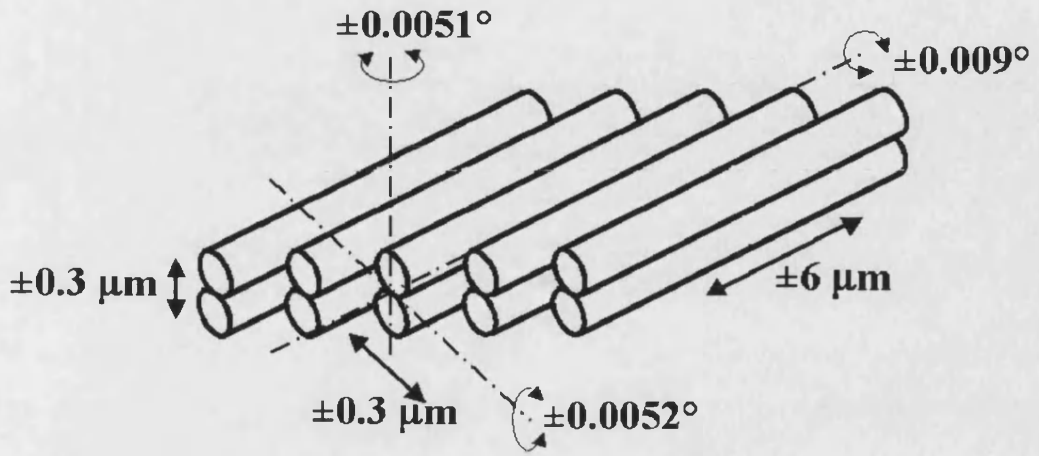

Fig. 6.6. **Tolerances in the position of input/output fibre array.**

The tolerances on the parameters of the holographic recording scheme and the grating curvature radius were determined by MATLAB simulation programs, in a way similar to that in section 5.9.3. For each iteration, the angle and the distance from the grating vertex for the central input/output fibre were determined by equating to zero wave aberration expansion coefficients A_{10} and A_{20} described in section 5.5.1. This defines the readjusted position as

$$\alpha_0 = \beta_0 = \arcsin[\frac{\lambda_0}{2\lambda_H}(\sin\gamma - \sin\delta)],$$

$$r_{\alpha 0} = r_{\beta 0} = 2\cos^2\alpha_0\left[\frac{\lambda_0}{\lambda_H}\left(\frac{\cos^2\gamma}{r_C} - \frac{\cos^2\delta}{r_D} - \frac{\cos\gamma - \cos\delta}{R}\right) + \frac{2\cos\alpha_0}{R}\right]^{-1}.$$

After that the fibre array was slightly rotated in the dispersion plane to maximize the merit function, defined as

$MF = \min[\tau_{-45\to-45}, \tau_{-45\to0}, \tau_{-45\to45}, \tau_{0\to-45}, \tau_{0\to0}, \tau_{0\to45}, \tau_{45\to-45}, \tau_{45\to0}, \tau_{45\to45}]$, where $\tau_{M\to N}$ is the useful coupling efficiency for the route $M\to N$, defined in a section 6.3. Less

than 0.3 dB decrease of the merit function compared to the initial value corresponds to the following tolerances: -0.009 mm<ΔR<0.014 mm, -0.045 mm<Δr_C <0.069 mm, -0.020 mm <Δr_D <0.024 mm, -0.015°<$\Delta\gamma$<0.031°, -0.019°<$\Delta\delta$<0.018°. Tolerances on the grating curvature radius are much smaller compared to the demultiplexer. This is due to the fact that in a case of the demultiplexer, the magnification coefficient can be varied to fit the linear dispersion by readjusting both the input fibre and output fibres array independently. The router, however, must always have unit magnification because the input and output fibres are in the same positions.

6.7 Bandwidth, crosstalk and the optimum router dimensions

All the calculations of transmission characteristics below have been carried out for a grating on a circular substrate using Equations (5.15), (6.4) and (6.5). The grating diameter D_g is related to the input/output numerical aperture NA_D in the dispersion direction approximately as $NA_D=(D_g/r_{\alpha 0})\cos 30°/2=D_g/(4R)$. The fibre numerical aperture is 0.1 at e^{-2} intensity level, as before.

The transmission spectra for the 91-wavelength router (NA_D=0.16) from -45^{th} 0^{th} and 45^{th} input fibres to the output fibres with the highest and lowest losses (defined from Fig. 6.5 e) are shown in a Fig. 6.7. The transmission spectra for the 181-wavelength router from the central and extreme input fibres to -45^{th} 0^{th} and 45^{th} output fibres are shown in a Fig. 6.8. The crosstalk from the adjacent channels ($\Delta\lambda$=±0.333 nm) does not exceed –50 dB for all cases. A large variation in the passband shape for the 91 wavelength router results

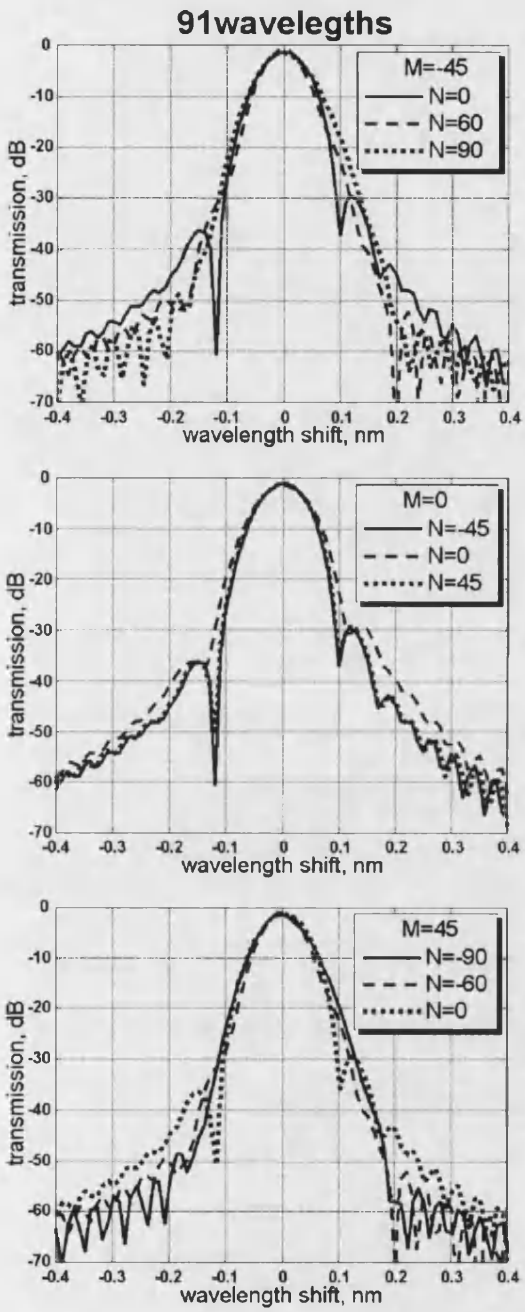

Fig. 6.7. **91-wavelength router. Transmission spectra for different routes $M \rightarrow N$.**

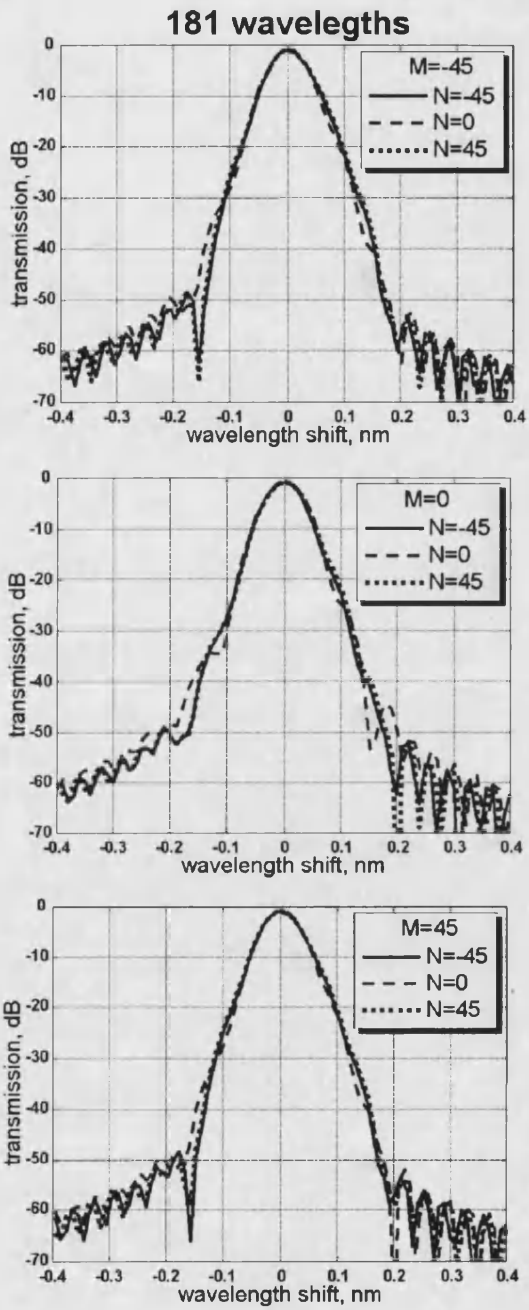

Fig. 6.8. **Same as Fig. 6.6 for 181-wavelength router.**

in variation of the 1-dB bandwidth from 0.038 to 0.052 nm with the upper bound corresponding to the channels with the higher losses. This can be explained by the residual aberrations resulting in the broadened image of the fibre mode. More uniform transmission spectra for the 181-wavelength router give 1 dB bandwidth in the range of 0.038-0.040 nm, which is only 12% of the channel spacing. The bandwidth can be broadened by approximately a factor of 3 if all input fibres are pigtailed to the waveguide concentrator with 91 multimode interference couplers. However this will increase the device cost and introduce about 2.7 dB additional losses, as described in Chapter 5.

The most direct way to increase the 1-dB bandwidth is to decrease proportionally all router dimensions, including the spacing between the adjacent fibres and the holographic recording scheme. This will result in a smaller linear dispersion and, consequently, a wider passband. Fig.6.9 makes a comparison of the passband shapes for the initial, two times larger and two times smaller routers. The smaller device dimensions are very attractive for customers, but result in higher crosstalk. The crosstalk between the adjacent channels is increased due to the smaller fibre separation, resulting in higher contribution from the image tails, and background crosstalk is increased inversely proportional to the square of the router size, as described in section 3.6.1. According to the experimental data from Chapter 3 the level of background noise due to diffuse scattering from the holographic concave grating is –60 dB when an output fibre is at a distance of 100 mm. This means that for an arbitrary router or demultiplexer the relative value of background noise can be estimated as

$\sigma_d=(100\ \text{mm}/r_{\beta 0})^2 \text{x} 10^{-6}$, (6.10)

where $r_{\beta 0}$ is the distance from the central output fibre to the grating vertex, which is designated later on as the router size. For $r_{\beta 0}$=173.2051 mm of the initial design this gives: $\sigma_d=3.3\text{x}10^{-7}$.

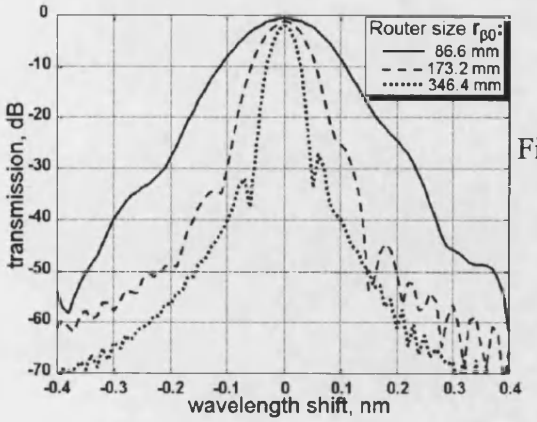

Fig. 6.9. **Demonstrating the effect of the router size on a passband shape for 0→0 signal of 181 wavelengths router.**

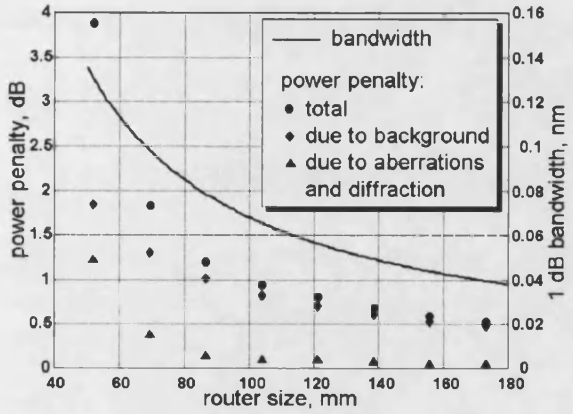

Fig. 6.10. **Power penalty and 1 dB bandwidth as a function of router size.**

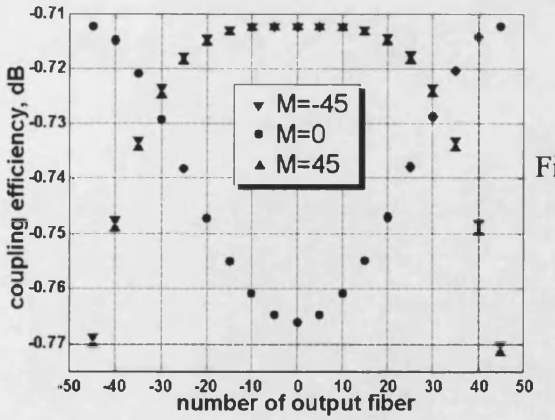

Fig. 6.11. **Coupling efficiency of different routes $M \rightarrow N$ for the size $r_{\beta 0}$=100 mm.**

It is important to estimate the performance degradation arising from the decrease of device dimensions, aimed towards bandwidth broadening Consider the coherent crosstalk for a signal routed from the central input (M=0) to the central output fibre (N=0) at wavelength λ_0. The worst case is assumed when all the noise sources at this wavelength have the opposite phase to the signal and match its polarization. For the fixed decision threshold in the receiver, the power penalty P_{00} for this signal can be estimated [6] as

$$P_{00} = -10\log(1-2\sqrt{\varepsilon_{00}}), \quad (6.11)$$

where

$$\varepsilon_{00} = (2K\sqrt{\sigma_d} + \sum_{M\neq 0}\sqrt{\eta_{0M0}/\tau_{0\to 0}})^2, \quad (6.12)$$

is cumulative coherent crosstalk from $2K$ input fibres ($M\neq 0$) at the wavelength λ_0, calculated as a sum of all amplitudes. The first term is related to the aggregate background noise, and the second term is the contribution from aberrations and diffraction at the aperture. Incoherent crosstalk is defined by characteristics of the demultiplexer or tuneable filter at the receiver, and is not considered here. Besides, the contribution of incoherent crosstalk to signal degradation is much smaller.

The power penalty P_{00} due to coherent crosstalk, and 1-dB bandwidth are shown in Fig.6.10 against the geometrical size of a 91x91 (K=45) router with 181 routing wavelengths for numerical aperture NA_D=0.16. The contribution to cumulative coherent crosstalk from diffraction at the aperture and aberrations is very small. It becomes comparable with the background input when the router size is smaller than 60 mm (fibre separation of about 15 μm). The acceptable power penalty of 1 dB corresponds to a router size of 100 mm with 25 μm fibre separation and 1-dB bandwidth of 0.068 nm (20.4% of channel spacing). The performance degradation, due to scaling down, for other routed

channels is approximately the same. Crosstalk from adjacent channels is increased to about -47 dB due to scaling. All the aberrations are decreased proportionally to the router size, resulting in higher coupling efficiencies for all routes, as shown in Fig.6.11 (compare to Fig.6.5 f for $r_{\beta 0}$=173.2051 mm). The highest loss is 0.77 dB, including 90% diffraction efficiency, which is 0.2 dB lower than for the initial router size. Further reduction in the dimensions of the 91x91 router is problematic due to the rapidly increasing crosstalk.

6.8 Conclusions

This chapter described a novel design of a 91x91 free-space concave grating wavelength router with the channel spacing of 0.333 nm. It was shown that full-mesh routing between 91 ports can be realized with two approaches: using 91 wavelengths and combining 181 output fibres in pairs using Y couplers, or just using 181 wavelengths. The second method requires double the number of controllable stable wavelengths, but it is more attractive because of the substantially lower cost and 3.5 dB of transmittance gain (3 dB due to the elimination of Y couplers and 0.5 dB due to smaller aberrations).

The optimum router dimension of 100 mm (distance from fibres array to grating) is defined from the trade-off between the transmission bandwidth and coherent crosstalk. This gives 25 μm fibre separation, 1 dB bandwidth of 0.068 nm for a Gaussian spectral response, less than 0.8 dB losses, and 1 dB power penalty due to coherent crosstalk. The incoherent crosstalk between the adjacent channels is –47 dB.

Two types of fibres array configuration are proposed. A simple method for the evaluation of the router transmission characteristics is developed. A holographic recording scheme was optimised to minimize aberrations within all possible routes. A tolerance analysis for the fabrication of the concave grating and the positioning of the fibre array

relative to grating is described. The experimental results carried out recently by Vitaly Mikhailov et al [16, 17] using the described grating and fibre array fabricated to this design by Chris Doerr (Bell Laboratories, Lucent Technologies), are in a good agreement with predicted performance characteristics.

References to Chapter 6

[1] G. R. Hill, "A wavelength routing approach to optical communication networks," *BT Technol. J.*, vol.6, 1988, pp.24-31.

[2] M. Young, H. Laor, and E. J. Fontenot, "First in-service network application of optical cross-connects," *Proc. OFC 1998*, paper PD23.

[3] I. Chlamtac, A. Ganz, and G. Karmi, "Prely optical networks for terabit communication," *Proc. IEEE INFOCOM 1989*, pp.887-896.

[4] O. Gerstel, "On the future of wavelength routing networks," *IEEE Network*, vol.10, 1996, pp.14-20.

[5] P. E. Jr. Green, "Optical networking update," *IEEE J. Select. Areas Commun.*, vol.14, 1996, pp.746-779.

[6] A. M. Hill, S. Carter, J. Armitage, M. Shabeer, R. A. Harmon, and P. Rose, "A Scaleable and Switchless Optical Network Structure, Employing a Single 32x32 Free-Space Grating Multiplexer," *IEEE Photon. Technol. Lett.*, vol.8, 1996, pp.569-571.

[7] P. A. Bernasconi, C. R. Doerr, C. P. Dragone, "Large NxN waveguide grating router," US patent 6381383 B1, Apr.30, 2002.

[8] J. F. Verrill. "The specification and measurement of scattered light from diffraction gratings," *Optica Acta*, vol.25, 1978, pp.531-547.

[9] E. G. Churin, P. Bayvel. "Coherent crosstalk and scalability of free-space wavelength routers," *IEE Electronics Letters*, vol.34, 1998, pp.1225-1227.

[10] E. G. Churin, P. Bayvel, "Design of free-space WDM router based on holographic concave grating", *IEEE Photon. Technol. Lett.*, vol.11, 1999, pp.221-223.

[11] E. G. Churin, P. Bayvel, A. Stavdas, J. E. Midwinter, A. M. Hill, "Stationary anastigmatic mounts of concave gratings," *Applied Optics*, vol.36, 1997, pp.3444-3451.

[12] R. E. Wagner, and W. J. Tomlinson, "Coupling efficiency of optics in single-mode fibre components," *Applied Optics*, vol.21, 1982, pp. 2671-2688.

[13] M. Iida, K. Hagivara, and H. Asakura, "Holographic Fourier diffraction gratings with a high diffraction efficiency optimized for optical communication systems," *Applied Optics*, vol.31, 1992, pp. 3015-3019.

[14] Born, M. and Wolf, E, *Principles of Optics*. Pergamon Press, London, 1970.

[15] J. C. Monga, "Double-layer Broadband antireflection coatings for grazing incidence angles," *Applied Optics*, vol.31, 1992, pp.546-553.

[16] V. Mikhailov, P. Bayvel and E. G. Churin, "0.53 bit/s/Hz spectral efficiency free-space demultiplexer with very low crosstalk, loss and polarisation dependence", *IEE Electronics Letters*, vol.36, 2000, pp. 1640-1641.

[17] V. Mikhailov, C. Doerr and P. Bayvel, "Ultra low coherent crosstalk, high port-count free-space wavelength router," *Proc. OFC 2003*, paper TuN5.

Chapter 7

Concave grating channel power equalizer

7.1 Introduction

The previous chapters described completely passive devices based on concave gratings and used for channel multi/demultiplexing and wavelength routing in WDM optical networks. In addition to passive components, such as routers and demultiplexers, there is also a need for active devices which incorporate a dispersive element, to perform the functions required in optical networks, such as channel power equalization [1,2], gain flattening [3,4] and add/drop multiplexing [5,6]. In such devices a multi-wavelength signal is dispersed and after the required manipulation or processing is recombined into a single output fibre. Concave gratings can also be successfully used in these devices, but to date this has not been reported. In this chapter, the possibility of using concave gratings in a channel power equalizer is investigated.

In large channel-count WDM networks, it is important to ensure that none of the channels becomes significantly weaker than the others, otherwise a reduction in optical signal-to-noise ratio could result in transmission penalties. This can be achieved using periodic channel equalisation. Devices that can dynamically equalize the power on a channel-by-channel basis typically consist of a demultiplexer, an array of controllable attenuators, and a multiplexer (or power combiner). Different attenuators have been proposed for this purpose: MEMS (micro-electro-mechanical systems) array of tilting mirrors [6]; MEMS etalons [7]; and liquid-crystal cells [8].

7.2 Optical schemes

By way of an example, consider a free-space channel power equalizer proposed by Ford *et al* [1] and shown in Fig. 7.1. Light from the input fibre is collimated, diffracts from a plane gold-coated 600-lines/mm blazed grating, then focused by a 50-mm lens onto an array of modulators. This lens is vertically displaced so that the light reflected back is spatially separated from the input. The attenuated signals are collected by a second pass through the grating, reflect from a small fold mirror, and focused into a separate output fibre. The PDL is avoided by using a quarter-wave plate in the collimated beam to rotate the polarization of the reflected light for the second pass through the grating. The device in [1] had 4.6 dB insertion loss, 0.2 dB PDL, 20 dB dynamic range, 10 μs response time and 24 nm operating spectral range.

The same physical principles can be applied to a system incorporating a concave grating with a dramatic decrease of the number of optical elements as shown in Fig. 7.2a,. However, both schemes are very sensitive to misalignments of all components. The best way to reduce this sensitivity is to set up a retro-reflective optical scheme as shown in Fig. 7.2b by using a fibre circulator. In this case the light return path is always to the input/output fibre and the scheme is not sensitive to the lateral misalignments of the fibre or concave grating. Associated with this is a penalty in the doubling of the sensitivity to defocusing of the input/output fibre. However, as shown in section 5.9.2 this an acceptable trade-off, because the lateral misalignments are approximately a factor of 10 more critical than defocus. The typical additional insertion loss introduced by the circulator is in the range of 0.5-1 dB.

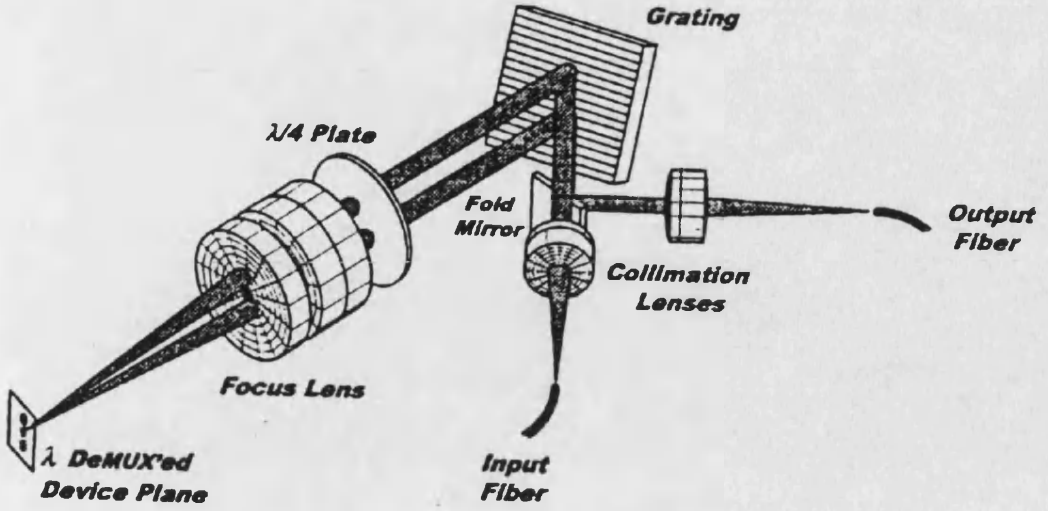

Fig.7.1. **Channel power equalizer from Bell Laboratories, Lucent Technologies. After J. E. Ford, 1998.**

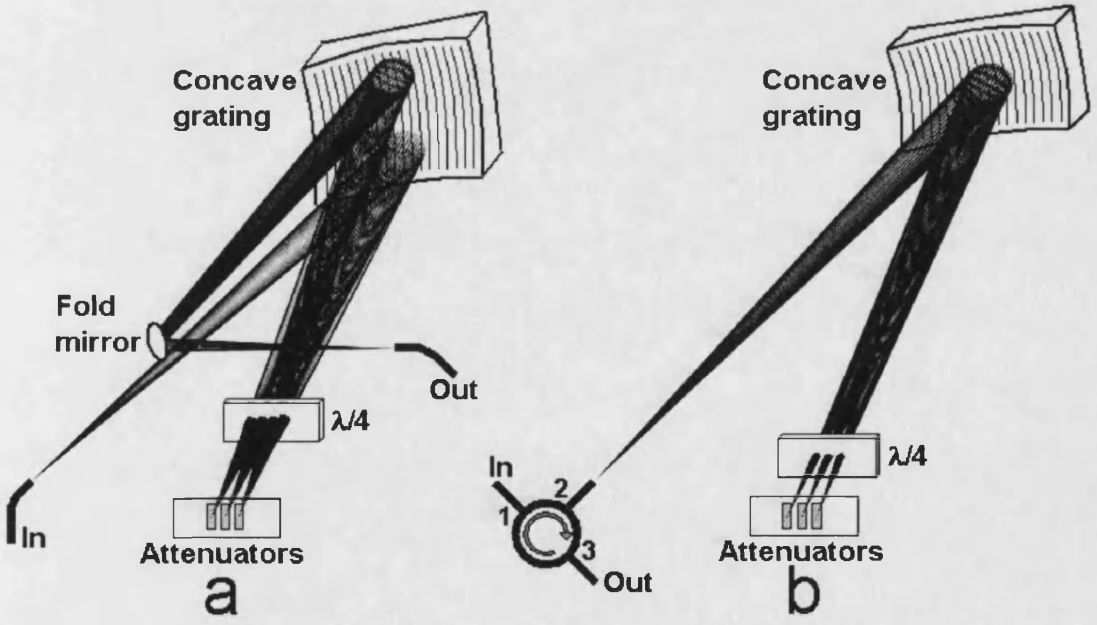

Fig.7.2. **Concave grating-based channel power equalizer with fold mirror (a) and with circulator (b).**

7.3 Ray-tracing analysis

Consider, as a basis, the optical scheme of the demultiplexer described in a Chapter 5. The input/output fibre of the circulator is in the position of demultiplexer input, whilst the modulator array is placed in the former position of the output fibres. Figure 7.3a shows the ray-tracing spot diagrams calculated for different wavelengths on the surface of attenuators

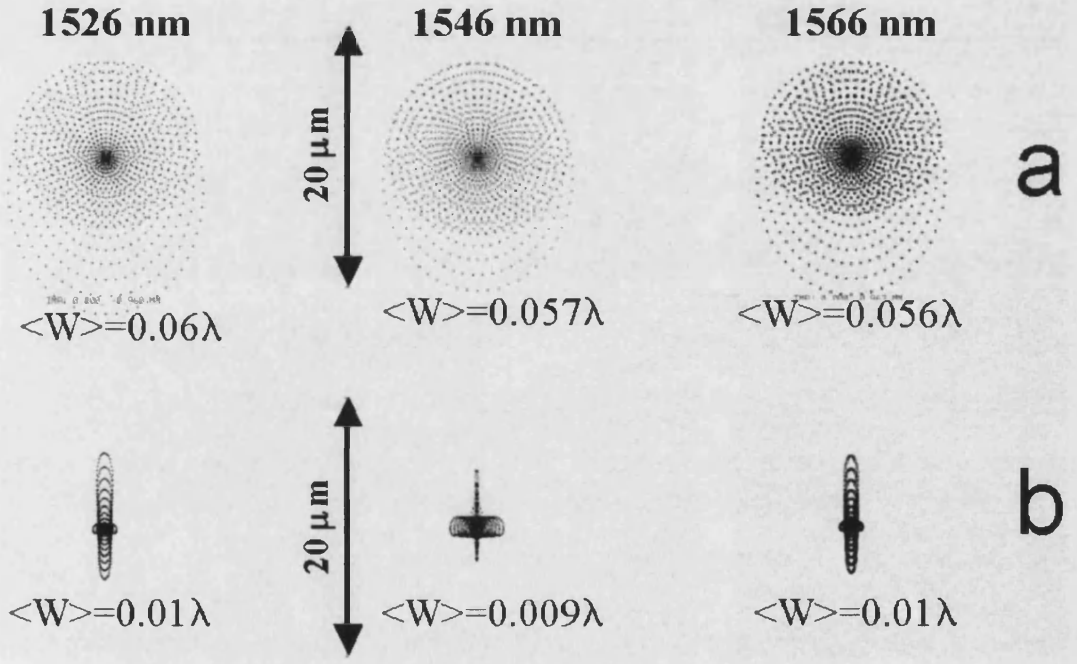

Fig.7.3. **Ray-tracing spot diagrams on the attenuator array plane (a) and on the output fibre (b).**

(numerical aperture NA=0.11 with uniform illumination). The spot diagrams at the facet of output fibre after reflection back from the attenuator array are shown in Fig. 7.3b and reveal very good aberration compensation compared to that achieved with the demultiplexer alone. This is because all the odd terms in the wave aberration expansion (Equation &.3) vanish, as each ray returns through a diametrically opposite point of the concave grating, and the main contribution to the aberration of a demultiplexer was from coma, as described in section 5.5.2. The RMS wavefront errors <W> were calculated for

every wavelength and, as can be seen in Fig 7.3, do not exceed $\lambda/100$. Usually it is considered that such an optical scheme provides diffraction limited imaging if $\langle W \rangle \leq 0.07\lambda$ [9].

7.4 Experimental results

The equalizer optical scheme shown in Fig. 7.2b was experimentally realised and investigated. The grating used in this scheme was the same as described in Section 5.5.2. The array of attenuators was substituted by a plane gold-coated mirror. The transmission spectrum for non-polarized light at the output of equalizer (port 3 of circulator), measured with an optical spectrum analyser ANDO AQ-6315E, is shown as the solid line in Fig. 7.4.

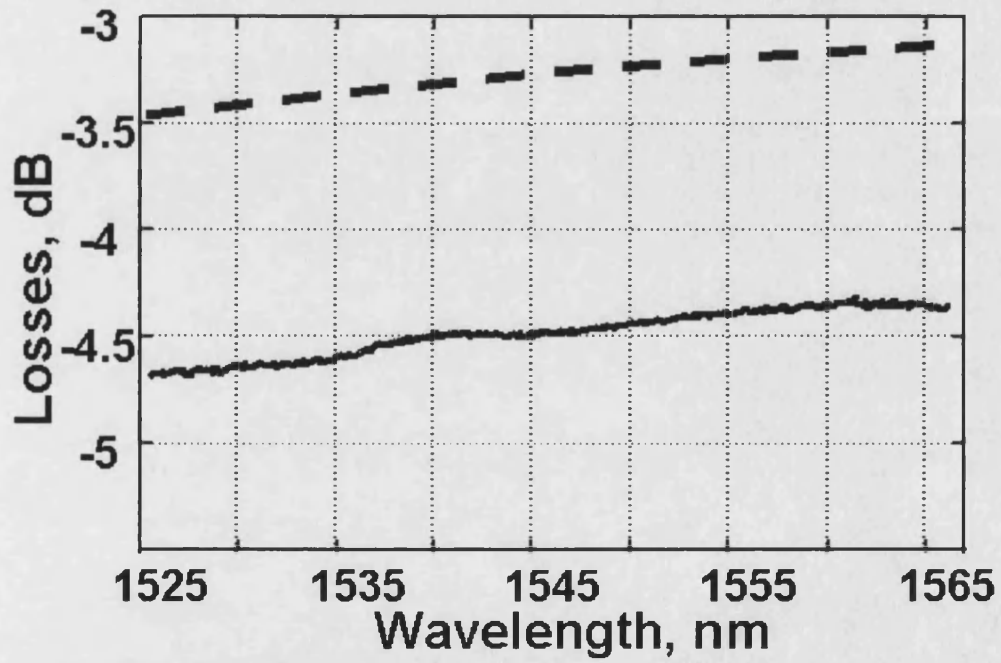

Fig.7.4. **Transmission spectrum of equalizer (solid curve), and grating diffraction efficiency loss (dashed curve).**

The main contributions to the measured transmission loss are due to non-ideal grating diffraction efficiency and the circulator insertion loss. Losses due to aberrations are negligible. The zero order $\lambda/4$ plate exchanges S- and P-polarizations, so that losses due to

diffraction after the double pass through the grating can be estimated as $L_G=\eta_S\eta_P$, where η_S and η_P are diffraction efficiencies for S- and P- polarizations, respectively. These diffraction losses, calculated from Fig. 5.1 are shown in Fig. 7.4 as the dotted line. Circulator losses for non-polarized light at λ=1545 nm were 0.9 dB (0.5 dB for the route 1→2, and 0.4 dB for the route 2→3). The circulator and grating together give 4.2 dB total loss at the central wavelength of 1545 nm. The additional 0.3 dB measured in the experiment can be accounted for by the fibre connectors.

It is very instructive to demonstrate the effect of using the λ/4 plate. Fig. 7.5 shows the experimentally measured PDL versus wavelength for the channel equalizer with and without λ/4 plate. It can be seen that the quarter-wave plate reduces the maximum PDL from 1.1 to 0.15 dB.

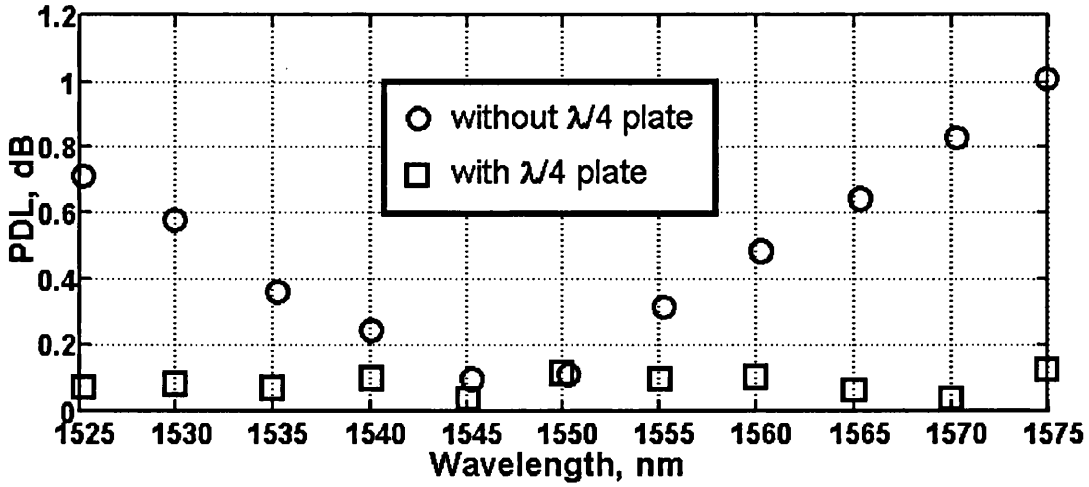

Fig.7.5. **Polarization depended losses with and without quarter-wave plate.**

The gold-coated mirror was tilted in the dispersion plane to estimate the achievable dynamic range of attenuation for the case when tilting micro-mirrors are used as attenuators. Fig. 7.6 shows the coupling efficiency for λ=1546 nm as a function of the plain

mirror tilt angle. A 25 dB dynamic range of attenuation corresponds to a 5° tilt, easily achieved with today's MEMS technology [6].

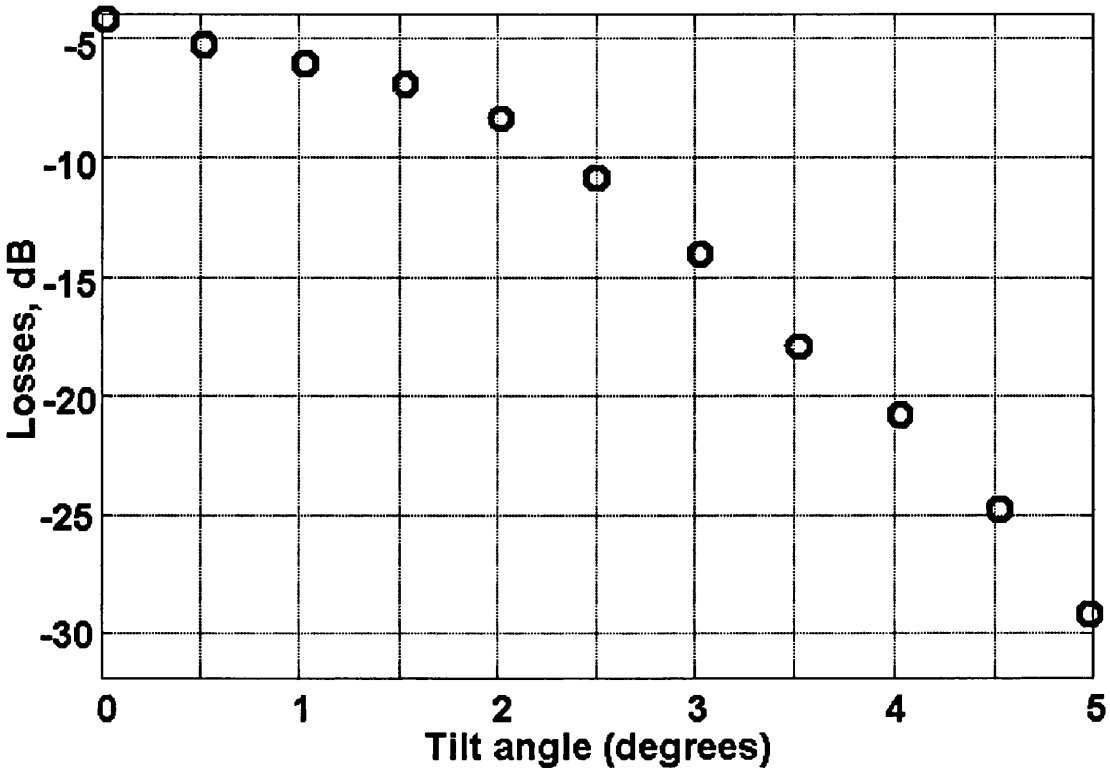

Fig.7.6. **Attenuation effect of the mirror tilt.**

7.5 Conclusions

The feasibility of a concave grating based channel equalizer with extremely low PDL, 25 dB dynamic range of attenuation, 4.5 dB losses and 40 nm operating spectral range is demonstrated experimentally and by ray-tracing analysis. In reality, this is a much easier design problem than realising the demultiplexer due to the following features:

1. No limitations on crosstalk;
2. Potential for PDL compensation by the λ/4 plate;
3. Much lower sensitivity to misalignments when using an optical circulator;
4. Lower aberrations due to the retro-reflective optical scheme.

References to Chapter 7

[1] J. E. Ford, J. A. Walker, "Dynamic Power Equalization Using Micro-Opto-Mechanics", *IEEE Photon. Technol. Lett.*, vol.10, 1998, pp.1440-1442.

[2] C. R. Doerr, C. H. Joyner, and L. W. Stulz, "Integrated WDM dynamic power equalizer with potentially low insertion loss", *IEEE Photon. Technol. Lett.*, vol.10, 1998, pp.1443-1445.

[3] H. S. Kim, S. H. Yun, H. K. Kim, N. Park, and B. Y. Kim, "Actively gain-flattened erbium-doped fibre amplifier over 35 nm by using all-fibre acoustooptic tunable filters", *IEEE Photon. Technol. Lett.*, vol.10, 1998, pp.790-792.

[4] W. Tomlinson, "Technologies for dynamic gain and channel power equalization", *Proc. OFC 2003*, paper TuM1.

[5] C. R. Doerr, L. W. Stulz, M. Cappuzzo, E. Laskowski, A. Paunescu, L. Gomez, J. V. Gates, S. Shunk, and A. E. White, "40-wavelength add-drop filter", *IEEE Photon. Technol. Lett.*, vol.11, 1999, pp.1437-1439.

[6] J. E. Ford, V. A. Aksyuk, D. J. Bishop, and J. A. Walker, "Wavelength add-drop switching using tilting micromirrors", *J. Lightwave Technol.*, vol.17, 1999, pp.904-911.

[7] J. E. Ford, J. A. Walker, and K. W. Goossen, "Fiber-coupled variable attenuator using MARS modulator", *Proc. SPIE*, vol.3226, 1997, pp.86-93.

[8] C. C. Bowley and G. P. Crawford, "Improved reflective displays based on polymer liquid crystals", *J. Opt. Technol.* vol.67, 2000, pp.717-722.

[9] M. Born, and E. Wolf, *Principles of Optics*. Pergamon Press, London, 1970.

Chapter 8

Passband flattening techniques for high spectral efficiency demultiplexers

8.1 Introduction

As discussed in Chapter 2, broadening and flattening of the passband in WDM demultiplexers is key to maximizing spectral efficiency and relaxing the tolerances on wavelength control in the network. In conventional demultiplexers there is a fundamental trade-off between the desirable passband and the achievable crosstalk levels. A lower crosstalk implies a wider separation between the output fibres/waveguides and, therefore, necessarily higher linear dispersion, resulting in proportional bandwidth narrowing. All methods, used currently for broadening and flattening the passband of multi/demultiplexers and wavelength routers, are based on the approach of widening the light spot at the facet of output fibre. This generally results in 2-3 dB of additional loss and a substantial increase in crosstalk between neighbouring channels.

Several techniques to broaden and flatten the demultiplexer passband have been considered, aimed at decreasing the sensitivity of the coupling efficiency to the wavelength variations. This can be realized by using wide multimode waveguides [1, 2], or by broadening and reshaping the output image [3, 4]. In this Chapter a completely different approach [5] based on the generation of inversely dispersed sources at the input of the demultiplexer is proposed and analyzed. In this way the positions of the output images

become independent of wavelength within the signal windows. A device based on a similar principle was implemented using a waveguide grating demultiplexer [6]. The proposed approach completely eliminates the conflicting requirements of bandwidth and crosstalk, so that an increase in dispersion leads simultaneously to a wider and a more rectangular passband and a lower crosstalk. A simple Fabry-Perot filter is proposed to provide further flattening of the transmission band. Improved spectral efficiencies of greater than 90% can be achieved with very low crosstalk.

8.2 Principal optical schemes

One possible scheme to achieve passband broadening consists of two identical demultiplexers arranged in cascade and separated by a micro-lens array is shown in Fig. 8.1. The demultiplexers are schematically shown as a combination of lenses and gratings to illustrate the imaging and dispersive functions. In practice, either concave gratings or plane gratings and lenses could be used. Each micro-lens transfers the inverted image of a single channel from the output plane of the first demultiplexer to the input plane of the second. At the output of the second demultiplexer the light from every channel is focused into its appropriate position, independent of wavelength shift $\delta\lambda$ within the signal window. The output fibre separation in this scheme is increased by a factor of 2 compared to single demultiplexer.

Instead of the first demultiplexer and micro-lens array, a more straightforward realization would use a multi-order diffractive element [7] operating in very high orders, so that the channel wavelengths are diffracted at the same angles into the different diffraction order. The channel wavelengths, and the corresponding diffraction orders M, should satisfy the relation $\lambda_n/\lambda_k=M_k/M_n$, where n and k are respective channel numbers. The dispersed multi-wavelength image is formed at the input of the demultiplexer as shown in Fig. 8.2,

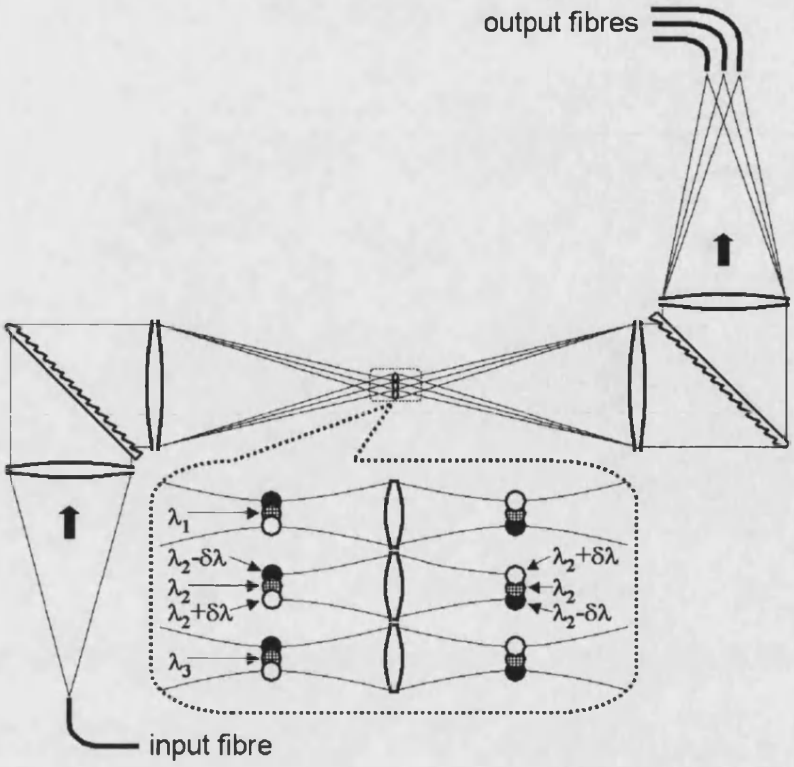

Fig.8.1. **Schematic diagram of a device with two identical demultiplexers and a micro-lens array**

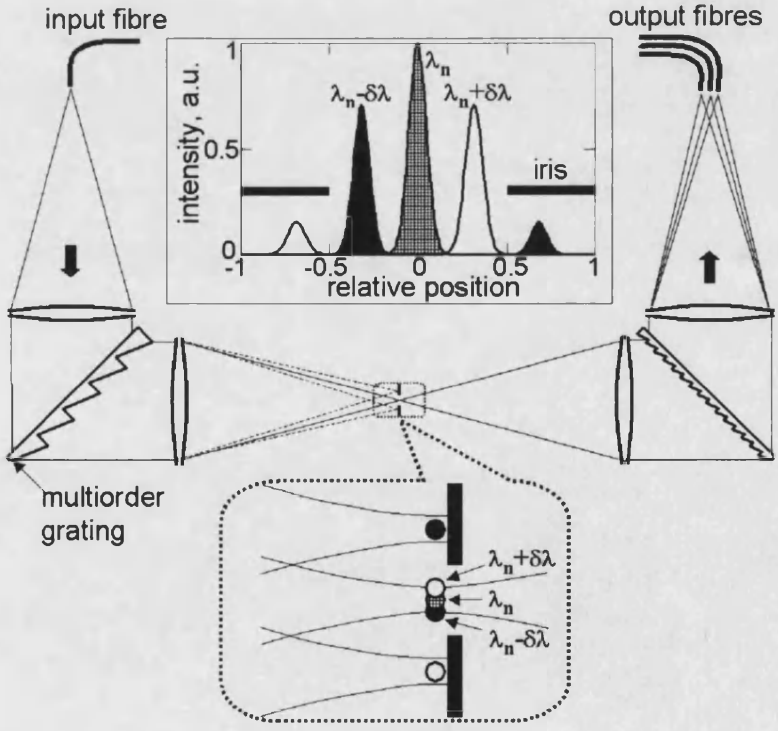

Fig.8.2. **Schematic diagram of the device with a multi-order diffractive element, demultiplexer, and iris**

and the parasitic orders are filtered by an iris. The dispersion values of the multi-order element and demultiplexer completely compensate for each other at the design wavelength. The intensity profiles at the wavelengths λ_n, λ_n-$\delta\lambda$, and λ_n+$\delta\lambda$ in the intermediate focal plane are shown in the inset of Fig. 8.2 for $\delta\lambda$=0.3(λ_n-λ_{n-1}).

8.3 Numerical results and discussion

All the calculations have been carried out for the device shown in Fig. 8.2 using Fourier analysis and the technique of overlap integrals, described in Chapter 3. However, here it is the Gaussian approximation for the modal field, which is used instead of the more accurate description of the fibre mode. This is because the use of the Gaussian approximation allows tractable calculations and is sufficient for the demonstration of the device operation principles.

The square apertures of the demultiplexer and multi-order device are truncated at the e^{-2} intensity level. For simplicity a demultiplexer operating with eleven 200 GHz spaced channels with wavelengths λ_1-λ_{11} (1542.04, 1543.63, 1545.22, 1546.81, 1548.4, 1550, 1541.6, 1553.21, 1554.81, 1556.42 1558.04 nm) was considered with the corresponding diffraction orders M_1=974, ..., M_{11}=964. The blazed gratings of the multi-order device and demultiplexer provide the maximum phase modulation of 969x2π and 10x2π, respectively, for the design wavelength λ_6=1550 nm. The key feature of this device is that in the absence of the fabrication errors and aberrations, the transmission spectrum is completely defined by the two following ratios. The first is the relative fibre spacing $\rho_1 = D_f/D_m$ and the second is ρ_2=D_i/D_f, where D_f is the output fibre separation, D_m is the fibre mode size at the e^{-2} intensity level, and D_i is the size of the iris. In all simulations, described below, ρ_2=0.95. The normalized transmission spectra of two adjacent channels for ρ_1=2.5 are shown in Fig.

8.3a to have a 3 dB bandwidth of $0.67\Delta\lambda$ and inter-channel crosstalk <-34 dB. The passbands for ρ_1=10 (corresponding to a factor of 4 higher dispersion) are shown in Fig. 8.3b with a 3 dB bandwidth of $0.85\Delta\lambda$ and inter-channel crosstalk <-51 dB. The passbands of conventional demultiplexers with the same aperture and ρ_1 values are also shown for comparison in Fig 8.3. In contrast to conventional demultiplexers, in this scheme a higher dispersion results in the wider and more rectangular passband. However, the curvature of the passband top remains approximately the same for any ρ_1. This is defined by the spectral dependence of the diffraction efficiency $\eta_M(\lambda)$ for the M-th diffraction order, which can be expressed [7] as $\eta_M(\lambda) = \mathrm{sinc}^2(969\lambda_6/\lambda - M)$.

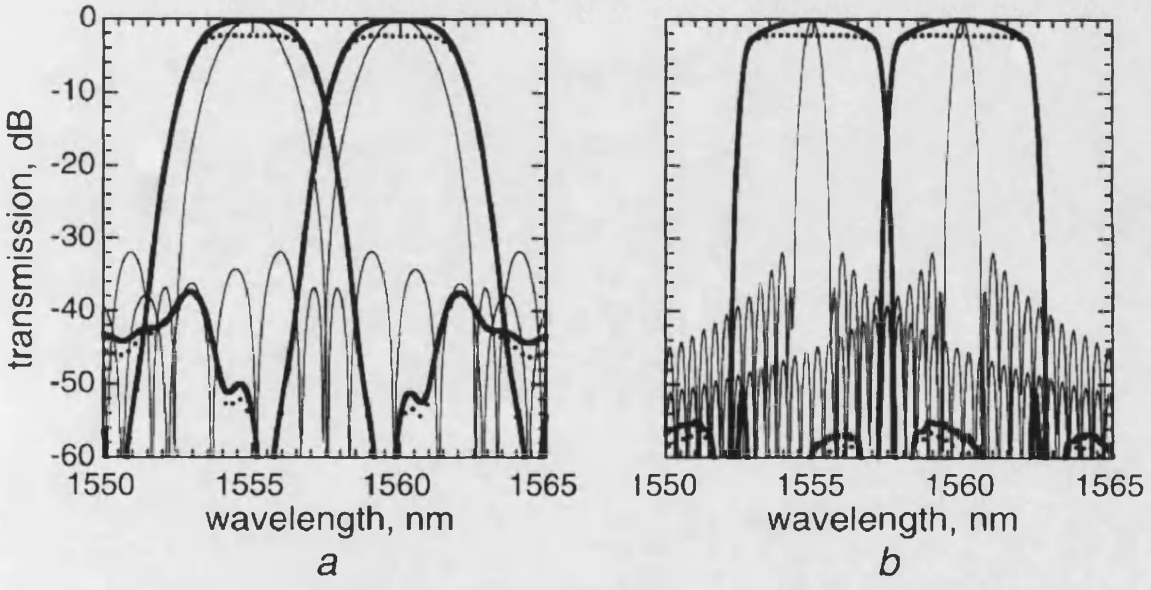

Fig.8.3. **Transmission spectra of two adjacent channels for relative fibre spacing ρ_1=2.5 (a) and ρ_1=10 (b). Fine, solid and dotted lines correspond to conventional demultiplexer, the device shown in Fig. 8.2, and the same device with Fabry-Perot filter, respectively.**

The remaining curvature of the passband top can be successfully compensated for in all the channels by a Fabry-Perot filter whose transmission minima coincide with the

channel wavelengths. The filter with a low reflectance (R=0.125) and an optical path length of $484.5\lambda'$, where λ'=1550.8 nm, is positioned at the device input. Its spectral transmission characteristic $T(\lambda) = 1/[1 + 0.653\sin^2(969\pi\lambda'/\lambda)]$ [8] allows flattening of the resultant passband substantially, as shown in Fig. 8.3 with only 2.2 dB additional losses. The 3 dB bandwidth becomes $0.78\Delta\lambda$ and $0.91\Delta\lambda$ for ρ_1=2.5 and 10, respectively, and the 1dB/20dB figure of merit [4] for the latter passband (ρ_1=10) can be estimated as 83%.

8.4. Conclusions

The principle of the cancellation of the wavelength-dependent image shifts in WDM demultiplexers was described. A device to achieve this using a multi-order diffractive element and conventional demultiplexer was proposed and analyzed numerically. Unlike in a conventional demultiplexer, the higher dispersion of the proposed scheme results in the improvement of all the performance characteristics. A Fabry-Perot filter at the input provides additional flattening and broadening of the transmission spectrum, to achieve a spectral efficiency as high as 91%. Such high efficiencies are particularly important for the spectrally demanding high bit-rate WDM RZ-based OTDM systems [9], which use much shorter pulses width than conventional NRZ (non-return-to-zero) intensity modulated transmission

References to Chapter 8

[1] M. R. Amersfoort, C. R. De Boer, F. P. G. M. Van Ham, M. K. Smit, P. Demeester, J. J. G. M. Van der Tol, and A. Kuntze, "Phased-array wavelength demultiplexer with a flattened wavelength response," *IEE Electronics Letters*, vol.30, 1994, pp. 300-301.

[2] M. R. Amersfoort, J. B. D. Soole, H. P. LeBlance, N. C. Andreadakis, A. Rajhel, and C. Caneau, "Passband broadening of integrated arrayed waveguide filters using multimode interference couplers," *IEE Electronics Letters*, vol.23, 1996, pp. 449-451.

[3] C. Dragone, T. Strasser, G. A. Bogert, L. W. Stulz, and P. Chou, "Waveguide grating router with maximally flat passband produced by spatial filtering," *IEE Electronics Letters*, vol.33, 1997, pp. 312-314.

[4] A. Rigny, A. Bruno, and H. Sik, "Multigrating method for flattened spectral response wavelength multi/demultiplexers," *IEE Electronics Letters*, vol.33, 1997, pp. 1701-1702.

[5] E. G. Churin, P. Bayvel, "Passband flattening and broadening techniques for high spectral efficiency wavelength demultiplexers", *IEE Electronics Letters*, vol.35, 1999, pp. 27-28.

[6] G. H. B. Thompson, R. Epworth, C. Rogers, S. Day, S. Ojha, "An original low-loss and pass-band flattened SiO_2 on Si planar wavelength demultiplexer," *Proc. OFC 1998*, p.77.

[7] D. Faklis, and G. M. Morris, "Spectral properties of multiorder diffractive lenses," *Applied Optics*, vol.34, 1995, pp.2462-2468.

[8] M. Born, and E. Wolf, *Principles of Optics*. Pergamon Press, London, 1970.

[9] Y. Miyamoto, *et al.* "1.04 Tbit/s DWDM transmission experiment based on alternate polarization 80 Gbit/s OTDM signals", *Proc. ECOC 1998*, vol. 3, pp55-57.

Chapter 9

Conclusions and future work

The feasibility of using a concave holographic grating in wavelength division multiplexed (WDM) optical network devices, such as multi/demultiplexers, routers and channel equalizers was studied in this work. The main advantage of this approach is that a single optical element in free space can perform the functions of both dispersion and imaging to realize the demultiplexing and routing functions. Free space optics demonstrates much lower temperature sensitivity and crosstalk level compared to integrated optics devices, which is especially important for wavelength routing applications. Modern WDM devices require diffraction-limited performance and extremely low polarization dependence for all wavelength channels, which is difficult to realize with a single optical surface because of the small number of free parameters used for optimization. However, as was shown in Chapters 4 and 5, four free parameters defining the concave grating mount are enough to meet all requirements.

Accurate aberration analysis allowed derivation of the novel analytic formulae that define the parameters of the grating mounts minimizing astigmatism (the largest chromatic aberration for a concave grating) in the vicinity of the designed wavelength. These mounts give diffraction limited imaging of a fibre mode within the operating spectral range of WDM optical networks. This analysis and developed techniques for the optimization of the holographic recording scheme were used to design and produce a 49-channel demultiplexer, a 91x91 wavelength router and a channel equalizer. The experimental measurements and the characterization of the demultiplexer and channel equalizer showed

very good performance characteristics consistent with simulation results and confirmed the validity of the developed design concept.

In addition, the proposed stationary anastigmatic concave grating spectrograph has been modified into a novel retro-reflective scheme by introducing a convex mirror, providing a factor of two higher dispersion, and much larger image field without an increase of aberrations. The design of a wavelength router revealed additional difficulties compared to the demultiplexer, such as the necessity to minimize astigmatism in both the forward and the reverse directions and more complex realization of the fibres-in-V-grooves arrays.

Special attention was devoted to the analysis of crosstalk in WDM devices arising from the combined effect of aberrations, diffraction at the aperture and diffuse scattering. A background crosstalk level of –60 dB was demonstrated experimentally for a holographic concave grating with diamond aperture. It was also shown analytically that holographic grating-based routers with circular and diamond aperture are absolutely scalable from the coherent crosstalk point of view.

And finally, a novel technique for the realization of a flat top passband in WDM demultiplexers allowing more than 90% spectral efficiency with a very low crosstalk was proposed.

It is very important to understand the ways and possibilities for further development and improvements of the concave grating based devices to meet the growing telecommunications demands. The constantly increasing information flow will require more and more bandwidth from the WDM optical networks. There are two approaches to increase the obtainable capacity:

1) Increase in the density of the wavelength channels. This allows more effective filling of the fibre bandwidth, but is, of course, limited. 50 GHz spaced channels are already quite effective and match the currently achievable, state-of-the art bit rate of modulators and receivers, so that further decrease in the channel spacing may not provide any gain in the data flow. Nevertheless, some network operators and manufacturers prefer to deal with the higher number of wavelength channels (≤25 GHz separation) allowing more flexibility and larger number of direct interconnections.
2) Extensive development results in increase of the available low-loss fibre bandwidth from C-band (1525-1565 nm) to adjacent S- (1480-1525 nm) and L- (1565-1610 nm) bands, and the elimination of the water peak in the fibre fabrication so that total bandwidth will increase to over 300 nm or 40 THz.

First, consider how many channels a concave holographic grating can successfully demultiplex within the C-band? The simplest way to increase the channel count in the same optical scheme is to use more output fibres with proportionally decreased fibre separation. However, this method is not constructive, because it results in a much higher adjacent channels crosstalk. A more sensible solution is to keep the same fibre spacing, but to increase proportionally the demultiplexer dimensions, which results in a larger linear dispersion. However, in this case, all the aberrations also increase by the same factor. To estimate a theoretical limit for the concave grating demultiplexer dimensions consider the RMS wave aberration $<W>$ shown in Fig. 5.3 as a function of wavelength. For the "ideal" grating (dashed line) $<W>$ does not exceed 0.007λ within the C-band, so that all the dimensions of optical scheme can be increased by the factor of 10 whilst remaining within the Marechal criterion ($<W>\leq 0.07\lambda$) for diffraction-limited imaging. This results in 490, 10 GHz spaced, channels. However, a real, holographically recorded grating gives $<W>=0.055\lambda$ for the central wavelength (solid line in Fig. 5.3) and does not leave any

room for the further enlargement of the optical scheme. This implies that for any further increases in the channel density, the realisation of the holographic grating should approach much closer to that of the "ideal" one.

Currently the residual aberrations of real gratings can be explained by the lack of free parameters for further optimisation of the holographic recording scheme. There are only four recording parameters defining the positions of two stigmatic point sources in the dispersion plane of the grating. A possible way to increase the optimization freedom is to use aberrated sources instead of stigmatic. This will allow four additional parameters to be obtained by introducing spherical aberration and astigmatism into recording sources, although in this case the derivation of the analytical expression for the wave aberration function is not a trivial exercise. In addition, the holographic recording scheme becomes more complicated. However, this problem must be solved in the near future to allow the demultiplexing of a much larger number of channels using a single optical element.

The main obstacle in the extensive development of concave grating demultiplexer is polarization dependent loss (PDL), which increases proportionally with the operating spectral range. To double the spectral range of a demultiplexer, the concave grating and convex mirror spectrograph, proposed in section 4.8 and shown in Fig. 4.19, can be used. In this case a zero- order $\lambda/4$ plate should be inserted between the concave grating and the convex mirror to compensate for the PDL in the same way as in for channel equalizer described in Chapter 7. The concave grating presented in Chapter 5 together with a convex mirror with a radius of curvature of 44 mm can successfully demultiplex 200, 50 GHz separated channels within the spectral range 1507-1585 nm. The doubling of the channel density is due to the doubling of the linear dispersion compared to the initial demultiplexer.

Encouraging results described in chapters 6 and 7 indicate the potential of the concave grating based wavelength router and channel equalizer to be implemented in

practical devices. In addition, there is still a wide research field on the application of concave gratings in such active WDM devices as gain flattening filters and add/drop multiplexers, and future research work is likely to focus in these areas.

List of abbreviations

AWG: arrayed waveguide grating

BER: bit error rate

BT: British Telecom

CTE: coefficient of thermal expansion

ECOC: European Conference on Optical Communications

EDFA: erbium-doped fibre amplifier

FD: Fraunhofer diffraction

FPR: free propagation region

FSDG: free-space diffraction grating

ITU: International Telecommunications Union

MEMS: micro-electro-mechanical systems

MMI: multi-mode interference

NA: numerical aperture

NRZ: non-return to zero

OFC: Optical Fibre Communications Conference

OTDM: optical time division multiplexing

PDL: polarization-dependent loss

RMS: root-mean-square

RS: Royal Society

RZ: return to zero

SA: stationary anastigmatic

SMF: single-mode fibre

TDM: time division multiplexing

TEC: thermo-electric cooler

ULE: ultra low expansion

WDM: wavelength division multiplexing

Isotopic labeling

From Wikipedia, the free encyclopedia
(Redirected from Isotopic tracer)

Isotopic labeling is a technique for tracking the passage of a sample of substance through a system. The substance is 'labeled' by including unusual isotopes in its chemical composition. If these unusual isotopes are later detected in a certain part of the system, they must have come from the labeled substance.

In ordinary isotopic labeling, there are two ways to detect the presence of labeling isotopes. Since isotopes have different masses, they can be separated using mass spectrometry. Another consequence of the difference in mass is that molecules containing isotopes have different vibrational modes; these can be detected by infrared spectroscopy.

Isotopic labeling can also be used to study chemical reactions. In this method specific atoms are replaced by an isotope in a reactant molecule which then participates in a chemical reaction. With spectroscopy, nuclear magnetic resonance spectroscopy for example, it is now possible to identify where a particular molecular fragment in the reactant ends up as a particular fragment in one of the reaction products.

An example of the use of isotopic labeling is the study of phenol (C_6H_5OH) in water by replacing common hydrogen (protium) with deuterium (**deuterium labeling**). Upon adding phenol to deuterated water (water containing D_2O in addition to the usual H_2O), the substitution of deuterium for the hydrogen is observed in phenol's hydroxyl group (resulting in C_6H_5OD), indicating that phenol readily undergoes hydrogen-exchange reactions with water. Only the hydroxyl group was affected, indicating that the other 5 hydrogen atoms did not participate in these exchange reactions.

Contents

Radioisotopic labelling

Radioisotopic labelling is a technique for tracking the passage of a sample of substance through a system. The substance is "labelled" by including radionuclides in its chemical composition. When these decay, their presence can be determined by detecting the radiation they emit. Radioisotopic labelling is a special case of **isotopic labeling**.

For these purposes, a particularly useful type of radioactive decay is positron emission. When a positron collides with an electron, it releases two high-energy photons traveling in diametrically opposite directions. If the positron is produced within a solid object, it is likely to do this before travelling more than a millimetre. If both of these photons can be detected, the location of the decay event can be determined very precisely.